

Development of Metal-Assisted Chemical Etching (MACE) Based Silicon (Si) Nano/microstructures and Their Applications in Surface Enhanced Raman Spectroscopy (SERS) for Chemical Sensing

Submitted by

Debabrot Borgohain

Reg. No.11ENPT08

A thesis submitted to the University of Hyderabad in partial fulfilment of the requirements
for the award of degree

Doctor of Philosophy
in
Nanoscience and Technology

Under the supervision of

Dr. Raj Kishora Dash



School of Engineering Sciences & Technology

University of Hyderabad

Prof. C. R. Rao Road, Hyderabad-500046

India, 2018



CERTIFICATE

This is to certify that the thesis entitled "**Development of Metal-assisted chemical etching (MACE) based Silicon (Si) Nano/microstructures and their Applications in Surface Enhanced Raman Spectroscopy (SERS) for Chemical Sensing**" submitted by **Debabrot Borgohain** bearing registration number **11ENPT08** in partial fulfilment of the requirements for award of **Doctor of Philosophy** in the **School of Engineering Sciences and Technology** is a bonafide work carried out by his under my supervision and guidance.

This thesis is free from plagiarism and has not been submitted previously in part or in full to this or any other University or Institution for the award of any degree or diploma.

Parts of this thesis have been:

- A. Published in the following publications:
 - i. Debabrot Borgohain and Raj Kishora Dash, Journal of Material Science: Materials in Electronics, 29 (5), 4211-4216 (2018).
- B. Presented in the following conferences:
 - i. D. Borgohain and R. K. Dash, "Comparative study of thermal annealing effect of Gold (Au) and Silver (Ag) metal catalysts on metal-assisted chemical etching of Silicon (Si)", *International Conference on Nanotechnology: Idea, Innovations & Initiatives (ICN:3I -2017)*, IIT Roorkee, Uttarakhand, 6-8 December, 2017.
 - ii. D. Borgohain and R. K. Dash, "Development of a Novel Mask-Less Microfabrication Process for Nanostructure formation by using Metal-Assisted Chemical Etching", *4th Int. Conference Advanced Nanomaterials and Nanotechnology(ICANN-2015)*, IIT Guwahati, Guwahati, Assam, 8-11 December 2015.

Further, the student has passed the following courses towards fulfilment of the coursework requirement for PhD.

Course Code	Name	Credits	Pass/Fail
NT601	Research Methodology	4	Pass

and was exempted from doing coursework (recommended by Doctoral Committee) on the basis of the following course passed during his M. Tech. program (in Int. M.tech./Ph.D. program) and the M.Tech. was awarded:

Course Code	Name	Credits	Pass/Fail
NT401	Thermodynamics and Phase Equilibria	4	Pass
NT402	Concepts of Material Science	4	Pass
NT403	Characterization of Materials	4	Pass
NT404	Seminar	2	Pass
NT405	Advanced Engineering Mathematics	2	Pass
NT406	Materials Processing and Characterization Laboratory	4	Pass
NT407	Concepts of Nanoscience and Technology	4	Pass
NT408	Synthesis and Applications of Nanomaterials	4	Pass
NT451	NanoBiotechnology	4	Pass
NT452	Mechanical Behaviour of Nanomaterials	4	Pass
NT453	Modelling and Simulation	4	Pass
NT454	MEMS and NEMS Nanofabrication Technologies	4	Pass
NT455	Surface Engineering	4	Pass
NT456	Polymer Science and Technology	2	Pass
NT457	Laboratory	4	Pass
NT458	Seminar	2	Pass
NT550	Dissertation	18	Pass

Dr. Raj Kishora Dash
Supervisor

Prof. M. Ghanashyam Krishna
Dean, SEST, UoH



DECLARATION

I hereby declare that the work reported in the Ph.D. thesis entitled, "**Development of Metal-assisted chemical etching (MACE) based Silicon (Si) Nano/microstructures and their Applications in Surface Enhanced Raman Spectroscopy (SERS) for Chemical Sensing**" submitted to University of Hyderabad for the award of Doctor of Philosophy in Nanoscience and Technology in original and was carried out by me during my tenure as a Ph.D. scholar under the supervision of Dr. Raj Kishora Dash, Assistant Professor at the **University of Hyderabad, India**. This thesis has not formed the basis for the award of any degree, diploma, associateship, membership or similar title of any university or institutions. Finally, plagiarism of this thesis is checked and satisfied the requirements.

Debabrot Borgohain

School of Engineering Sciences & Technology

University of Hyderabad

Hyderabad-500046

India

Place: Hyderabad

Date:



CERTIFICATE

This is to certify that the thesis work entitled, "**Development of Metal-assisted chemical etching (MACE) based Silicon (Si) Nano/microstructures and their Applications in Surface Enhanced Raman Spectroscopy (SERS) for Chemical Sensing**", submitted by Debabrot Borgohain bearing Reg. No. **11ENPT08** in partial fulfilment of the requirements for the **Doctor of Philosophy** in **Nanoscience & Technology** is a bonafide record of the work that has been carried out by him under my supervision. This thesis has not formed the basis for the award of any degree, diploma, associateship, membership or similar title of any university or institutions. Finally, plagiarism of this thesis is checked and satisfied the requirements.

Dr. Raj Kishora Dash (Supervisor)

Assistant Professor

SEST

University of Hyderabad

Prof. M. Ghanashyam Krishna

Dean

SEST

University of Hyderabad

ACKNOWLEDGEMENT

I feel privileged to place before you my research work entitled "**Development of Metal-assisted chemical etching (MACE) based Silicon (Si) Nano/microstructures and their Applications in Surface Enhanced Raman Spectroscopy (SERS) for Chemical Sensing**".

For the overall completion of this research work, I owe its success to numerous diligent personalities.

First and foremost, I wish to place my sincere gratitude to my young, dynamic and inspiring supervisor Dr. Raj Kishora Dash, Assistant Professor, School of Engineering Sciences & Technology, who has provided a considerable wealth of resources, opportunities and guidance during my whole research work. His support has been an essential factor towards the completion of this thesis.

My sincere thanks to my doctoral committee members Dr. R. Vijay, Scientist F and team leader, International Advanced Research Centre for Powder Metallurgy and New Materials (ARCI) and Dr. Swati Ghosh Acharyya, Assistant Professor, School of Engineering Sciences & Technology, UoH, for their kind guidance and support throughout my research work.

I also would like to thank Prof. M. Ghanashyam Krishna, Dean, School of Engineering Sciences and Technology, for his constant suggestions and supports towards the completion of my research work in the stipulated time.

I also want to express my sincere thanks to the University Grants Commission, New Delhi, India for the financial support received through the National Fellowship for OBC candidate.

I also thank all the laboratory technicians for XRD, TEM, FESEM, Raman spectroscopy, AFM for their friendship and technical support.

I also would like to express my sincere thanks to the Centre for Nanotechnology, University of Hyderabad for helping me to carry out my research work.

I also use this opportunity to convey my thanks to all my group members and fellow students for their co-operation and help.

I would like to take this opportunity to express my thanks to my friends Ayangleima, Abhishek, Vipul, Chandu, Naveen, Bikash who helped me in many ways to complete my research work.

Finally, I extend my deep sense of gratitude and thanks to all the teaching and non-teaching staff for their guidance and king co-operation in the completion of this research work. My stay at the University of Hyderabad has been made so unforgettable and enjoyable either

directly or indirectly by many other friends like Naren, Sandeep, Yugantak, Sikha, Pooja, Himadri, Heerock, Hemanta, Kaushik when I spent the time with them.

Last, but not the least, I would like to thank my parents and sister for providing an abundance of love, encouragement and support towards the completion of my PhD journey.

Papers published/communicated/conference attended

A. Communicated/published in the following publications

1. Enhancement in the detection limit and enhancement factor to detect molecular level methylene blue (MB) by depositing discontinuous Au thin film on nanoporous Si fabricated by metal-assisted chemical etching process. (to be submitted)
2. Investigation on the formation of nanopores in silicon by directly using the silver nanoparticles as metal catalyst for surface-enhanced Raman scattering (SERS) active substrate preparation. (submitted)
3. Understanding the influence of thermal annealing of the metal catalyst on the metal-assisted chemical etching. (Journal of Material Science: Materials in Electronics, 29 (5), 4211-4216, 2018).
4. Effect of conductive and non-conductive substrates on the formation of anodic aluminium oxide (AAO) template for mask-less nanofabrication. (Microelectronic Engineering, 157, 1-6, 2016)

B. Poster/paper presented in the following conferences

1. Poster presented: “Comparative study of thermal annealing effect of gold and silver metal catalysts on metal-assisted chemical etching of silicon”, ICN:3I-2017, IIT Roorkee, India.
2. Poster presented: “Development of a novel mask-less nanofabrication process for nanostructure formation by using metal-assisted chemical etching”, ICANN-2015, IIT Guwahati, India.
3. Paper presented: “Effect of different process parameters on formation of nanotemplates based mask-less lithography on different substrates for nanosensor applications”, ICNT-2013, Institute of fire and safety engineering, Haldia, India.
4. Poster presented: “Development of mask-less nanofabrication process for tin oxide periodic nanostructure”, EIPBN-2013, Nashville, USA.

LIST OF TABLES

Table no.	Description	Page No.
2.1	Deposition parameters for Au thin film deposition by RF sputtering.	34
2.2	Deposition parameters for Au and Ag thin films deposition by RF sputtering.	38
2.3	Deposition parameters for Au thin film deposition by thermal evaporation.	41
3.1	Roughness values for the thin films deposited with different source to substrate distance.	63
4.1	Deposition parameters for the discontinuous thin film deposited by thermal evaporation.	75
4.2	Different Si micro/nanostructured substrates used for SERS measurements	83
5.1	Details about the coating parameters of dip and spin coating.	88

LIST OF FIGURES

Figure no.	Description	Page no.
1.1	Various applications of MACE technique in nano/microstructures fabrication on Si substrates.	3
1.2	SEM images of post-etching Pt-coated Si (100) substrate etched in HF/H ₂ O ₂ solution for 30 s.	3
1.3	Scheme of the H ₂ O ₂ reduction at Pt nanoelectrodes and injecting holes into the Si substrate for the initiation of etching.	4
1.4	SEM images (at 45°) of post etched p-Si (100) samples etched with HF-H ₂ O ₂ of different values.	5
1.5	Graphical representation of the proposed mechanism of cone-shaped pore formation in HF-H ₂ O ₂ solutions with ρ between 20% and 70%	5
1.6	Raman spectra of liquid pyridine and at the Ag electrode.	6
1.7	Schematic representation of the reason for the polarization of light with E vector along the inter-particle axis which can result in huge enhancements in the gap between the two NPs while the orthogonal polarization cannot.	7
1.8	Cross-sectional SEM images of the sample where etching was done in a mixed solution of 50% HF, 30% H ₂ O ₂ , and H ₂ O at a volume ratio of 2:1:8 for 5 min.	8
1.9	Cross-sectional SEM images of the generated holes in Si when etching was carried out in a mixed solution of 50% HF and 30% H ₂ O ₂ at a volume ratio of 10:1 for 5 min.	8
1.10	Schematic of the deposition of Ag by an electroless process on Si in HF/AgNO ₃ solution and the Ag NP-catalyzed chemical etching of Si in HF/Fe(NO ₃) ₃ solution.	9
1.11	TEM images of Si nanowires.	10
1.12	Scheme of the electrokinetics for autonomous movement of Ag particles in bulk Si	10

	induced by catalytic reactions	
1.13	Post UV ozone PVP removal by etching with Ag nanorods and nanodonuts where $\rho=90$ etchant for 10 min.	12
1.14	SEM images of etched Si with EBL-patterned Au catalysts for 40 min.	12
1.15	Scheme of the etching mechanism. (A) the one-step process and (B) the two-step process	14
1.16	Post etching AFM height images of an Au nanocube and an Au nanoprism on a substrate of Si after etching for 20 min.	15
1.17	The mechanism associated with metal-assisted etching. Accumulation of charge on the metal nanoparticle generates an electric field.	16
1.18	Scheme of the reduction potentials of the two half reactions of MACE which is relative to the standard hydrogen electrode, VSHE.	17
1.19	Schematic representation of possible diffusion processes of the reactants and reaction products during MACE.	18
1.20	Schematic illustration of the Ag particles' rotational direction and probable paths of moving during the forming process of helical pores with various pitches and widths.	20
1.21	Cross-sectional SEM images of the arrays of aligned Si nanowire obtained from the catalytic etching of n-type Si.	21
1.22	Scheme of the whole MACE process by using (a) silver and (b) gold metal catalysts.	21
1.23	Illustration of the formation of the chain-like array of Ag NPs aggregates within PVA nanofibers.	22
1.24	SEM images of the SERS-active substrates: an array of gold nanowires with variable lengths.	23
1.25	Graphical illustration of the fabrication of NPs on Si (flat, thermally conducting), glass (flat, thermally insulating), and paper (fibrils, thermally insulating) by taking advantage of the laser-induced photothermal effect.	24
1.26	Illustration of the whole fabrication process of the silver-coated silicon nanowire arrays.	24
1.27	The scheme of the experiments.	25
1.28	Details about the fabrication process of the silicon nanowire arrays coated with silver.	25
1.29	Schematic diagram of the experimental process flow.	26
1.30	Schematic representation of the production of the superhydrophobic SERS substrate created with the hierarchical silicon nanostructures.	26
1.31	Collected Raman spectra of the real blood sample with and without the NPs. Correspondingly in the plot, Glucose peak and other blood peaks are shown	27
1.32	SERS spectra acquired by AuNPs/Psi SERS active substrate for the Penicillin G antibiotic at different concentrations	28
2.1	XRD pattern of Au thin film deposited on Si substrate for 4 minutes.	35
2.2	XRD pattern of Au thin film deposited on Si substrate for 8 minutes.	36
2.3	XRD pattern of Au thin film deposited on Si substrate for 23 minutes.	36
2.4	EDX spectra of the first deposited Au thin film on Si substrate.	37

2.5	EDX spectra of the second deposited Au thin film on Si substrate.	37
2.6	EDX spectra of the third deposited Au thin film on Si substrate	38
2.7	XRD pattern of Au thin film deposited on Si substrate by thermal evaporation.	39
2.8	XRD pattern of Ag thin film deposited on Si substrate by thermal evaporation.	40
2.9	EDX spectra of the thermally evaporated Au thin film on Si substrate.	40
2.10	EDX spectra of the thermally evaporated Ag thin film on Si substrate.	40
2.11	XRD pattern of Au thin film deposited on Si substrate by maintaining 10 cm gap between source and substrate.	42
2.12	XRD pattern of Au thin film deposited on Si substrate by maintaining 12 cm gap between source and substrate.	42
2.13	XRD pattern of Au thin film deposited on Si substrate by maintaining 15 cm gap between source and substrate.	43
2.14	EDX spectra of the thermally evaporated Au thin film on Si substrate by maintaining 10 cm gap between source and substrate.	44
2.15	EDX spectra of the thermally evaporated Au thin film on Si substrate by maintaining 12 cm gap between source and substrate.	44
2.16	FESEM image of the Micro-stripes fabricated on Si substrate.	45
2.17	The width of the Au catalyst (a) optical microscope image, (b) FESEM image.	45
2.18	Surface profilometer plots of (a) 20 nm (b) 50 nm and (c) 140 nm thin patterned Au micro-stripes on Si substrate.	46
2.19	Surface profilometer plots of (a) Au (b) Ag micro stripes on the Si substrate.	47
2.20	Surface profilometer plots of micro-stripes fabricated on Si substrate from Au thin film.	47
3.1	Schematic representation of the MACE process on Si substrate by using Au micro-stripes as a catalyst.	50
3.2	Si substrate after MACE by 20nm thick Au micro-stripes (a) top view and (b) cross-section view.	52
3.3	Si substrate after MACE by 20nm thick Ag micro-stripes (a) top view and (b) cross-section view.	52
3.4	3D AFM image of post-MACE Si substrate fabricated by Ag micro-stripes.	53
3.5	Si substrate after MACE by annealed Au micro-stripes (a) top view and (b) cross-section view.	53
3.6	: FESEM images of the patterned Au micro-stripes (TMS20Au) on Si substrate (a) As-deposited (b) after annealing at 200°C.	54
3.7	FESEM images of the patterned Au micro-stripes (TMS20Ag) on Si substrate (a) As-deposited (b) after annealing at 200°C.	54
3.8	Si substrate after MACE by annealed Ag micro-stripes (a) top view and (b) cross-section view.	55
3.9	FESEM images of the patterned Au micro-stripes on Si substrate (SMS20Au) (a) As-deposited (b) after annealing at 200°C.	56

3.10	Top view of Si substrate after MACE by un-annealed SMS20Au micro-stripes.	57
3.11	Cross-section view of Si substrate after MACE by un-annealed SMS20Au micro-stripes.	57
3.12	Top view of Si substrate after MACE by annealed SMS20Au micro-stripes.	58
3.13	Cross-section view of Si substrate after MACE by annealed SMS20Au micro-stripes.	58
3.14	FESEM images of chemically etched p-Si (100) substrates where etching was done by using annealed (a,b) SMS50Au and (b,d) SMS140Au micro stripes	59
3.15	: FESEM cross-section images of MACE chemically etched p-Si (100) substrates by using (a) SMS50Au thin and (b) SMS140Au thick annealed Au micro stripes.	60
3.16	Schematic representation of the proposed mechanism of the MACE process by using an annealed Au micro stripe of (a) 50 nm and (b) 140 nm thicknesses and width more than 3 μ m.	60
3.17	Optical surface profilometer images (a) 2-D and (b) 3-D of etched p-Si (100) substrate after MACE by Au strip of 50 nm.	60
3.18	: Optical surface profilometer images (a) 2-D and (b) 3-D of etched p-Si (100) substrate after MACE by Au strip of 140 nm.	61
3.19	Typical FESEM images of (a) p-Si (100) substrate after MACE and followed by removal of Au micro stripes (140 nm) with a higher concentration of H_2O_2 and (b) enlarged view of the polished region formed after the MACE process.	62
3.20	FESEM images of MS₁ (a) Low and (b) High magnification.	63
3.21	FESEM images of MS₂ (a) Low and (b) High magnification.	64
3.22	AFM images of Au thin film deposited by fixing source to substrate distance at 10 cm.	65
3.23	AFM images of Au thin film deposited by fixing source to substrate distance at 12 cm.	65
3.24	FESEM images of Si substrate after MACE by MS₁ micro-stripes (a) as a catalyst and (b) its magnified image of the area shown in Fig. 3.24 (a).	66
3.25	FESEM images of Si substrate after MACE by MS₂ micro-stripes (a) as a catalyst and (b) zoomed area of the related region in Fig. 3.25 (a).	66
3.26	3D AFM images of Si substrate after MACE by (a) MS₁ and (b) MS₂ micro-stripes.	67
3.27	AFM depth profile analysis of Si substrate after MACE by MS₁ micro-stripes.	67
3.28	AFM depth profile analysis of Si substrate after MACE by MS₂ micro-stripes.	67
4.1	Illustration of SERS mechanism.	71
4.2	Portable Raman spectrometer used for SERS detection.	72
4.3	FESEM images of p-Si (100) substrate after MACE process (a, b) by using Ag micro-stripes, (c, d) Au micro-stripes as a catalyst.	73
4.4	FESEM images of (a,b) AgSiM and (c,d) AuSiM substrates deposited with Ag NPs.	73
4.5	SERS spectra of MB of 50 nM detected by micro/nanostructured Si substrate prepared by (a) Ag assisted MACE process, (b) Au assisted MACE process.	74
4.6	SERS spectra of MB of 0.1 M detected by bare Si substrate.	75
4.7	SERS spectra of 50 nM MB detected by a Si substrate (without any micro/nanostructures on the surface) coated with Ag NPs.	76
4.8	SERS spectra of MB of 50 nM tested with a MACE modified Si substrate without coating any noble metal on the surface of the substrate.	76
4.9	Au deposited on the MACE Si substrate (using 20 nm Ag micro-stripes) by thermal	77

	evaporation for SERS measurement.	
4.10	EDX analysis of the evaporated thin film on (Ag micro-stripes assisted) MACE modified Si substrate.	78
4.11	: Surface profilometer plot of the deposited 10 nm Au thin film on nanostructured AgSiM substrate.	78
4.12	: SERS spectra of MB of 5 nM detected by 10 nm Au thin film and Ag NPs coated nanostructured Si substrate produced by Ag assisted MACE process.	79
4.13	: FESEM image of 10 nm Au discontinuous thin film coated nanoporous Si substrate fabricated by Ag assisted MACE process.	79
4.14	SERS spectra of MB of 5 nM by Au thin film coated on bare Si substrate.	80
4.15	Surface profilometer reading of the deposited (a) 20 nm, (b) 30 nm, (c) 40 nm and (d) 50 nm Au thin film on nanostructured Si substrate	81
4.16	SERS spectra of MB of 100 pM by the 20AuSi substrate.	81
4.17	FESEM image of 20 nm Au discontinuous thin film coated on nanoporous Si substrate fabricated by Ag assisted MACE process.	82
4.18	FESEM image of 30 nm Au discontinuous thin film coated on nanoporous Si substrate fabricated by Ag assisted MACE process.	82
4.19	SERS spectra of MB of 10 pM by the 30AuSi substrate.	83
4.20	FESEM image of (a) 40 nm Au discontinuous thin film and (b) 50 nm coated on nanoporous Si substrate fabricated by Ag assisted MACE process.	84
4.21	A comparative plot of SERS spectra of MB detected by different SERS substrates mentioned in Table 4.2	86
5.1	XRD pattern of Ag NPs.	90
5.2	(a) TEM and (b) EDX of Ag NPs.	90
5.3	Size distribution analysis of Ag NPs.	91
5.4	FESEM images of Ag nanoparticles coated on p-Si (100) substrate by (a,c) dip coating and (b,d) spin coating method.	91
5.5	FESEM image of p-Si (100) substrate after MACE by (a,c) dip coated and (b,d) spin coated Ag nanoparticles	92
5.6	Size distribution of nanopores formed on p-Si (100) substrate after MACE by (a) dip coated Ag NPs (b) Spin coated Ag NPs.	93
5.7	SERS spectra of MB of 50 nM detected by Ag NPs coated nanostructured Si substrate produced by Ag NPs assisted MACE process.	94

ABSTRACT

Surface-enhanced Raman Scattering (SERS) has emerged as a key research area for its excellent detection capability and fingerprint identification of the various chemicals such as methylene blue (MB), malachite green (MG), melamine etc. Recently, it has drawn tremendous attention for potential application in the food sector, medical sector, security sector etc. Though some progresses have already been achieved in the molecular level detection of chemical species with SERS technique, still more challenges are there such as repeatability, scalability, reproducibility, shelf life. One of the key factors is the development of the SERS substrates for improvements in the SERS signal and detection limit as well.

In this regard, significant progress has already been achieved in the fabrication of the SERS-active substrates by using both the top-down and bottom-up approaches. Bottom-up approaches, such chemical synthesis, self-assembly, electrodeposition, dip-coating processes are successfully employed to fabricate SERS-active substrates. On the other hand, the top-down approaches, such as lithography, oblique angle metal film deposition and metal-assisted chemical etching (MACE) and which are mainly used to fabricate various nanostructures, has shown very effective and reproducible SERS-active substrates preparation. However, still preparation of the SERS substrates with enhanced Raman signal and also with higher detection limit have been considered as the main challenges and need to be addressed.

Though, several existing approaches such as conventional or unconventional nanofabrication methods are used for the preparation of Si-based SERS substrates by top-down approach, MACE process is emerging as a very simple and cost-effective process for fabrication of the nanostructures and hence, it has gained sufficient attention globally. Thus, the main objective of this present work is to fabricate Si nano/microstructure by using MACE process and then utilizing these Si substrates for detection of the methylene blue (MB).

Different nano/microstructures were fabricated on Si by using noble metals catalyst such as gold (Au) and silver (Ag). The effect of different etching parameters such as thermal annealing of the metal catalyst, effect of the concentration of the oxidising agent, those are directly associated with the MACE process were investigated. The experimental results revealed that the thermal annealing process eliminated the pin-holes present in the metal catalyst when 50 nm thick Au acted as metal catalyst and successfully fabricated deeper micro-trenches on Si substrates than the un-annealed counterpart of it. Moreover, it also indicated that higher thickness of the metal catalyst micro-stripes help to fabricate flat bottom type deeper trench than the thinner counterpart. Furthermore, the mechanism for the obtained results are discussed in the thesis. The morphological effect of the metal micro-stripes was also examined and the results indicated that various nano/microstructures could be fabricated by controlling the morphology of the used metal catalyst.

As it is very well known fact that the SERS detection limit or enhancement of Raman signal primarily depend on the fabricated nano/microstructures present on the surface of the Si substrate and incorporated with the noble metal (Ag) nanoparticles. The performance of the Si-based SERS substrates was tested for the chemical detection of MB with very low concentrations starting from nM to pM, and the result indicated that nanostructured Si substrate showed better SERS detection than its microstructured counterpart. The probable reasons for such behaviours are also discussed.

More studies were also carried out to enhance the detection limit of the MB, since higher the detection limit is better for the usability of these substrates for molecular level detection of different chemical species. Thus, combination of discontinuous Au film and Ag nanoparticles (NPs) were deposited on the nanoporous Si substrates, those were obtained by MACE process and the result suggested that the detection limit of MB can be further improved by depositing discontinuous Au thin film with various thicknesses. It is also noticed

from the experimental results that up to certain thickness of the Au discontinuous thin films, it helps to improve the limit. On the other hand, higher thickness of the Au discontinuous thin films, degrades the detection limit. Thus, there is a direct correlation between the detection limit and the thickness of the Au discontinuous film on the nanoporous Si substrate. Our experimental findings suggested that the best detection could be achieved when a combination of 30 nm Au discontinuous thin film and Ag NPs were used for preparation of the SERS-active substrates which can detect 10 pM MB. Furthermore, highest enhancement factor of the order of 10^8 is also achieved with this same combination of Au discontinuous thin film and Ag NPs.

Thus, we believe that the prepared SERS-active substrate in this work can have the capability to detect MB at molecular level. We believe that the easy, simple and reusable SERS-active substrates will be more helpful to develop chemical sensors to detect molecular level chemical species other than MB with higher enhancement factor and can be utilized for the food safety, environmental monitoring, security and medical diagnosis in the near future.

Contents

Chapter 1: Introduction

1.1 Introduction	2
1.2 Fundamentals of MACE and SERS	3
1.3 Literature review on MACE of Si	7
1.4 Literature review on nano/microstructure based SERS measurement of chemical species	22
1.5 Current challenges	28
1.6 Objectives of the thesis work	30

Chapter 2: Microfabrication of the metal micro-stripes on p-Si (100) substrate

2.1 Introduction	32
2.2 Fabrication of Au/Ag micro-stripes on p-Si (100) substrates	32
2.2.1 Cleaning of p-Si (100) substrates	32
2.2.2 Patterning of positive photoresist on the cleaned Si substrates	33
2.2.3 Deposition and characterisation of thin films	34
2.2.3.1 Deposition and characterisation of Au thin films by RF sputtering	34
2.2.3.2 Deposition and characterisation of Au and Ag thin films by thermal evaporation	38
2.2.3.3 Deposition and characterisation of Au thin films with the different source to target distance	41
2.2.4 Lift-off process for the patterning of Au/Ag thin films on Si	44
2.3 Characterisation of the metal micro-stripes fabricated on Si substrate	45
2.4 Conclusions	47

Chapter 3: Metal-assisted chemical etching of Si by using Au/Ag micro-stripes as catalyst

3.1 Introduction	50
3.2 Experimental procedure for MACE of Si	50
3.3 Effect of different metal catalysts on the formation of Si micro/nanostructures	51
3.3.1 20 nm Au/Ag micro-stripes as catalyst	51
3.3.2 Effect of thermal annealing of metal micro-stripes on the formation of Si micro/nanostructures	53
3.4 Effect of the thickness of Au micro-stripes on the formation of Si microstructures	55
3.5 Effect of morphology of the metal catalyst on the formation of Si microstructures	63
3.6 Conclusions	68

Chapter 4: Application of nano/microstructure-based Si substrates for SERS detection of chemical species (MB)

4.1 Introduction	71
4.2 A brief about SERS	71
4.3 Experimental procedure for SERS detection	72
4.4 SERS detection by the micro/nanostructured Si substrate	72
4.5 Effect of discontinuous Au thin film on SERS detection limit	77
4.6 Combined analysis of all the Si-based SERS-active substrates fabricated by MACE	84

4.7 Conclusions	86
Chapter 5: Applications of Si nanopores based substrates for SERS detection of chemical species (MB)	
5.1 Introduction	89
5.2 Deposition of Ag NPs on Si substrate and its characterisation	89
5.3 Characterisation of the commercially available Ag NPs	90
5.4 MACE of Si by using Ag NPs deposited by dip and spin coating process	
92	
5.5 SERS measurement by nanoporous Si substrates fabricated by Ag NPs assisted MACE process	94
5.6 Conclusions	95
Chapter 6: Summary and conclusions	96
Chapter 7: References	101

CHAPTER 1

Introduction

1.1 Introduction

Silicon, the second highest abundant element in Earth's crust has become the highly demanding material as it is the base material for various applications such as electronics, photovoltaics, microelectromechanical devices etc. Recently, much attention has been given to developing Si-microstructure or nanostructures for using these in several applications. Basically, microstructure and nanostructure Si include the nanowires (NW), nanoholes (NH), nanometer depth micro trenches etc. and have shown excellent performances in the field of energy storage, harvesting, optoelectronics and sensors. For example, Silicon nanowires (SiNWs) show significantly reduced thermal conductivity as compared to the bulk Si and has considered as the excellent thermoelectric material. Also, these SiNWs are a promising material for the anode material of Li-ion battery [1] and sensor applications due to its high surface to volume ratio which enables them to offer high sensitivity, selectivity and stability. Moreover, monocrystalline SiNWs have also shown better photoelectric properties [2] and it has been recently reported that it can be used in the preparation of SERS-active substrate for chemical detection [3-7]. Thus, development of Si-nano and microstructure is an emerging research area for SERS application.

One of the important criteria in the nano/microfabrication is the cost and hence, cost-effective and simple methods to fabricate Si micro/nanostructures by using both top-down or bottom-up approaches [8]. Among all the existing methods, MACE is more cost-effective and simple process to fabricate different micro/nanostructures on Si substrates. As the research on fabricating different micro/nanostructures on Si by MACE process have received numerous success, simultaneously many researchers put effort to utilise these structures in the practical applications. Basically, Si micro/nanostructures have been used in several potential applications such as in energy conversion [9,10], sensors [11,12], and nanoelectronics [13,14]. Among all the various applications of Si micro/nanostructures, recently, SiNWs have been used as the supporting SERS substrate because of its unique mechanical and optical properties. Moreover, the Si nanostructures (such as nanoparticles, nanopillars) show low-loss optical resonance in the visible region and which provide the light scattering and hence can be used as a favourable SERS substrate [15,16]. An overall representation of different applications of MACE technique to fabricate nano/microstructures on the surface of Si which has been used in various fields can be seen in Fig.1.1.

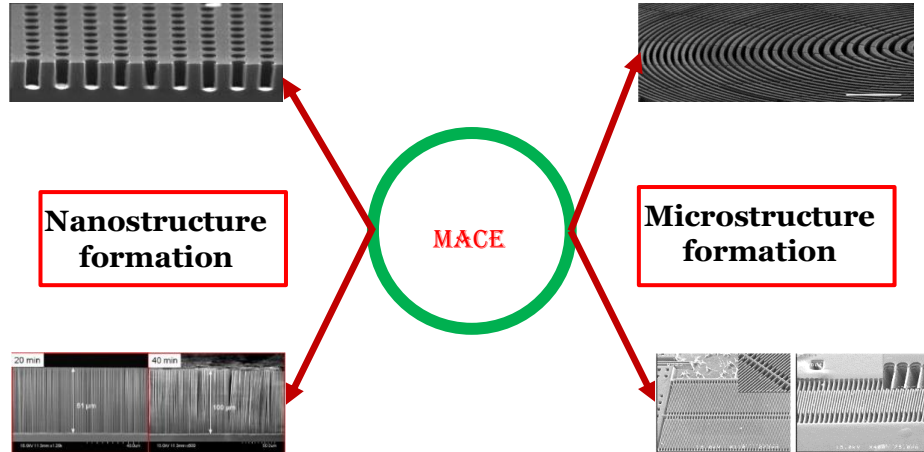


Fig.1.1: Various applications of MACE technique in nano/microstructures fabrication on Si substrates

1.2 Fundamentals of MACE and SERS

Out of all the different existing techniques mostly apply to fabricate micro/nanostructures on Si, a simple and cost-effective technique which is called Metal-Assisted Chemical Etching (MACE). It has shown its versatility over others [17]. Different Si nanostructures, for example, Si nanowires (SiNWs), porous SiNWs, Si nanopores are being fabricated on the Si substrate. This simple MACE technique was first used and explored as the electroless etching technique where porous Si and porous III-V compound semiconductor were produced by Li et.al. in 2000 [18] and 2002 [19] respectively. In their work, they studied the formation of porous Si (PSi) with different morphologies and also the variation in the light emitting properties by using different types of noble metals along with the different doping type and doping level. They found that the columnar pores with bigger sizes were formed in the metal coated areas, whereas the off-metal areas exhibited randomly oriented pores with smaller pore diameters (Fig.1.2).

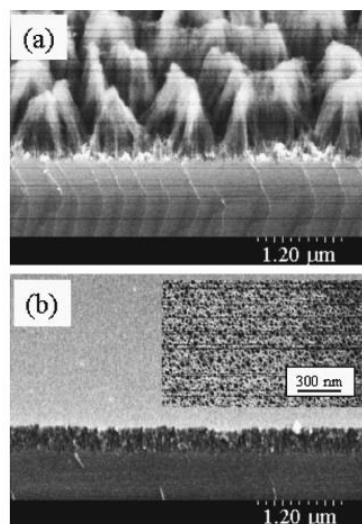


Fig.1.2: SEM images of post etching Pt-coated Si (100) substrate etched in HF/H₂O₂ solution for 30 s. (a) Pt-coated area on p+ Si, (b) off the Pt-coated area on p+ Si [18].

The MACE is an anisotropic wet etching technique where etching occurs in an etching solution comprising of H_2O_2 and HF where noble metals such as Gold (Au), Silver (Ag), Platinum (Pt) etc. are used to induce local oxidation and reduction reactions under open circuit. Initially, the noble metal had been understood to only catalyze the oxidative half-reaction where charge carriers (holes) are generated and then dissolve the material by another oxidative etching half-reaction [20]. In regard of hole generation during the MACE process, Chattopadhyay et al. [21] suggested that when a Pt-loaded Si substrate is dipped in a solution comprised of HF/ H_2O_2 / H_2O the generated holes injected via loaded Pt particles, deeply into the valence band of Si. For a better understanding of the whole mechanism, a diagram of energy levels of Si and also the electrochemical potential of $\text{H}_2\text{O}_2/\text{H}_2\text{O}$ has been reported by them, as shown in Fig. 1.3.

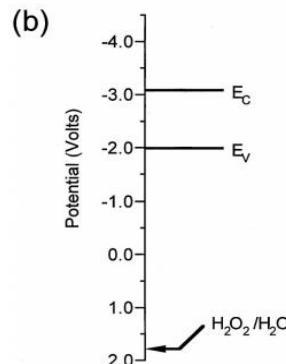
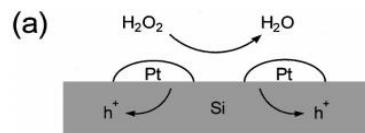
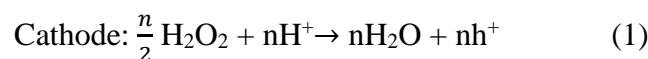
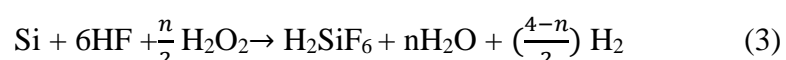


Fig.1.3: (a) Scheme of the H_2O_2 reduction at Pt nanoelectrodes and injecting holes into the Si substrate for the initiation of etching. (b) Comparison of band edge energies of Si and the redox potential of $\text{H}_2\text{O}_2/\text{H}_2\text{O}$ on the electrochemical energy scale and which indicates that injection of holes occurred deep into the valence band [21].

Despite different mechanisms are used to explain the MACE process, it has been widely accepted that the MACE process occurs due to a pair of redox reactions occurring at two different interfaces such cathode (Au-liquid interface) and anode (Au-Si interfaces) [22].



So that the balanced reaction:



In general, H_2O_2 reduces at the catalyst surface which is negatively charged [23] for $\text{pH} > 3$ in all possible HF concentrations [24]. Because of this negative charge, the H^+ ions are attracted to the vicinity of the catalyst surface. This cathodic reaction produces water and at the same time holes (h^+) are injected through the catalyst to Si. On the other hand in the anode (the Au-Si interface) the Si atoms which are underneath the catalyst are oxidized by the holes and dissolve in the HF solution as H_2SiF_6 . Few more research attempts were also reported to understand the effect of relative concentrations of HF and H_2O_2 on MACE process. In this regard, Chartier et al. [25] found a few different regimes of dissolution which varies according to the relative concentrations of HF and H_2O_2 . They have suggested that the concentration of H_2O_2 can be deliberated as the equivalent to the current density in electrochemistry and below or above the critical current density (J_{PS}), porous Si formation or polishing occurs.

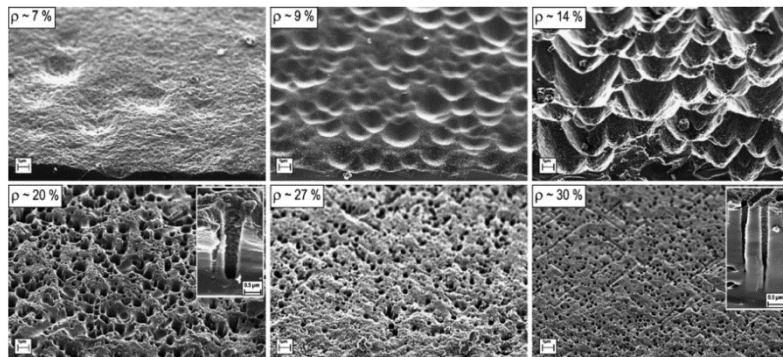


Fig.1.4: SEM images (at 45°) of post etched p-Si (1 0 0) etched with HF- H_2O_2 of different values [25].

An unusual behaviour in the pore formation was observed which shows the cone-shaped pore formation with a larger diameter than the Ag NPs dimensions used in the MACE process. They have proposed a mechanism which indicates that with the decrease of HF/ H_2O_2 proportion, the holes which generated during the process get injected and diffused away from the tip of the pore which is due to the growth of an oxide layer in the Si/Ag interface ($J_{tip} > J_{PS}$). Due to this, hole diffusion happens on the pore walls as the spread current (J_{walls}) is lower than J_{PS} and in process microporous Si forms on the pore walls.

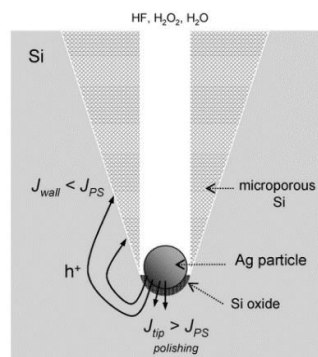


Fig.1.5: Graphical representation of the proposed mechanism of cone-shaped pore formation in HF- H_2O_2 solutions with ρ between 20% and 70% [25]. 5

The Surface-enhanced Raman spectroscopy(SERS) [26-28] has recently attracted much attention from its discovery in 1974 and becomes the most capable analytical tools for detection of single molecule level [29] of the biological and chemical species in both liquid and as well as in the gas phase [30-34]. After the first reported work on the enhancement of the Raman signal by Fleischmann and co-workers [35] with pyridine molecule on the rough surface of silver, many new avenues such as biology [36], catalysis [37], medicine [38], bioimaging and other allied fields have opened up. In their study, they had used an Ag electrode for Raman measurement of pyridine molecule and found the changes in the Raman spectrum when it was examined close to the surface of the electrode. The changes in the Raman spectrum is shown in Fig.1.6.

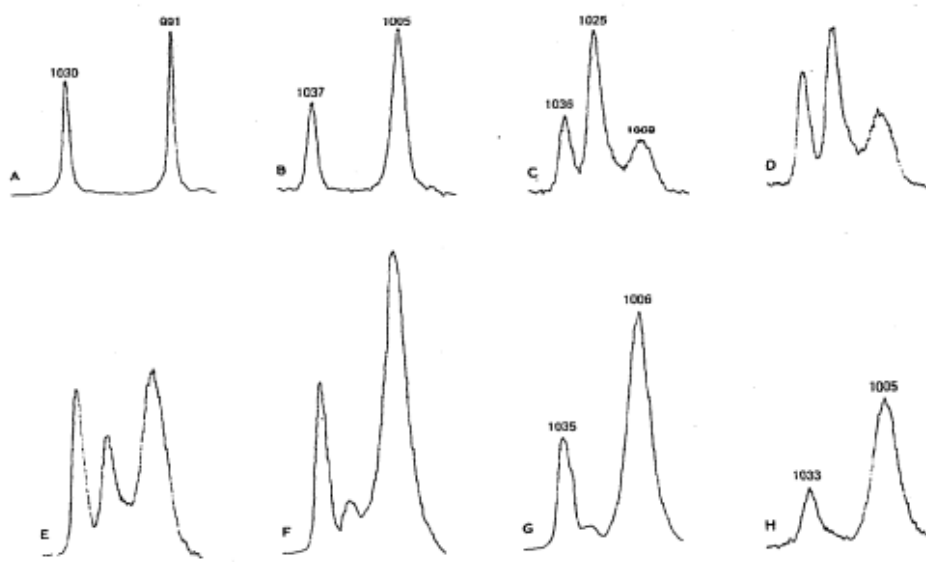


Fig.1.6: Raman spectra of liquid pyridine and at the Ag electrode. (A) liquid pyridine; (B) 0.05 M aqueous pyridine; (C) Ag electrode 0 V (S.C.E.); (D) -0.2 V; (E) -0.4 V; (F) -0.6 V; (G) -0.8 V; (H) -1.0 V [26].

The research carried out by Jearmaire and Van Duyne [39] with Albrecht and Creighton have indicated that SERS phenomenon mainly occurs by the electromagnetic field enhancement rather than the molecules saturate on the surface of the electrode. But, after a few years, Otto reported that it is due to the charge transfers between a metal surface and molecules [40]. Later, several researchers have proposed different mechanism for the enhancement of the Raman signal. In this regard, a critical analysis was carried out by the T. E. Furtak and J. Reyes [41] and they have proposed theoretical models and tried to provide the practical implications of these models. They have evaluated those theories from the Physics point of view and found that the microscopic theories forwarded by Fuschs and Burstein, Chen, Chen, Lundqvist and Tossatti [42]. However, no proper calculations were provided to support their theories and also made few simple predictions based on the experimental behaviour where

they pointed out for the first time that the excitation of the electron-hole pair in the metal is mainly responsible for this Giant Raman effect. But, later on, and till today numerous explanations have been reported by many researchers about the SERS enhancement factor. But, it has been broadly accepted that the electromagnetic field enhancement (EM) and chemical enhancement (CE) contribute to the SERS enhancement factor [43,44]. In this case, M. Moskovits et al. [45] have provided a brief explanation about the SERS enhancement of $\sim 10^{11}$ which was achieved by Xu et al. [43]. This giant enhancement was obtained when two nanoparticles brought very much close to each other (i.e. <1 nm) and the molecules reside at the spot between the two nanoparticles.

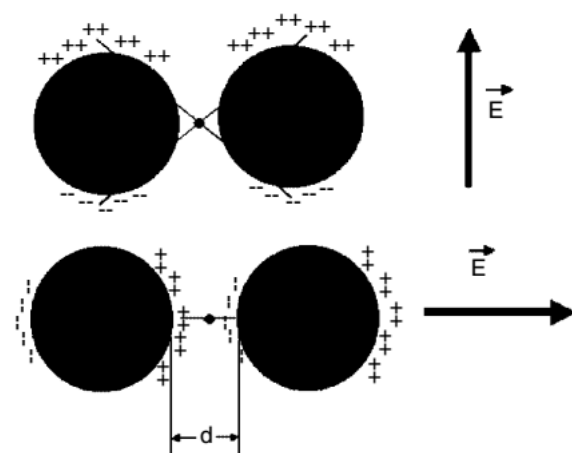


Fig.1.7: Schematic representation of the reason for the polarization of light with E vector along the inter-particle axis which can result in huge enhancements in the gap between the two NPs while the orthogonal polarization cannot. For the polarization of light along the inter-particle axis the proximity of the charges (induced by the optical fields) to the molecule can be made small arbitrarily and hence the field detected by the molecule is commensurately large as the NPs are brought closer together. This capability is not existing for light polarized orthogonally to the inter-particle axis [45].

From Fig.1.7, it is clearly seen that when the molecule (indicated by the small circle) are placed in the gap between the two metal nanospheres, a conjugate charge arise due to the individual polarisation of each nanoparticle. Similarly, the chemical enhancement is contributed by the chemisorption process such as the charge transfer between the adsorbate and substrate driven by the photons and also the coupling effect produced between the adsorbed molecule and electron-hole pair. In recent years, Mullin et al. represented a combined theory where he exclusively included the small metal clusters in the quantum chemical part by using Mie theory so as the impact of chemical and electromagnetic enhancement could be studied together [46].

1.3 Literature review on MACE of Si

In recent years many new findings related to MACE have been reported that indicating the importance of the factors such as the concentration of the etching solution [47], the extent of

coverage of the metal catalyst [20] and geometrical feature of the catalyst material [48]. In general, all these factors are mainly responsible for the etch rate, porosity and crystal direction. Therefore, more research efforts are still going on only to understand the mechanism behind the MACE process for better control on the nanostructure formations. Similarly, few researchers have demonstrated to understand the effect of the ratio of etchant concentration to the oxidising agent where the change in the etchant concentration radically change the crystallographic direction and porosity of the SiNWs. In this context, k. Tsujino et al. [49] discovered that the lower HF concentration creates porous layers on the sample surface.

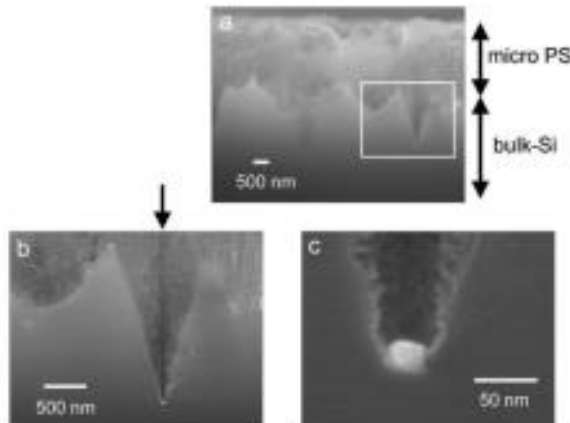


Fig.1.8: Cross-sectional SEM images of the sample where etching was done in a mixed solution of 50% HF, 30% H₂O₂, and H₂O at a volume ratio of 2:1:8 (lower concentration of HF solution) for 5 min. (a) Overview image. (b) Enlarged image of the area marked in (a) by a rectangle. (c) Enlarged image of the nanoparticle observed at the bottom of the concavity [49].

On the other hand, with a higher concentration of HF, helical pores are obtained which was explained by the fact that a very thin layer of oxide was formed in the Pt-Si interface due to the faster dissolution of this layer.

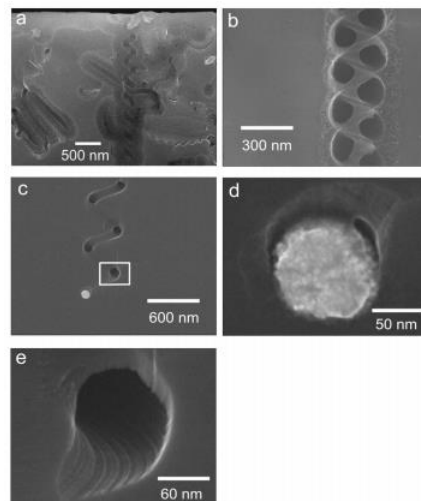


Fig.1.9: Cross-sectional SEM images of the generated holes in Si when etching was carried out in a mixed solution of 50% HF and 30% H₂O₂ at a volume ratio of 10:1 for 5 min. (a) Overview image of the holes noticed in the sample. (b) A typical helical hole observed in the sample. (c) Image near the bottom of a helical hole. (d) Enlarged image of the particle detected at the bottom of the hole shown in (c). (e) Enlarged image of the area marked in (c) by a rectangle [49].

Inspired by such results related to nanohole formation, researchers have demonstrated the synthesis of SiNWs by using the MACE technique. For instance, K. Peng et al. [50] found out that depending on the density of the deposited metal nanoparticles on Si substrates, nanopores to nanowires can be formed in Si by using the same etching conditions. According to their findings, metal particles with high density helps in forming SiNWs. On the other hand, when the metal particles are well dispersed and well separated from each other, well-separated nanoholes are tunnelled straight into the Si substrate. The electronic structure and the physical properties of these 1D Si nanostructures can be influenced by the axial crystallographic orientation. As reported by Holmes et al. [51] where they have utilized supercritical solutions to synthesise Si nanowires with controlled thickness and orientation. In their study, they discovered that the formation of the nanowires with preferred axial orientations depends on the pressure incorporated into the synthesis process. Peng et al. [52] have synthesized 1D Si nanostructure by using a two-step method. In their process, initially, a thin film of metal nanoparticles was first deposited on the cleaned Si surface by electroplating method and followed by an etching process carried out with HF/Fe(NO₃)₃ solution. The electroless deposition mechanism of the Ag particles from HF/AgNO₃ solution was proposed by them which include both cathodic and anodic reactions. The schematic of the whole process is shown in Fig.1.10.

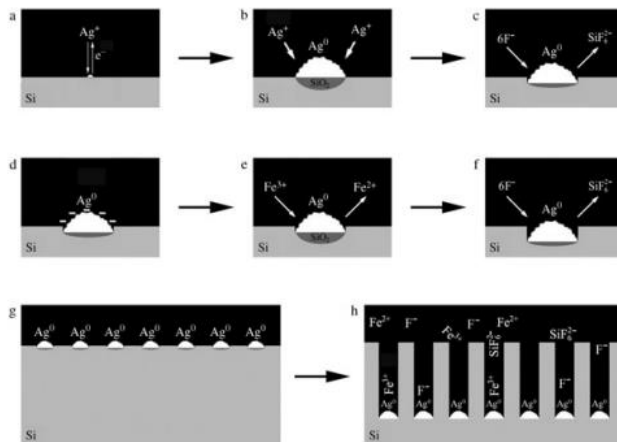


Fig.1.10: Schematic of the deposition of Ag by an electroless process on Si in HF/AgNO₃ solution and the Ag NP-catalyzed chemical etching of Si in HF/Fe(NO₃)₃ solution. (a–c) Nucleation and growth of Ag NPs on the surface of Si in HF/AgNO₃ solution: SiO₂ forms concurrently underneath the Ag NPs, and form pits as a result of etching away of SiO₂ in HF solution. (d–f) Reduction of Fe³⁺ ions, Si etching, and sinking of Ag NPs in HF/Fe(NO₃)₃ solution: deeper pits are formed by the Ag NPs. (g) Arrays of Ah NPs form on the Si surface. (h) Deep pores form in the bulk Si in HF/Fe(NO₃)₃ solution as an outcome of the constant etching away of SiO₂ underneath the Ag NPs [52].

Peng et al. [53] have reported that during the MACE process, the noble metal particles (Ag and Au) follow a highly uniform motion in the [100] crystallographic orientation of Si.

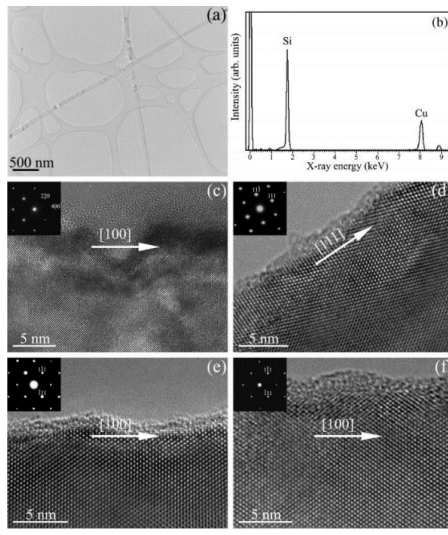


Fig.1.11: TEM images of Si nanowires. a) Low-magnification TEM image and b) EDX of Si nanowires fabricated from p-type Si(100) wafer. HRTEM images of a Si nanowire fabricated from c) p-type Si(100) wafer, d) p-type Si(111) wafer, e) p-type Si(110) wafer, and f) n-type Si(113) wafer [53]

This finding directly contradicts the earlier claims of many researchers where they pointed out that the sinking of metal particles always occur in the perpendicular direction to the surface of the Si substrate in use [54-57]. They have mentioned in their study that long nanowires those form along the [100] axial orientation, the nanowires axis is perpendicular to the (100) lattice plane. They proposed a new mechanism which basically led to an electrokinetic model (self-electrophoresis) which describes the noble metal particles' mobility in Si and in the presence of oxidising HF. According to their explanation, the motility of Ag particles governs by a process similar to electrochemical fuel 'combustion' where the chemical energy is converted into mechanical power locally by catalytic transformation and transformed to the surface of Ag particles by a spontaneous bipolar electrochemical reaction.

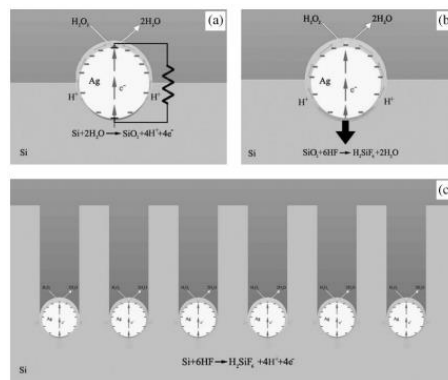


Fig.1.12: Scheme of the electrokinetics for autonomous movement of Ag particles in bulk Si induced by catalytic reactions: a) A self-generated electric field results from a hydrated proton gradient across the Ag particle. b) Motion of Ag particles by self-electrophoresis. c) Schematic of the collective and extended tunneling motion of Ag (or metal) particles in the matrix of Si and which leads to formation of Si nanostructures [53].

They have further studied the influence of buoyancy or gravity in the motility of the Ag particles during the MACE process. They have also demonstrated another experiment where they coated Ag particles on every surface of the Si substrate and carried out the MACE for the same substrate. They had observed that Ag particles dig into the Si substrate from all the directions, these results indicate that the self-electrophoresis is the preliminary force for the motility of the Ag particles during MACE process. Hildreth et al. have reported that the shape of the catalyst, method of fabrication, and the composition of the etchant significantly influence the etching direction. Due to this, etching of nanostructures are not only possible vertically to the substrate surface, it is similarly possible to obtain different nanostructures such as 3D spirals, twists, cycloids, slanted channels, and “S-shaped” undercuts with feature size ranging from hundreds of nanometers down to tens of nanometers [57]. In their work, they have used three different catalysts, such as chemically synthesized Ag nanorods, Ag nanodonuts along with electron beam lithography (EBL) patterned Au nanostructures. In case of Ag nanorod catalysts, straight and cycloid channel, i.e. Ag nanorods etch below the Si surface is obtained and when the etching direction was changed to etch through the top surface remerging at some distance away as shown in Fig.1.13. The source of cycloid like motion has been explained by Hildreth et al., that the addition of local perturbations, for example non-uniform instantaneous reduction and oxidation rates and acceleration due to Brownian motions are mainly responsible for this unique motions of Ag nanorods throughout the Si surface. On the other hand, in the case of Ag nanodonuts, etching occurs almost vertically to the Si surface with a minute rotation about the Z-axis as shown in Fig.1.13. They have also studied some complex structure built by Au nanolines where they used electron beam lithography (EBL) to fabricate Ti/Au nanostructures with a combination of 10 nm base adhesion layer of Ti followed by 50 nm Au catalyst metal consisting of discs, lines, ‘dog-bone’ shapes, squares, stars and grids by maintaining line widths ranging from 200 nm to 25 nm as shown in Fig.1.14. They have reported the penetration and etching direction on Si surface varies with the width of the line of Au nanolines. For example, 200 and 100 nm line widths remain closer to the surface and slicing just below the surface, whereas 50 and 25 nm line widths penetrate further into the Si and resurface rarely.

Hildreth et al. showed that the catalyst shape, catalyst fabrication method, and etchant composition significantly impact the direction of etching [57]. Thus the etching nanostructures are not only perpendicular to the substrate surface, it is also possible to build different nanostructures such as 3D spirals, twists, cycloids, slanted channels, and “S-shaped”

undercuts with feature size ranging from tens of nanometres up to hundreds of nanometers [57].

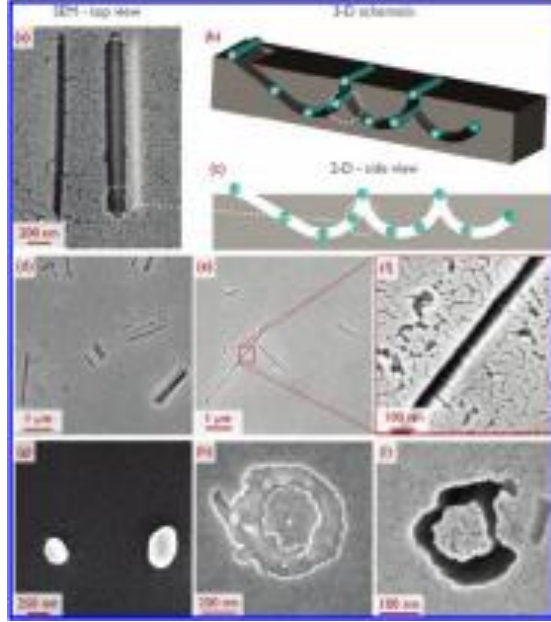


Fig.1.13: Post UV ozone PVP removal by etching with Ag nanorods and nanodonuts where $\rho=90$ etchant for 10 min. was used (a) Top view SEM image. Ag nanorod started moving at left-hand hole, etched into Si and re-immersed after 300 nm and then again etched back into Si. Ag nanorod are noticed just below the surface of Si on the far right. (b) Etching path with 3D schematic. (c) 2D side view schematic of etching path. The circles with white dashed on the images highlight the Si wedge remnant just underneath the top surface on all three images. (d) Cycloid-like and straight paths; nanorod channels' width range from 60 to 80 and 500 nm to 1.5 m long. (e) Straight channels ranging between 30 and 60 nm wide and 430 nm and 3.4 m long. (f) Higher magnification of image (e) showing 30 nm wide channel. 5 nm Au were coated on the samples after etching for enhanced (g) Ag particles of sub-micrometre size before UV ozone treatment; (h) Ag nanodonut just below the Si surface; (i) Ag nanodonut etching path after 10 min of etching. [57].

They have also reported that depending on line widths of Au nanolines and dog-bone shape, penetration and etching direction on Si surface varies. For example, 200 and 100 nm line widths remain closer to the surface and slicing just below the surface, whereas 50 and 25 nm line widths penetrate further into the Si and resurface rarely.

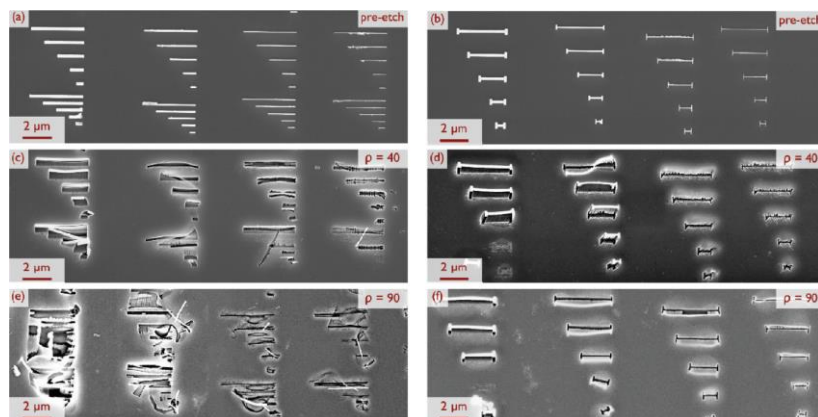


Fig.1.14: SEM images of Si etched for 40 minutes by the Au catalysts patterned with EBL. Left column shows Au nanolines. Right column shows Au dog-bone shapes. From left to right line widths are 200, 100, 50, and 25 nm [57].

Yongquan Qu et al. [58] have proposed that the formation of NWs are catalysed by the deposited metal NPs, whereas the porosification of the NWs happens due to the increase of the concentration of Ag^+ ions in the etching solution. Also, it has been reported that the concentration of H_2O_2 plays the major role in the porosification. When the concentration of H_2O_2 increases, Ag^+ ions concentration also increases and hence there is a possibility that the recovery of Ag^+ ions to Ag NPs may not be 100%. Due to the excess availability of the ions, the Ag^+ diffuse out and when it reaches a certain threshold, these ions start to nucleate in the weak and defective sites of the Si NWs (side walls) by removing an electron from NWs. During this process, new Ag NPs are formed and the etching occurs in the lateral dimension of the NWs. However, as per reported work by Ciro Chiappini et al. [59] have suggested that the formation of SiNWs is catalysed by the NPs, whereas the metal ions present in the solution catalyse the porosification.

It has been reported that two different catalytic activities such as the relative catalytic activity of ions (C_i) which determines the porosification rate and the catalytic activity of the NPs (C_n) that determines the etch rate of the SiNWs. Mathematically C_i and C_n can be explained as shown below [59],

$$C_i = v_p = \frac{\Delta x_p}{\Delta t_p} \quad (1)$$

$$C_n = v_e = \frac{\Delta x_e}{\Delta t_e} \quad (2)$$

where Δx_p is the porous layer thickness during a porosification time Δt_p and Δx_e is the nanowires' length obtained during an etch time Δt_e . It has been reported that the increase of ethanol concentration in the etching solution, the morphological transition occur in the NWs which they can be explained by the catalytic activity ratio (C_0) as

$$C_0 = \frac{C_i}{C_n} = \frac{v_p}{v_e} = \frac{\Delta x_p}{\Delta x_e} \quad (3)$$

In detail, the increased concentration of ethanol reduces the v_e which in turn reduces the C_0 and increases C_i . Thus the porosification rate changes due to the change in the ion's concentration in the etching solution.

Likewise few researchers have reported on the effect of H_2O_2 on the MACE process and mentioned that the concentration of H_2O_2 influenced the nanowires' morphology and surface characteristics [2]. Three different concentrations of etching solution composed of HF, H_2O_2 , and H_2O (the volume ratios are 20:10:70, 20:20:60, and 20:30:50) were chosen in their work,

so that the concentration of H_2O_2 was recorded as 10%, 20% and 30% respectively) and found that for different concentrations such as 10%, 20%, and 30%, SiNWs with different morphologies of high-density nanowire arrays, low-density nanowire arrays, and a chaotic porous nanostructure were formed respectively.

Similarly few researchers have also tried to understand the actual role of Ag during Si etching by MACE method. In this regard, Abouda-Lachiheb et al. [60] have demonstrated the dual role of Ag during the nanostructure formation. In their study, they have followed two different Ag deposition methods on Si, which are known as one step method and two-step method. In one step method, the metal deposition and etching happen at the same point of time, whereas two-step method includes the metal deposition (by evaporation or chemically formed on the surface) and subsequently the chemical etching.

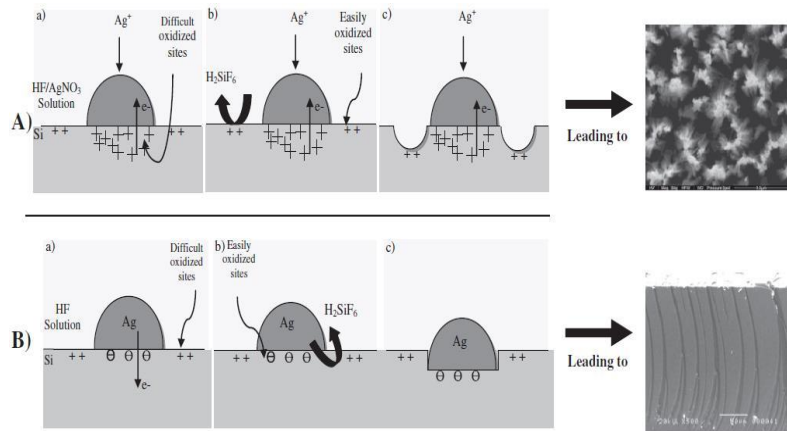


Fig. 1.15: Scheme of the etching mechanism. (A) the one-step process and (B) the two-step process [60].

They have proposed that the effect of electron transfer at the interface of Ag/Si plays the vital role in determining the etching behaviour of Ag on Si surface. In this regard, Yongkwan Kim et al. [61] have carried out research on the effect of co-solvent for tuning the curvature of the SiNWs by MACE process. They have demonstrated that by simply changing the type and amount of co-solvent in the etching solution, the directionality of the NWs could be changed. They have observed that by adding a small amount of 2-propanol, unidirectional curved SiNWs were formed over a large area. By increasing the concentration of this co-solvent, they were able to produce almost straight and tilted NWs.

Previously, many researchers [62, 63] have reported that the formation of slanted NWs depends on the orientation of the Si wafer. They have suggested that as the Si back-bond is weak in $<100>$ direction, preferred etching occurs in this direction. Thus, the non-vertical SiNWs formed only in those wafers other than (100). But, Yongkwan Kim et al. have demonstrated the diffusion of the reactants also plays a major role in the curvature and

directionality of the SiNWs. Similarly, a research work carried out by G. Liu et al. [64] has brought a new insight to the MACE process, where they carried out experiments to understand the role of exposed nanoparticle's surface in the etching process. In the process, they deposited different types of anisotropic Au nanoparticles and performed chemical etching with HF/H₂O₂. According to their reported results, the anisotropic nanoparticles had extremely faceted surface and which determined the etching rate of the MACE process. They deposited two different anisotropic nanoparticles such as Au triangular nanoprisms with {111} and Au nanocubes with {100} surface facets respectively.

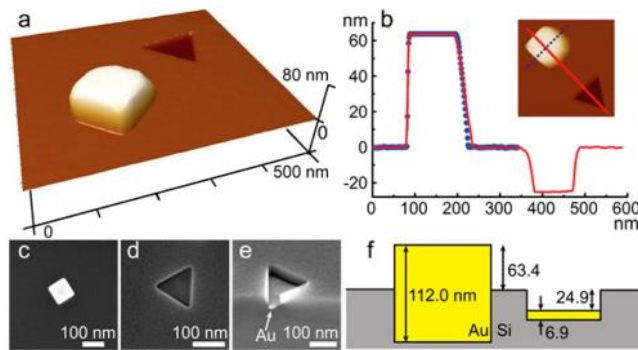


Fig. 1.16: (a) Post etching AFM height images of an Au nanocube and an Au nanoprism on a substrate of Si after etching for 20 min. One part of the cube is above the surface, whereas the entire nanoprism is within the etched triangular trench in the Si substrate. (b) AFM height profiles of the etched structures. The inset shows the direction of the line scans. (c, d) Top-down SEM images of (c) a nanocube and (d) a nanoprism after etching for 20 min. (e) Cross-sectional SEM image of a nanoprism in a Si trench at a 45° tilt angle. (f) Schematic representation of the side view etching depths obtained using a nanocube (yellow square) and a nanoprism (yellow rectangle) [64].

They have reported that nanocubes showed a faster etching rate than the nanoprism despite the same etching time and solution was used for the etching process. Their studies revealed that higher the surface energy of surface, a higher catalytic activity occurs with easier hole injection to Si and which led to higher etching rate. A. Backes et al. [65] have tried to address two key issues related to the doping level of the substrates such as for the highly doped substrates, nanometre-sized porous structures were formed in uncovered areas by metal NPs [66,67] and secondly to understand the impact of doping level on the etch rate. They have reported that in highly doped Si, etch rate decreased and which led to the formation of the porous substructure. They have suggested that with higher doping concentration diffusivity of the charge carriers from the metal-semiconductor increases and that reduces the charge density in the surface. Therefore, the etch rate decreases during the MACE process. On the other hand, at the lower doping concentration, the injected holes stay for longer in the metal-Si interface and which enhances the material removal in those areas where Ag NPs.

As it was easily accepted by the research community that during MACE process hole injection occur in the metal/Si interface. But, this concept of hole transfer was challenged by a work carried by K W Kolasinski et al. [68]. They have proposed a new mechanism based on the band structure of the system. They have chosen four noble metals such as Au, Ag, Pt and Pd and prepared that the holes injected to Ag are less stable either in Si or at the interface of Ag/Si than the Ag itself. Similarly, in case of other three metal catalyst such as Au, Pt and Pd, the injected holes move immediately to the interface of metal/Si, where the band bending restrict the movements of these holes to the Si surface. Due to this, there is no possibility of holes diffusion from the metal particles to the Si and also injection of holes are not possible from the Ag catalyst.

In the explanation of anisotropic etching by the metal particles, they have suggested that as the positively charged particles are not injected to the Si, mostly they are trapped in the metal nanoparticles or at the interface with Si they have created an electric field and that can be considered as the local anodic power supply. Depending upon the voltage created, etching occurs locally and form a etch track which is roughly similar to the size of the nanoparticles.

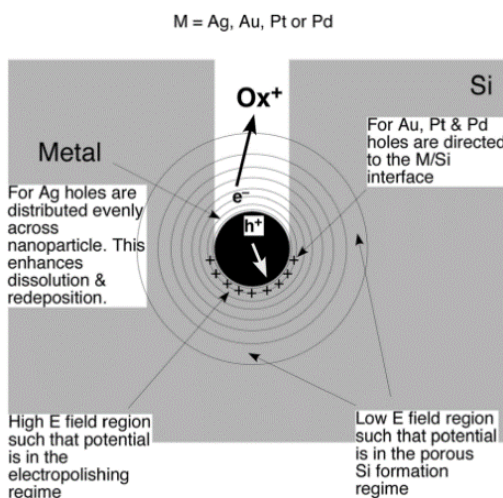


Fig. 1.17: The mechanism associated with metal-assisted etching. Accumulation of charge on the metal nanoparticle generates an electric field. Adjacent to the particle, the effective applied voltage is sufficient to push etching into the electropolishing regime, which facilitate the formation of an etch track which is approximately the size of the nanoparticle. Further way, the lower voltage corresponds to the formation of porous silicon regime [68].

Moreover, in the vicinity of the metal nanoparticle, the potential due to the charge imbalance is sufficiently high enough to carry out the etching with electropolishing character. On the other hand, the potential in far places from the metal nanoparticles is sufficiently high enough to induce etching which leads to form porous Si either by the valence 2 or valence 4 processes. Due to this, alternate and totally different mechanism are possible for nanostructures formation in Si by MACE process. Also, researchers have tried to understand

the effect of Schottky barrier [69] in the MACE of Si. In this aspect, R A Lai et al. [70] have proposed an additional function of metal catalyst in MACE process such as that the metal catalyst doesn't only catalyse the oxidative half-reaction but also form a Schottky junction with the Si which controls the distribution of the injected holes spatially. To understand the effect of Schottky barrier on band bending and eventually on MACE process, they have investigated the effect by using three n-type and three p-type (100) Si substrates with different doping level. The p-type and n-type Si possess the resistivity 0.001–0.01, 0.01–0.1, and 1–10 Ω cm. Their experimental results suggested that n-type Si etches faster than the p-type Si under identical etching solution with the same concentration. They have suggested that in case of n-type Si the Schottky barrier between Au and Si produces an electric field which confines the holes to the surface and for p-type Si, the holes are pulled away from the surface by the electric field. Due to this, the holes which are produced during the MACE process are no more available on the surface of the Si and hence the etching rate slows down in p-type Si than the n-type Si. They have reported that the etch rate for N⁺⁺, N⁺, N-Si are very much similar to different etchant composition whereas, for P⁺⁺, P⁺, P-Si, the etch rate depends upon doping concentration, for instance, higher the doping concentration in Si slower the etch rate. They have explained that as the holes are confined to the surface of n-type Si, saturation happens and hence the etch rates are similar even though doping concentrations are different for N, N⁺, and N⁺⁺ Si. On the other hand, in case of p-type Si, the holes are pulled away and hence the drift velocity of these charge carriers which directly depends on the mobility and electric field at the interface governs the whole etching process. As the drift velocity changes with the doping concentration, the etch rate also varies accordingly.

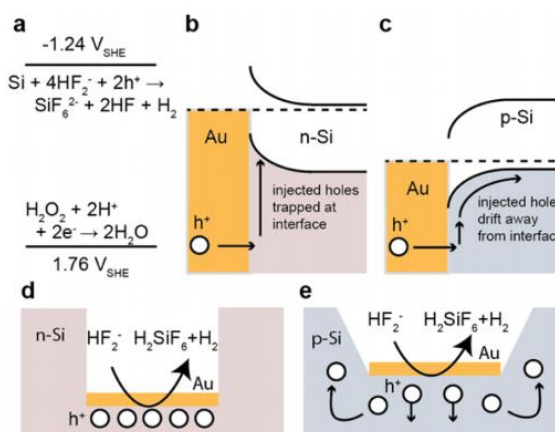


Fig.1.18: (a) Scheme of the reduction potentials of the two half reactions of MACE which is relative to the standard hydrogen electrode, V_{SHE} . (b, c) Band-diagram for n-type and p-type Si in the Au–Si interface, respectively, showing the behaviour of the injected hole carriers by the reduction of H_2O_2 . (d, e) Schematic representation of the resulting morphology for n-type and p-type Si after MACE, respectively [70].

After different parameters related to the MACE process were explored, researchers have tried to understand the mechanism associated with the formation of SiNWs when a continuous metal film is used as a catalyst in Si etching. In this regard, Nadine Geyer et al. [71] have performed a novel research to understand the possible mechanism related to MACE of Si where the continuous metal film is used as the catalyst. They have proposed three different possible mechanisms which can be illustrated as (1) diffusion of reactants and reaction by-products take place through the small pores present in the metal film, (2) otherwise diffusion of reactants and by-products occur through a channel formed at the interface of Si and metal catalyst, or (3) diffusion of Si atoms occur through the metal catalyst thin film and then oxidised and dissolved at the interface of metal and etching solution. These three possible mechanisms as proposed by them is shown in Fig. 16. In their study, it has been proposed that the irrespective of the thickness of the metal catalyst thin film, SiNWs were formed which indicates that the first mechanism may be the correct one and hence they have carried out different experiments to verify the other two proposed mechanism. They have demonstrated that different etching rates for the metal stripes with different lateral sizes and which proved that the second proposed mechanism possibly the correct one.

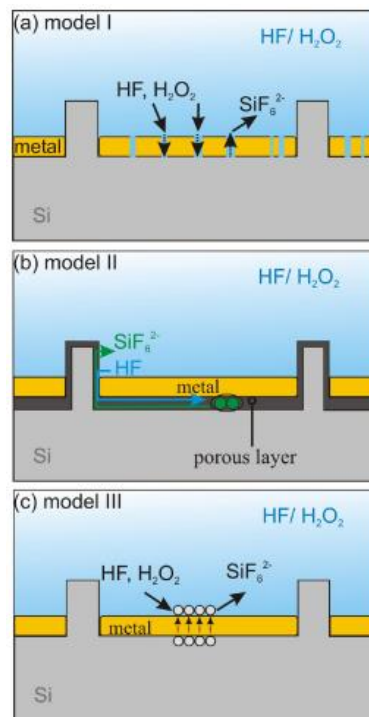


Fig.1.19: Schematic representation of possible diffusion processes of the reactants and reaction products during MACE. (a) Model I: Reactants and reaction products diffuses through a porous thin metal film. (b) Model II: The oxidation of the Si surface proceeds with the formation of a porous Si layer at the interface of the metal and the Si substrate. (c) Model III: Si atoms diffuse through the metal film and are oxidized at the metal's surface. Lastly, Si is dissolved in form of $[SiF_6]^{2-}$ [71].

Similarly, they have also reported that the etching rate remains constant when the thickness was varied and which justified that third proposed model of mass transfer might be not appropriate. Thus, their experimental results have indicated that the second model of mass transfer is more appropriate for the MACE process. However, it has been found that the metal stripes with more than 3 μm width bent during the etching process. They have suggested that as the diffusion length of the reactants species increases due to the increasing distance from the edge of the metal catalyst stripe, etching rate varies from edge to the centre of the stripe [71].

But a recent study proposed that depending on the thickness of the metal catalyst film, the mechanism associated with the etching process may be different. K. Choi et al. [72] have proposed two different mass transport mechanisms which basically depends on the thickness of the metal catalyst film. According to them, Au catalyses the etching reaction by reducing the activation energy of H_2O_2 reduction and also injects holes in the metal/Si interface which oxidise the Si selectively. Moreover, the mass transfer of reactant (HF) and reaction by-product (SiF_6^{-2}) occur differently for thick and thin metal catalyst film. Normally, thin metal catalyst film consists of pinholes and through which mass transport of reactants and by-product occurs during the MACE process. However, for a thick film, the pinholes are absent and due to which mass transport occurs at the edges of the metal/Si interface that leads to a mechanism which is known as the in-plane mass transport. Moreover, the microstructures' depth is higher for a thin metal film catalyst since both in-plane and out-of-plan mechanism occur simultaneously. This combined mechanism possibly helps to etch out Si underneath the metal catalyst concurrently resulting in a uniform etching of the semiconductor surface and without bending of the catalyst.

Furthermore, B. Jiang et al. [73] have tried to understand the movement of the metal particles in the formation of nanopores in Si by MACE process. According to their findings, the concentration of HF plays a vital role in the formation of different helical pores due to its capacity to induce rotation and revolution in the Ag catalyst particles during the MACE process. Moreover, the rotation of the metal particles determines the morphology of the helical pore formed in the Si substrate. They have suggested that the pitch length of the helical pores directly depends on the angle θ . According to hem, a smaller value of θ produces the helical pores with a smaller pitch length.

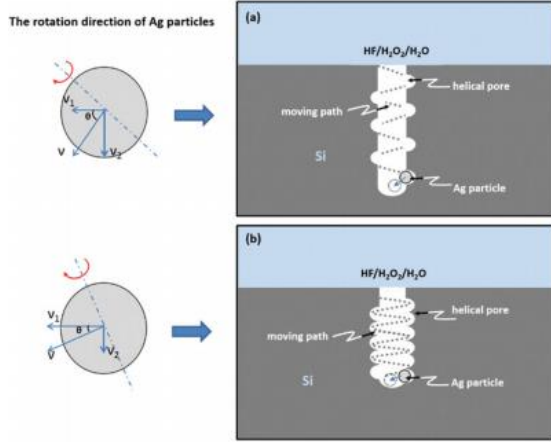


Fig.1.20: Schematic illustration of the Ag particles' rotational direction and probable paths of moving during the forming process of helical pores with various pitches and widths [73].

The nanowires/nanopores formation in Si by MACE process has evolved tremendously over the last two decades, but still, more research efforts are there to building micro/nanostructures in Si. In this regard, Smith et al. [74] have reported a new two-step method to form sub 10 nm nanopores with sub 10 nm interpore spacing where they have used silica-shell gold nanoparticles ($\text{SiO}_2\text{-AuNPs}$) for the MACE process. The silica shell act as the sacrificial spacer layer which separates the Au nanoparticles during deposition. They have reported that after the dissolution of the silica shell, not all the deposited Au NPs take part in the etching of Si. They suggested two possible reasons for such behaviours of Au NPs during etching are (1) after dissolution of the silica shell, few Au NPs possibly contact with the Si surface on the vertex of a facet or on the edge of a crystal grain and hence the hole injection rate differ than a particle which has a planar interface with the Si surface. This difference in the hole injection rate lowers the etching rate for few particles which remain on the surface of the Si after the MACE process, (2) due to the difference in the shell thicknesses of the NPs, the dissolution rate may differ from particles to particles and which may create lack of hole injection from those particles which remain on the surface of Si compared to the particles which penetrated beforehand.

In addition to this, the etching rate dependency on reaction temperature has been studied by researchers [75, 76] and it is well understood that with the increase of reaction temperature, the rate of formation of Si NWs also increases. It is also reported that an increase in the reaction temperature up to 60°C created nanopores within Si NWs which alter the optical, mechanical etc. properties [77, 78]. In this regard, a research work was carried out by C Y Chen et al. [79] where they attached a conductive substrate with the Si substrate and performed a two-step conventional MACE process. They investigated the role of back

substrates on NWs formation in the Si substrates irrespective of doping type and found that the back substrates prevent the excess hole injection to the Si substrate which was responsible to form nanoporous Si NWs [Fig.1.21]. They have suggested that oxidation of H_2O_2 occurs not only at the Ag/Si interface but also occurs on the surface of the back substrate which is in direct contact with the solution. Due to this an electron concentration gradient is produced in the neighbourhood of the back substrate. Hence, it drives the electrons towards the back of the Si substrate resulting in the reduction of pore formation during MACE process. Williams et al. [80] have studied the effect of etchant concentration by using gold and silver metal catalyst and suggested that the Ag morphology is not stable due to the dissolution and which led to forming rough structures on the back side of Si. On the other hand, they have reported that Au maintains its shape and dig into the wafer surface [Fig.1.22]

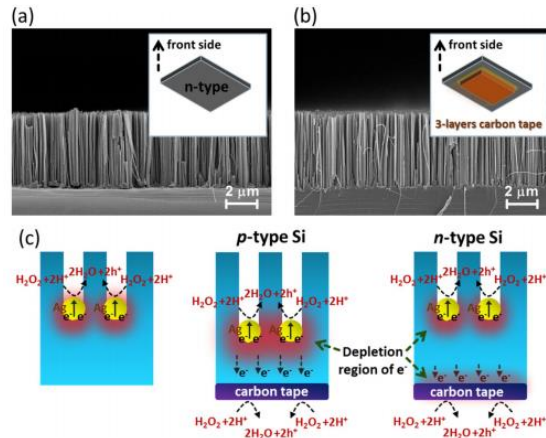


Fig.1.21: Cross-sectional SEM images of the arrays of aligned Si nanowire obtained from the catalytic etching of n-type Si: (a) by conventional MACE process and (b) back-substrate assisted MACE process where three-layer conductive carbon tape was used as back substrates. (c) Schematic representation of the distinct formation mechanisms of MACE process: Si substrates (p-type or n-type) devoid of conductive back substrates, Si substrates (p-type) and Si substrates (n-type) with the presence of conductive back substrates [79].

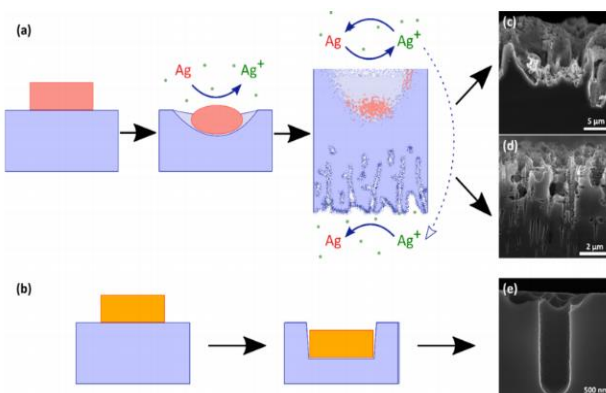


Fig.1.22: Scheme of the whole MACE process by using (a) silver and (b) gold metal catalysts. SEM images of (c) front side and (d) back side of a Si piece after 5 min of Ag-MACE in $\rho = 0.75$ and $\rho = 0.50$ baths, respectively. Part (e) shows the front side after 18 h of Au-MACE in a $\rho = 0.25$ bath [80].

1.4 Literature review on nano/microstructure-based SERS measurement of chemical species

Despite numerous efforts have given by many researchers to prepare the SERS substrate, the whole different types of SERS-active substrates can be categorised broadly into four groups which are mentioned below [81]:

1. Substrates with spherical gold (Au) or silver (Ag) nanoparticles (NPs), where these NPs were fabricated by sputtering or capillary force assembly, pulsed laser deposition etc.
2. Substrates with non-spherical nanostructures such as gold nanowire or another oxide (such as quasi-vertically aligned TiO₂) nanowires coated with Ag NPs.
3. Substrates with complex multiparticle nanostructures such as gold nanoflowers, gold nanodendrites etc.
4. A flexible substrate with decorated noble metal NPs, nanorods etc.

Baia et al. [82] have immobilized the colloidal gold NPs upon a glass substrate and SERS measurements were carried out in the visible and near-infrared spectral region by using p-aminothiophenol as the probe material. They have reported that a combination of surface plasmon excitation and high chemical affinity of gold with probe molecule made this SERS-active system as the suitable model for understanding Raman enhancement mechanism. Likewise, D. He et al. [83] have fabricated flexible and free-standing SERS substrate by electrospinning technique. A schematic of the whole process is shown in Fig.1.23.

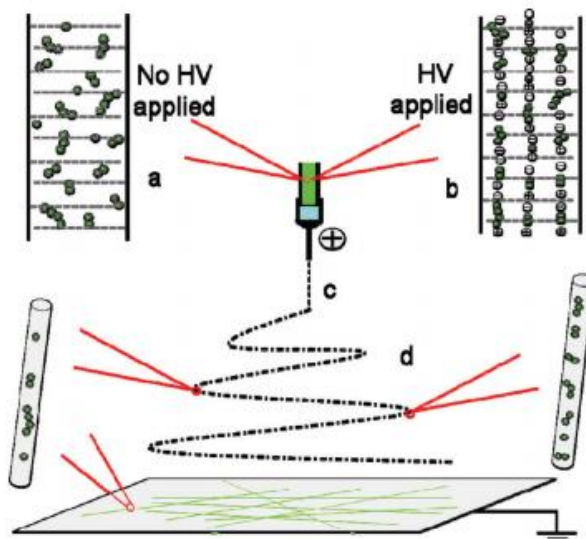


Fig.1.23: Illustration of the chain-like arrays formation of Ag NPs aggregates within PVA nanofibers. (a) Before the application of high voltage dispersion of Ag aggregates in PVA solution (b) with the application of high voltage to the blend solution, the whole solution was polarized and then one side of the PVA-capped Ag NP aggregates became positively charged and the other side became negatively charged. Due to the electrostatic attraction they would align themselves in the direction of the electric field. (c) Stable region near the tip of the spinneret. A jet would erupt from the tip of the spinneret when the repulsive force within the charged solution became larger than its surface tension. (d) Most nanofibers were formed in the instability region due to stretching and acceleration of the fluid filament as the solvent evaporated [83].

They have suggested that the electrospinning time and the amount of aggregation of the Ag NPs in poly(vinyl alcohol) (PVA) nanofibers are the two crucial points which basically determine the SERS signal enhancement. Similarly, in case of fabricating SERS substrate with non-spherical shaped nanostructures, L. Billot et al. [84] fabricated Au NWs on a glass substrate by using electron beam lithography (EBL) and lift-off technique. The dependence of Raman enhancement against the length of NWs have been verified and a maximum enhancement was reported for 670 and 900 nm long NWs. For the third variety of substrates, where complex nanostructures are used to enhance the Raman signal of the probe materials, Reinhard et al have reported multiscale enhancement by using nanoparticle cluster arrays (NCA). In their work, they have combined top-down nanofabrication and bottom-up self-assembly process to fabricate NCAs which help to more control the size of the particle clusters. It has been reported that the cluster size “ n ” and edge-to-edge separation between the clusters “ λ ” control the enhancement in the SERS signal. The fourth type substrates, i.e. flexible substrates have drawn lots of attention from the research community for wearable sensors.

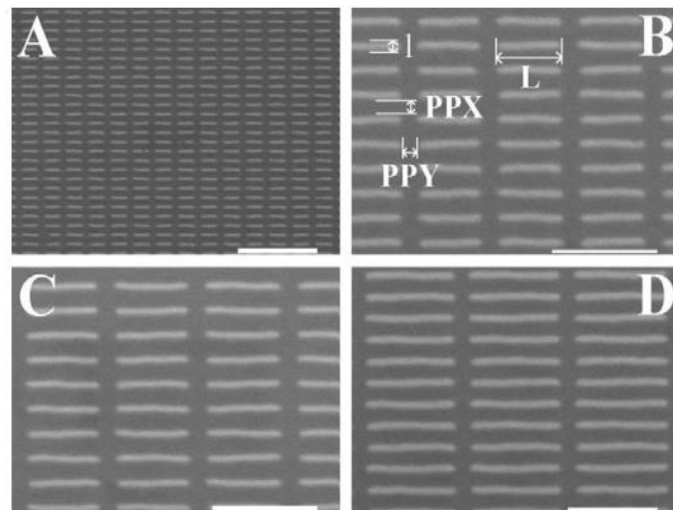


Fig.1.24: SEM images of the SERS-active substrates: array of gold nanowires with variable length, L (A: $L=420$ nm, B: $L=620$ nm, C: $L=720$ nm, D: $L=1\text{ }\mu\text{m}$), 50 nm height, 60 nm width (l). The inter-particle spacing are constant for all arrays and are fixed to 150 nm (PPX and PPY). Scale bars: 2 μm for A and 1 μm for B, C and D [84].

Incidentally, Chen-Chieh Yu et al [85] have produced highly sensitive SERS-active paper substrate where a photo-thermal effect, induced by laser was used to form NPs on it. The whole synthesis process of the SERS substrate preparation is shown in Fig.1.25. They have suggested that the density of the NPs directly influenced by the pore size of the paper substrate. According to their finding, the SERS signal could be enhanced by choosing the smaller the pore size that leads to higher the NPs density.

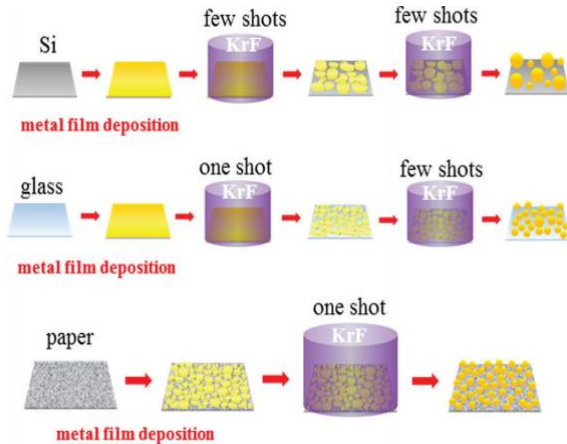


Fig.1.25: Graphical illustration of the fabrication of NPs on Si (flat, thermally conducting), glass (flat, thermally insulating), and paper (fibrils, thermally insulating) by taking advantage of the laser-induced photothermal effect. [85].

Si is considered one of the most used semiconducting material, therefore, the nanostructured-Si have lots of future potentials to use in the optoelectronic nanodevices. Therefore, despite different SERS substrates are being developed, recent research activities are focussing on the enhancement in the Raman signal by using Si substrates for different practical applications. Moreover, the well-established fabrication technology associated with this semiconducting material [86] has provided an extra advantage for using it for SERS applications. As a result, more research efforts are required to build SERS substrate those are compatible with the Si fabrication technology. In this regard, B. Zhang et al [87] have prepared SERS substrates with Ag-coated Si NWs by a wet-chemical process. Due to the poor diffusivity associated with the Ag NPs, they improved the Ag coating technique by incorporating an Au NPs electroless deposition.

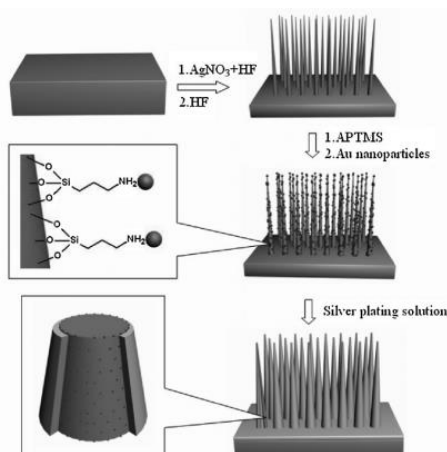


Fig.1.26: Illustration of the whole fabrication process of the silver-coated silicon nanowire arrays [87]

With this approach, they have reported that low concentration of the toxic molecules could be detected for human safety with a higher enhancement in the SERS signal. Similarly, L. Mikac

et al [88] have prepared porous Si by using electrochemical etching process where metal NPs were deposited by three different ways such as immersion plating, drop casting and pulsed laser ablation. The schematic of the whole SERS substrate fabrication process is shown in Fig.1.27. They were able to detect two different probe material such as Rhodamine 6G (R6G) up to 10^{-8} M and methylene blue (MB) up to 10^{-10} M with Ag ablated porous Si substrate.

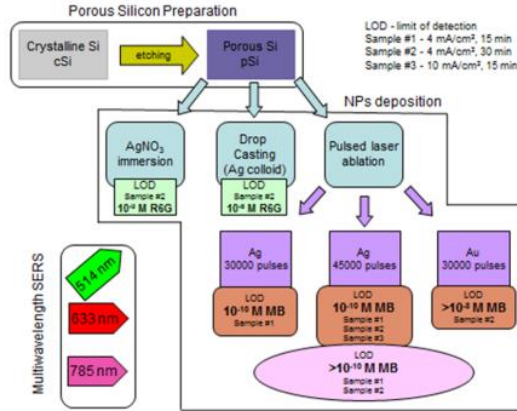


Fig.1.27: The scheme of the experiments [88]

In another reported work, S.A. Kara et al [3] had demonstrated few insights to the Si-based SERS substrate preparation where they have synthesized flexible Si NWs by combining two different processes such as Nano-Spheres Lithography (NSL) and MACE. With their SERS-active substrate, they were able to detect various probe molecule to picomolar concentration. Also, they have controlled the flexibility of the Si NWs by varying the aspect ratio of these NWs. Similarly, in case of 1:10 aspect ratio Si NWs, the microcapillary force drives the NWs close to each other whenever they were in contact with liquid and in the process trap the probe molecules at the fingertips coated with metal. This way the hot spots are generated which enhance the Raman signal.

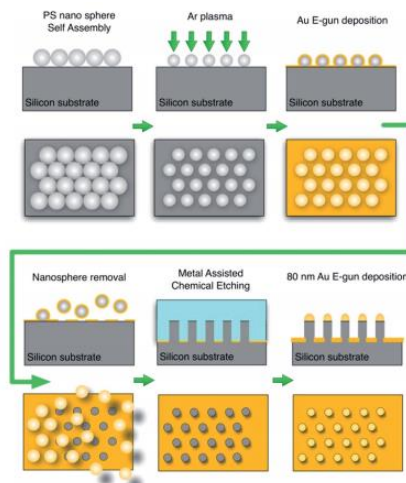


Fig.1.28: Details about the fabrication process of the silicon nanowire arrays coated with silver [3]

A similar Si-based SERS substrate fabrication has been reported by Bi-Shen Lee et al [89] where the silicon nanowire array (SiNWA) fabricated by MACE process and decorated with AuNPs by using oblique angle deposition (OAD) technique. They have used a gold metal backplate to enhance the intensity of the Raman signal and were able to reach an enhancement factor of 1.78×10^6 .

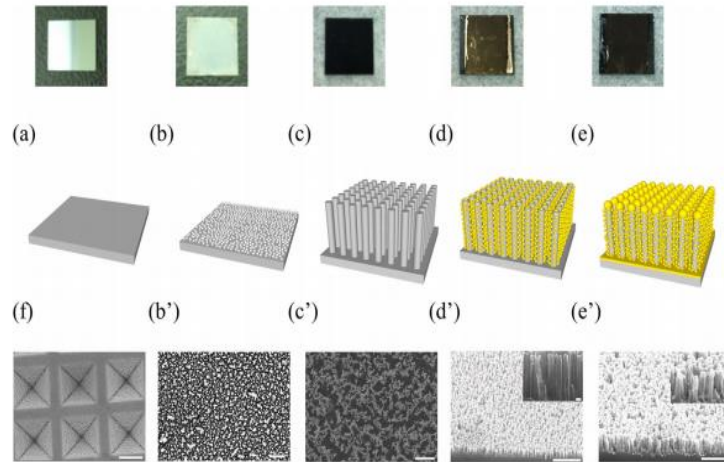


Fig.1.29: Schematic illustration of the experimental process flow (a) The cut <100> P-type 1 × 1 cm² Si substrate. (b) Si substrate with silver network used as the catalyst for the etching process. The blue region represents Ag clusters. (c) The SiNWA scaffold for the desired SERS substrate. (d) The SiNWA were decorated on the sidewall with AuNPs by OAD process. (e) The SiNWA with AuNPs and AuMBP as the preferred SERS substrate. (f) SEM image of commercialized SERS substrate (Klarite). It is noted that Figure (b'), (c'), (d'), (e') are the SEM images corresponded to each steps. (The scale bar represented 1 μm in the lower magnitude SEM image and represented 100 nm in the inset higher magnitude figure) [89].

They have reported that the use of Au metal backplate on the SERS substrate is possible to avoid the Raman signals being trapped by the SiNWs and hence the intensity of the signals can be enhanced. In this way, they were able to detect the malachite green probe molecule with the lowest concentration up to 10 nM. Recently Xuexian Chen et al. [90] have demonstrated that by incorporating superhydrophobic nature and functionalizing Au NPs in the hierarchical nanostructure of Si, the detection limit can be reached up to $\sim 10^{-11}$ M.

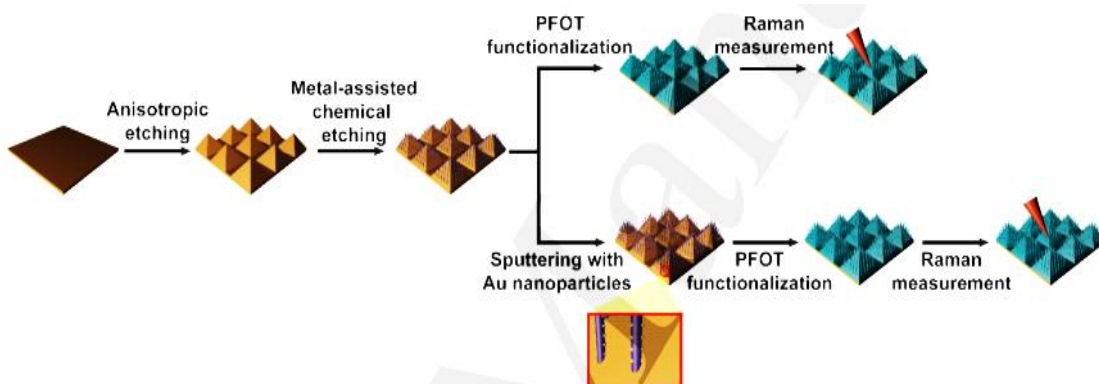


Fig.1.30: Schematic representation of the production of the superhydrophobic SERS substrate created with the hierarchical silicon nanostructures [90]

In their process, 1H,1H,2H,2H-perfluorooctyltriethoxysilane (PFOT) was used to make the substrate superhydrophobic and which enhanced the Raman signal as well. But using PFOT may create pulmonary diseases [91] and has other adverse effects.

Furthermore, K. P. Sooraj et al. [92] have fabricated a Si-based SERS substrate to detect Glucose level in blood by using Ag nanoparticle arrays. In their work, they have formed ripple patterns on Si by argon ion sputtering and then Ag NPs were deposited on it. It has been reported earlier that, without using binder molecule detection of Glucose by SERS technique is almost impossible due to its small Raman scattering cross-section and also due to very weak binding with the metal NPs. On the other hand, they have suggested that the issues associated with the binder-less Glucose detection can be overcome and it is possible to detect the biomolecule from the actual blood sample. The effect of plasmonic Ag NPs on ripple patterned Si substrate for the detection of Glucose from the actual blood sample is shown in Fig. 1.31. Their results indicate that without the NPs the same peaks were not detected for the same actual blood sample.

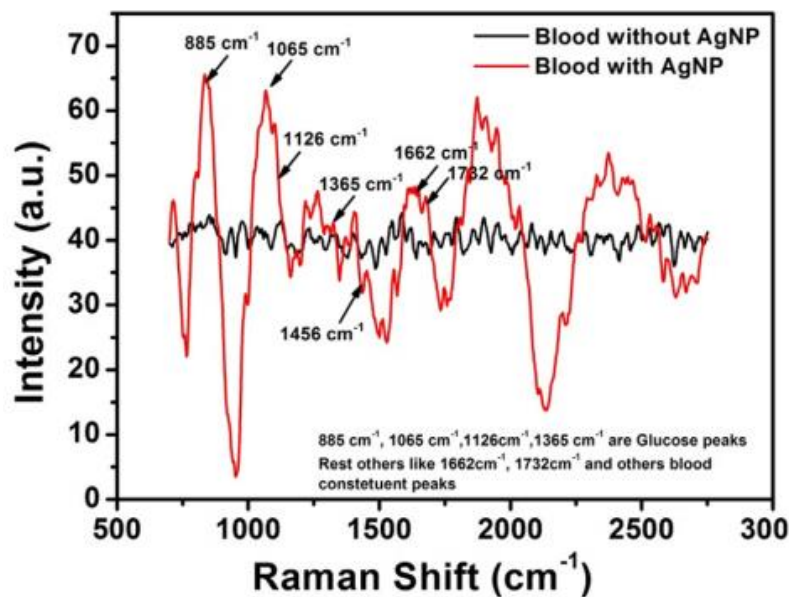


Fig.1.31: Collected Raman spectra of the real blood sample with and without the NPs. Correspondingly in the plot, Glucose peak and other blood peaks are shown [92].

Recently, SERS technique has emerged as a practical technique to be used in environmental pollution detection, and gained remarkable interest from the research community. For instance, L. A. Wali et al. [93] have reported the detection of the penicillin G (PG), which is normally used as the antibiotic drug for many diseases. The occurrence of this drug in the environment may create many problems for a human being and also to animals. In their work, they have targeted the detection of this antibiotic with porous Si-based SERS substrate where

they incorporated gold NPs and achieved the highest detection up to 10^{-9} M concentration of PG which is shown in Fig. 1.32.

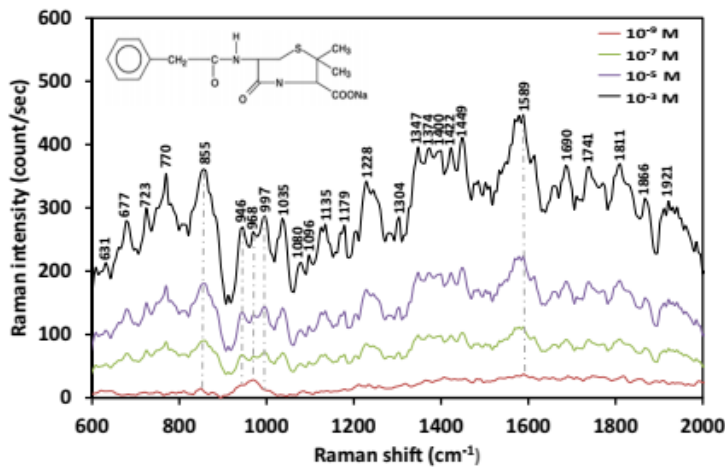


Fig.1.32: SERS spectra acquired by AuNPs/PSi SERS active substrate for the Penicillin G antibiotic at different concentrations [93].

1.5 Current challenges

From the current literature, it has been noticed that fabrication of different nano/microstructures on Si by MACE process still needs more efforts to improve this process for different applications. It has been found that, there are no available reported works on the annealing effect of a micro-stripe catalyst on the Si-etching process by MACE. Hence, it needs to be addressed. Moreover, the effect of metal micro stripes morphology on the Si-etching by MACE process is still not clear, and needs more research efforts to understand this phenomenon.

Moreover, from the current literature, it is reasonably clear that the fabrication of a proper SERS substrate is very much essential to use this analytical technique for practical application. In addition to that many efforts have been given towards the cost-effective way of fabrication and also the reusability of any SERS substrate starting from flexible to the Si-based substrate. It is also clear from the current literature that the micro/nanostructures fabricated on Si substrate play a vital role in achieving lower SERS detection limit of the analytes under probe. Therefore, still more challenges are there to enhance the SERS signal by fabricating desired nano/microstructures on Si substrate for the application of SERS detection, and thus effort must be given to control the parameters associated with the MACE process.

Despite huge efforts have been given towards understanding the effect of different parameters associated with the MACE process for the fabrication of desired nano/microstructures, few parameters such as the morphological effect of the catalyst, annealing effect of the metal catalyst are not addressed as per our knowledge and need to be investigated. It is well-established fact that the heat treatment can alter the physical properties and as well as can modify the morphology of the metal catalyst thin films. Hence it is required to understand the effect of thermal annealing of the metal catalyst on MACE of Si, and its effect on the chemical etching process. Furthermore, the deposition parameters associated with the metal catalyst deposition can also modify the morphology of these metal catalyst and can also modify the etching of Si by MACE process. To understand clearly these effects on the MACE process, more research work needs to be carried out to deposit different metal catalyst on Si substrates by varying few deposition parameters, for instance, the deposition of a metal catalyst with different morphologies. Eventually, a systematic study is required understand the effect of different morphological metal catalyst thin films on MACE of Si.

Another way to etch Si by using MACE process, where metal nanoparticles act as catalyst. It generally involves two different methods such as a one-step method and a two-step method. Most common way the researchers have used various in-situ metal nanoparticles deposition to etch Si, however, controlling the size and also the contamination involve in these processes are the shortfalls.

Out of many applications of Si micro/nanostructures fabricated by MACE process, the use of these substrates as SERS-active substrate have gained a lot of interest in recent years due to its potential in various fields such as detecting biomolecules to the explosive detection. In addition to this, the SERS technique has shown its potential to be widely used in the field of food safety and environmental pollution. Therefore, a systematic study needs to be carried out to fabricate different micro/nanostructures on Si by optimising different parameters associated with the MACE process and also to apply these substrates as SERS-active substrate for the detection of chemical species such as Methylene Blue (MB), Malachite Green (MG) etc. at a very lower concentration with higher Raman signal (higher enhancement factor).

However, the following are the limitation of the SERS technique

- (1) This method needs intimate contact between the surface and the analyte.
- (2) The possibility of degradation of the SERS substrate with the time which weakens the Raman signal.

- (3) Limited selectivity of the substrate for a particular analyte.
- (4) Re-usability of the SERS substrate.

Thus, it is required to address all these issues and for this purpose, the preparation of the SERS substrate plays a key role. The most common SERS substrates preparation process are classified as (i) metal nanoparticles, (ii) metal nanoparticles immobilised on the solid substrate and (iii) nano/microstructures fabricated directly on the solid substrates by micro/nanolithography and etching process. In this work, the effects of different nano/microstructure based Si, those are fabricated by MACE process and their influence on the detection of MB by SERS technique are addressed.

1.6 Objective of this thesis work

The main objective of this thesis work involves two areas such as (1) to investigate the effects of metal micro-stripes thickness and thermal annealing of these micro-stripes on the fabrication of the Si-microstructure by utilizing MACE process. In another approach, to apply directly the commercial metal NPs to etch Si by MACE process and compare with the existing method (2) The second objective of this thesis work is to apply these Si-nano/microstructures based substrates, those are prepared by MACE process as SERS substrates to detect the chemicals (MB) for food safety applications. Also, to investigate the influences of the different nano/microstructures/nanopores based Si as SERS substrates and their effects on the enhancement factor (Raman signal), and the detection limit for utilizing these SERS substrates for future chemical sensing applications.

CHAPTER 2

Microfabrication of metal micro-stripes on p-Si (100) substrate

2.1 Introduction

This chapter involves the deposition of a metal catalyst such as gold (Au) and Ag thin film and micro-fabrication of the metal micro stripes on silicon (Si) substrate, those metal micro-stripes act as a catalyst for the MACE process, which is discussed in the next chapter. Two different physical vapour deposition processes are employed to deposit Au metal catalyst thin film for the fabrication of Au micro stripes on Si substrate. For this purpose, the cleaned Si substrates are used directly for deposition of Au and Ag thin film. The whole process of thin film deposition and formation of micro stripes by the micro-fabrication process are explained in this chapter

2.2 Fabrication of Au/Ag micro stripes on p-Si (100) substrates

The fabrication process for Au/Ag micro stripes consists of four successive steps such as substrates cleaning, patterning of photoresist on the cleaned substrates, deposition of metal thin films on the patterned Si substrates and at last lift-off for the removal of the unwanted metal deposited on Si. The four steps are elaborated briefly in the following sections.

2.2.1 Cleaning of p-Si(100) substrates

Before the cleaning process, the p-Si (100) substrates with resistivity $1\text{-}10 \Omega\text{.cm}$ were cut in $1 \text{ cm} \times 1 \text{ cm}$ size by using a diamond scribe. Then the cleaning of these substrates was carried out in three different steps which are mentioned below. The whole cleaning process was done on a wet bench maintained inside a class 1000 clean room which is shown below.



Step 1: This step is named as RCA 1 cleaning step (where RCA stands for Radio Corporation of America) and basically used for the removal of organic impurities and dust particles. The RCA 1 is a mixture of deionized (DI) water (H_2O), hydrogen peroxide (H_2O_2) and ammonium hydroxide (NH_4OH) in a ratio 5:1:1 respectively. The cut pieces of Si were dipped in the RCA 1 for 10 minutes at 75^0 C and then rinsed with deionized (DI) water for several times.

Step 2: This is basically an optional step where a dilute solution of hydrofluoric acid (HF) is used. During the first step, normally a very thin oxide layer ($\sim 10 \text{ \AA}$) is formed on the surface of the Si substrates. To remove the oxide layer this cleaning step is used. But, in our process, this step was skipped so that the very thin oxide layer remain intact between Au and Si. This is necessary, as Si atoms diffuse rapidly to Au thin film even in room temperature and possibly form a gold silicide layer which may affect the Si etching process. Nevertheless, the presence of this oxide layer inhibits the formation of gold silicide [94].

Step 3: This step is termed as RCA 2 cleaning step and was used to remove all the metallic contaminants from the Si substrates. The RCA 2 is also a mixture of DI water, H_2O_2 and hydrochloric acid (HCl) in a ratio 6:1:1 respectively. In this step, the Si substrates were dipped in RCA 2 solution for 10 minutes at 75^0 C followed by rinsing in DI water for a number of times.

After completion of the abovementioned steps, the Si substrates were cleaned with DI water several times and dried by blowing nitrogen. Then, the Si substrates were used directly for further processes without any thermal treatment, to avoid any form of thermally induced stress [95].

2.2.2 Patterning of positive photoresist on the cleaned Si substrates

Once the cleaning process was over, all the cleaned substrates were coated with a positive photoresist and followed by a soft baking which was performed for 20 minutes. Subsequently, these substrates were exposed to UV light through a mask and then the exposed photoresist was developed with a developer. The stepwise schematic representation of the whole lithography process for pattern formation on Si substrate are mentioned below:

- Positive photoresist (+PR) OIR 620 was coated on the cleaned p-Si (100) substrates by a “Spin 150” spin coater with a two-step process.

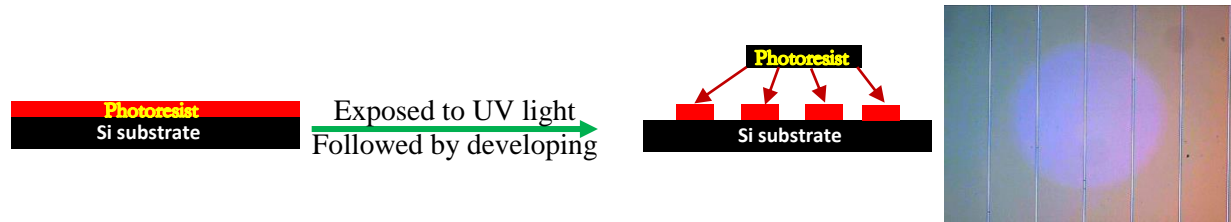
Step 1 - RPM = 500, time = 5 sec

Step 2 - RPM = 4500, time = 30 sec



After the coating process was completed, the +PR coated substrates were soft baked in a hot-plate at 85^0 C for 20 minutes. Then the photoresist films were exposed to ultraviolet light (364 nm) for 5 seconds. The exposed +PR coated substrates were patterned by using metal

lift-off process which was carried out by putting the PR coated Si substrates in acetone for 30 seconds.



2.2.3 Deposition and characterisation of thin films

In this section, the deposition of the thin films by various physical vapour deposition processes and its characterisations are discussed. In both the deposition, photoresist patterned Si substrates were used for the preparation of the metal micro-stripes on Si substrate.

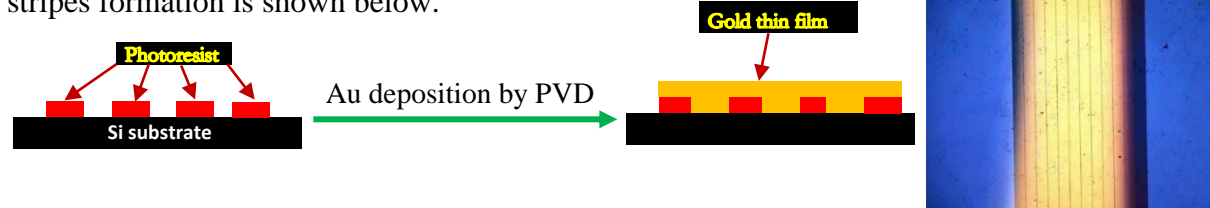
2.2.3.1 Deposition and characterisation of Au thin films by RF sputtering

The gold thin film was deposited on these PR patterned Si substrate by PVD by using the following synthesis parameters listed in Table 2.1. In this way, three different thickness 20, 50, 140 nm Au thin film were deposited on these substrates.

Table 2.1: Deposition parameters for Au thin film deposition by RF sputtering

Parameters	Values
Base pressure	7.49×10^{-7} mbar
Working pressure	7×10^{-3} mbar
Argon pressure	2.5 bar
RF power	40 W
Working temperature	35° C
Deposition rate	6 nm/min

The schematic representation of one of the fabrication step (thin film deposition) for micro-stripes formation is shown below.



All three depositions were carried out by maintaining identical parameter except the deposition time to obtain three different thickness on the PR- patterned Si- substrates. The first deposition was carried out for 4 minutes, whereas the second and third depositions were carried out for 8 and 23 minutes. This way all three thin films of different thicknesses were successfully deposited on the photoresist patterned Si substrates. After the deposition, the

deposited thin films were characterised by X-ray diffraction (XRD) and energy dispersive X-ray analysis (EDX). For XRD analysis, a dummy substrate was prepared by keeping a clean and bare p-Si (100) substrate inside the deposition chamber along with the test substrates which were coated with photoresist pattern. Then the dummy substrates for three different depositions were used to collect the XRD pattern for Au coated on a Si substrate. The XRD plot of the first deposition which was carried out for 4 minutes is shown in Fig.2.1 (a).

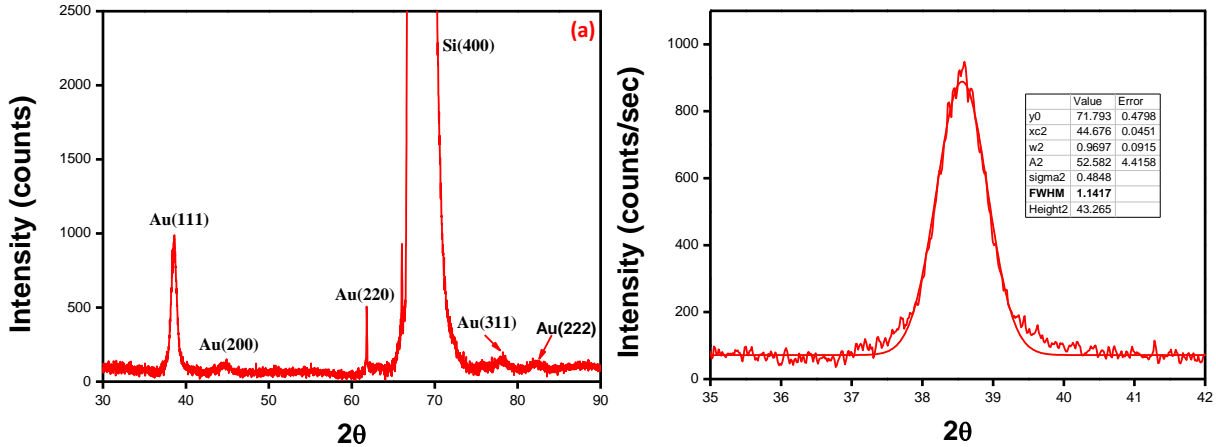


Fig.2.1: (a) XRD pattern of Au thin film deposited on Si substrate for 4 minutes, (b) FWHM of the Au (111) peak by Gaussian fitting in Origin)

As shown in Fig. 2.1 (a), five peaks ($2\theta = 38.51, 44.63, 62.1, 77.87$ and 82.07°) appear and are indexed to the face centred cubic (FCC) structure of gold with a lattice constant 4.04 \AA , having (hkl) values of (111), (200), (220), (311), and (222) respectively (verified with Downs et al. [94]). Similarly, the peak appears at $2\theta = 69.27^\circ$ is indexed to the Si with (hkl) value of (400) (verified with JCPDS card 27–1402). Out of all the five peaks indexed for Au, the highest intensity peak, i.e. (111) is considered to calculate the crystallite size of Au by using the Scherrer's formula [97].

$$D_p = \frac{0.9\lambda}{\beta_p \cos\theta} \quad (2.1)$$

Here β_p is the full width at half the maximum (FWHM) intensity, λ is the X-ray wavelength, and θ is the Bragg angle. For FWHM of the highest intensity peak, Gaussian fitting was done by using Origin software and is shown in Fig.2.1 (b). By using the abovementioned formula 2.1, the crystallite size of the Au is calculated as $\sim 7.5 \text{ nm}$.

The XRD pattern of the second sample (8 min, Au deposition) is shown in Fig.2.2 (a). As shown in Fig. 2.2 (a), the five peaks ($2\theta = 38.79, 45.01, 63.1, 77.35$ and 83.03°) appear and are indexed to the face centred cubic (FCC) structure of gold with a lattice constant 4.01 \AA . The corresponding planes are (111), (200), (220), (311), and (222), respectively (verified

with Downs et al.). Similarly, the peak appears at $2\theta = 69.27^\circ$ is indexed to the Si with (hkl) value of (400) (verified with JCPDS card 27–1402). Out of all five peaks indexed for Au, the highest intensity peak, i.e. (111) is considered to calculate the crystallite size of Au by using the Scherrer's formula. Gaussian fitting was done by using Origin software to evaluate the FWHM and is shown in Fig.2.2 (b).

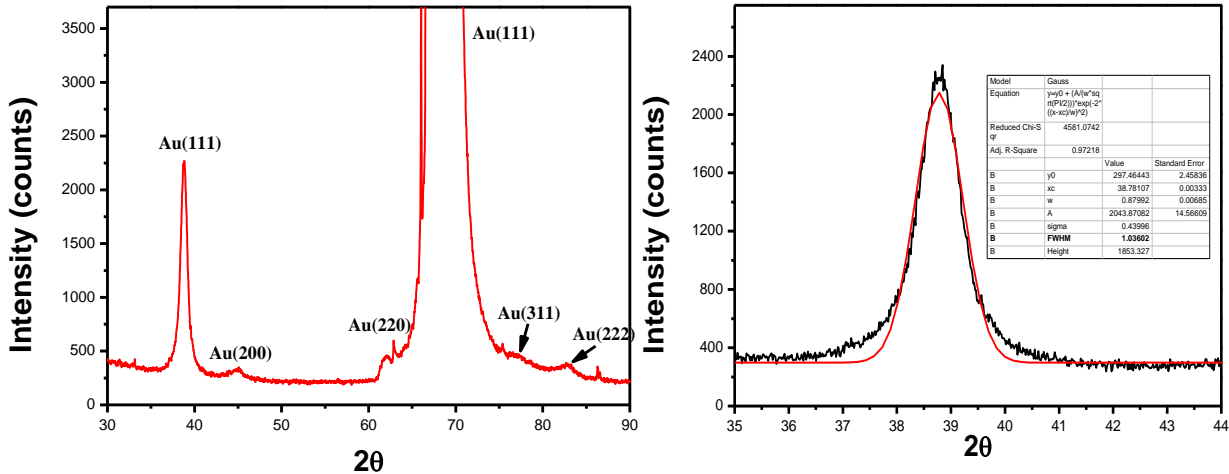


Fig.2.2: (a) XRD pattern of Au thin film deposited on Si substrate for 8 minutes, (b) FWHM of the Au (111) peak by Gaussian fitting in Origin

By using the formula 2.1, the crystallite size of the Au is calculated as ~ 8.3 nm. The XRD pattern for the third sample Au thin film which was carried out for 23 minutes is shown in Fig.2.3 (a).

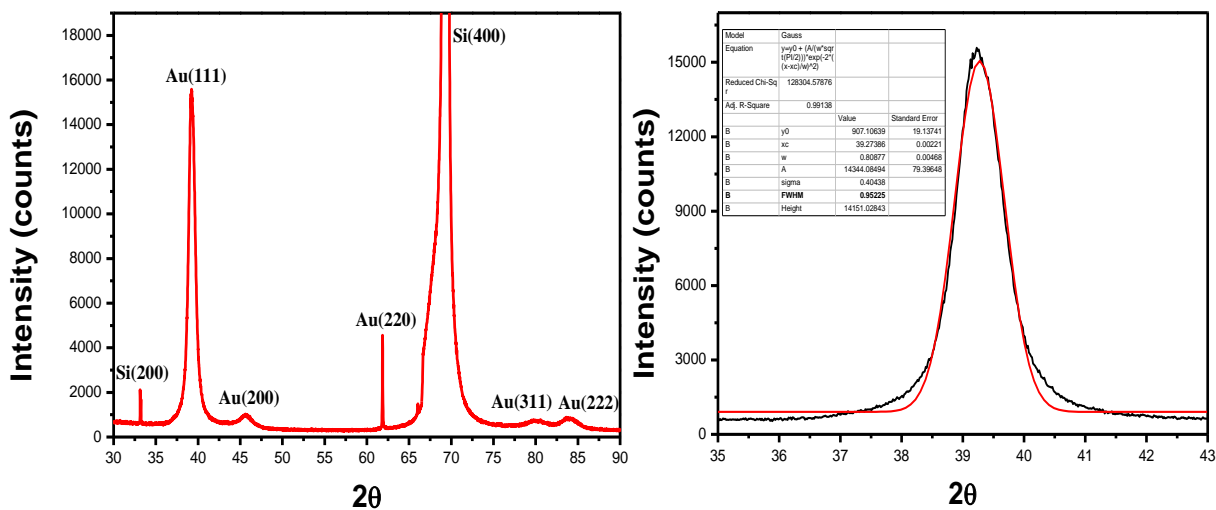


Fig.2.3: (a) XRD pattern of Au thin film deposited on Si substrate for 23 minutes, (b) FWHM of the Au (111) peak by Gaussian fitting in Origin

Fig. 2.3. (a) shows the XRD pattern and five peaks ($2\theta = 39.2, 45.6, 62.2, 79.7$ and 83.5) appear those are indexed to the face centred cubic (FCC) structure of gold with a lattice

constant 3.96 \AA . All five peaks are indexed to the corresponding planes (111), (200), (220), (311), (222), respectively (verified with Downs et al). Similarly, two peaks at $2\theta = 33.14^\circ$ and 69.27° are indexed to (200) and (400) planes respectively, (verified with JCPDS card 27–1402) respectively. Out of all five peaks, the highest intensity peak, i.e. (111) is considered to calculate the crystallite size of Au by using the Scherrer formula as mentioned earlier. To find the FWHM of the peak (111), Gaussian fitting was carried out for the peak in Origin which is shown in Fig.2.3 (b). By using the Scherrer formula (2.1), the crystallite size of Au thin film is evaluated as 9.1 nm. It is confirmed by the experimental results that the crystallite size increases with the film thickness. From the XRD analysis for both the depositions, it is found that there is no extra peaks are present which indicates the purity of the Au thin film without any contamination. Moreover, it is also found in both the deposition, no silicate formation is observed after the Au deposition on Si substrate which is due to the presence of a very thin oxide layer on the Si substrate. It is already reported earlier that at room temperature and also in an unbaked unpassivated and unetched Si substrate, the silicide formation does not occur [94]. The elemental identification and the quantitative compositional information of the thin films were carried out by EDX analysis. The EDX spectra and quantitative compositions for the first deposited Au thin film are shown in Fig.2.4.

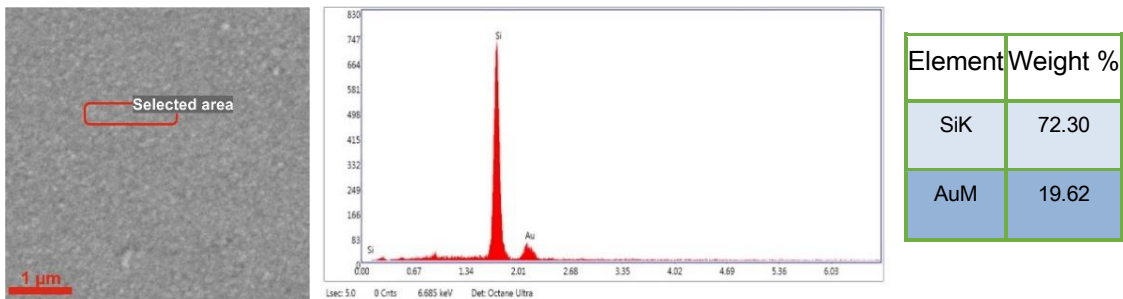


Fig.2.4: EDX spectra of the first deposited Au thin film on Si

The EDX spectra and quantitative compositions for the second deposited Au thin film are shown in Fig.2.5.

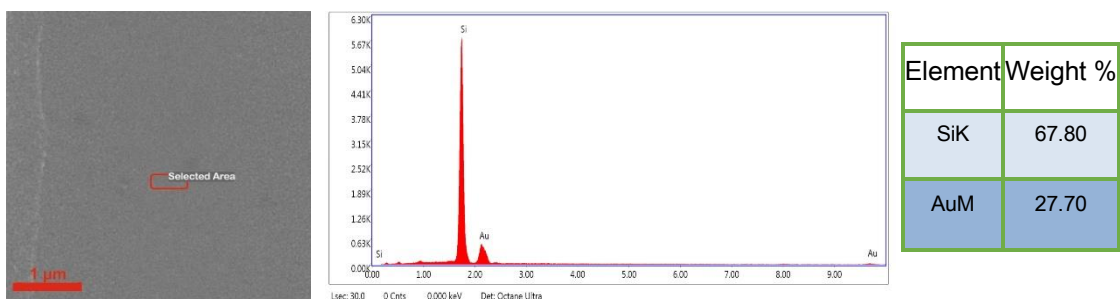


Fig.2.5: EDX spectra of the second deposited Au thin film on Si

Similarly, for the third Au thin film deposition, the EDX spectra and quantitative compositions are shown in Fig.2.6.

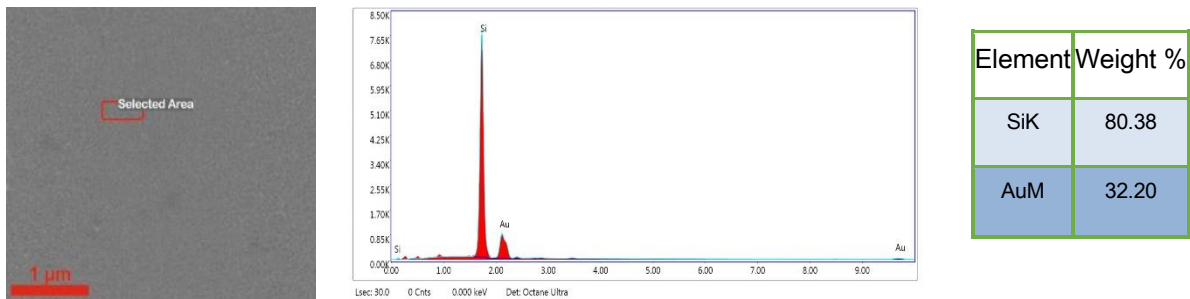


Fig.2.6: EDX spectra of the third deposited Au thin film on Si substrate

There is no extra element present in the sample which is verified by the EDX analysis. Thus, the results indicate that the deposited Au thin film on the Si substrates was almost 100% pure. Moreover, the percentage of Au present in the thin film was found higher in case of longer deposition time compared to the shorter deposition time, this is due to the higher thickness of the Au thin film.

2.2.3.2 Deposition and characterisation of Au and Ag thin films by Thermal Evaporation

In our research, two different PVD systems were used for Au deposition such as RF sputtering and thermal evaporation. In the previous section, all the details about RF sputtering and the characterisation of these sputtered thin films was discussed. In this section, the details about the Au and Ag thin film deposition by thermal evaporation and the characterisation of these thin films will be discussed. The deposition of Au and Ag were carried out by using a thermal evaporation system manufactured by “Vec Solutions” which is shown below. The parameters related to the thermal evaporation for both Au and Ag are mentioned in the following table (Table 2.2). Moreover, in both cases, wire type source was used to deposit thin films of Au and Ag.

Table 2.2: Deposition parameters for Au and Ag thin films deposition by thermal evaporation

Parameters	Values
Base pressure	1×10^{-6} mbar
Source to substrate distance	10 cm
Substrate rotation	3 rpm
Deposition current	140A
Deposition time	2 min



All the Au/Ag, the as-deposited thin films were characterised by X-ray diffraction (XRD) and energy dispersive X-ray analysis (EDX) for structure and compositional analysis. Similar to the previous deposition, for XRD measurement, a dummy substrate was prepared by keeping a clean and bare p-Si (100) substrate inside the deposition chamber along with the test substrates which were coated with photoresist pattern. Afterwards, the dummy substrates for two different depositions were used to collect the XRD pattern for Au and Ag-coated on Si substrates. The XRD pattern of the Au deposition which was carried out for 2 minutes is shown in Fig.2.7 (a).

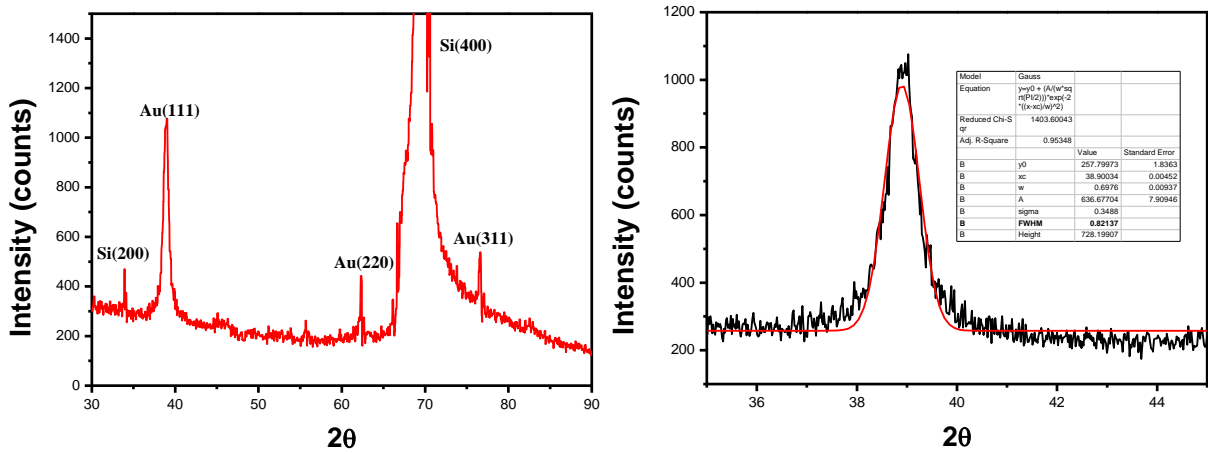


Fig.2.7: (a) XRD pattern of Au thin film deposited on Si substrate by thermal evaporation, (b) FWHM of the Ag (111) peak by Gaussian fitting in Origin

From the XRD plot, the three peaks ($2\theta = 38.95^\circ$, 62.65° , and 77.08°) are indexed to the face centred cubic (FCC) structure of gold with a lattice constant of 3.98 \AA . All three peaks are indexed with the (hkl) values of (111), (220), and (311) respectively (verified with Downs et al.). Similarly, two peaks at $2\theta = 33.8^\circ$ and 69.27° are indexed to the Si having (hkl) value of (200) and (400) (verified with JCPDS card 27–1402) respectively. Out of all three peaks indexed for Au, the highest intensity peak, i.e. (111) is considered to calculate the crystallite size of Au by using the Scherrer formula as mentioned earlier. To find the FWHM of the peak (111), Gaussian fitting was done for the peak in Origin which is shown in Fig. 2.7 (b). As the FWHM is calculated by performing a Gaussian fitting in Origin, the crystallite size of the deposited Au thin film is calculated by using the Scherrer formula and it is found to be $\sim 10.6 \text{ nm}$.

The XRD plot of the Ag deposition which was carried out for 2 minutes is shown in Fig.2.8 (a). From XRD pattern, the five peaks appears at ($2\theta = 38.4^\circ$, 43.4° , 61.9° , 77.9° and 82.1°) to the face centred cubic (FCC) structure of silver with a lattice constant 2.35 \AA , having (hkl) values of (111), (200), (220), (311), (222) respectively (verified with Downs et al. [96]).

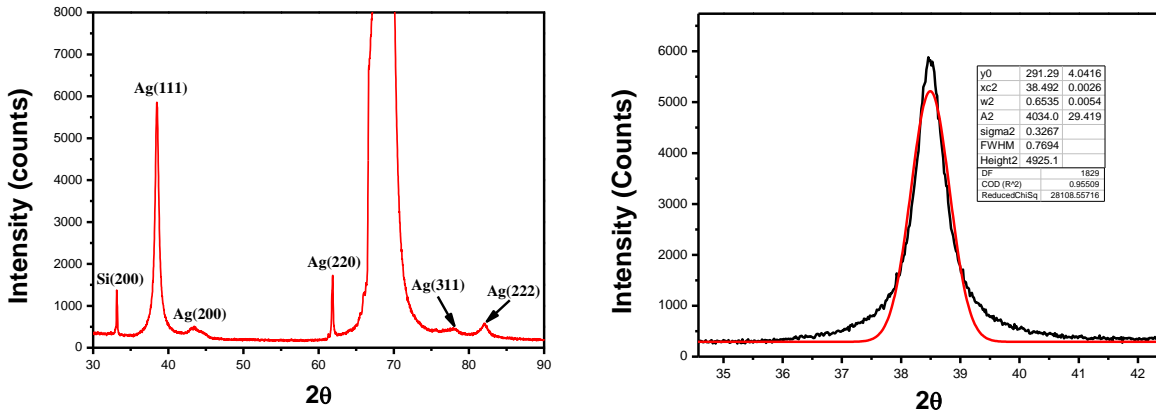


Fig.2.8: (a) XRD pattern of Ag thin film deposited on Si substrate by thermal evaporation, (b) FWHM of the Ag (111) peak by Gaussian fitting in Origin

Similarly, two peaks at $2\theta = 33.16^0$ and 69.29^0 are indexed to the Si having (hkl) value of (200) [98] and (400) (verified with JCPDS card 27–1402) respectively. Out of all five peaks indexed for Ag, the dominant out-of-plan peak, i.e. (111) is considered to calculate the crystallite size of Ag by using the Scherrer formula as mentioned earlier. In this regard, for (111) peak FWHM is calculated by using Origin software where the peak is fitted with Gaussian and is shown in Fig.2.8 (b). By using the FWHM value in the Scherrer formula, the crystallite size of the Ag is calculated as ~ 10.34 nm.

The elemental identification and the quantitative compositional information of the Au and Ag thin films were carried out by EDX analysis. The EDX spectra and quantitative compositions for the Au thin film are shown in Fig. 2.9.

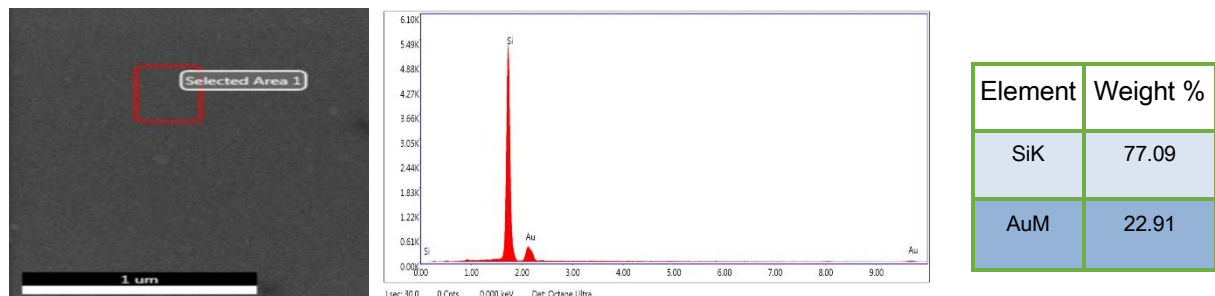


Fig.2.9: EDX spectra of the thermally evaporated Au thin film on Si

Similarly, for the Ag thin film deposition, the EDX spectra and quantitative compositions are shown in Fig.2.10.

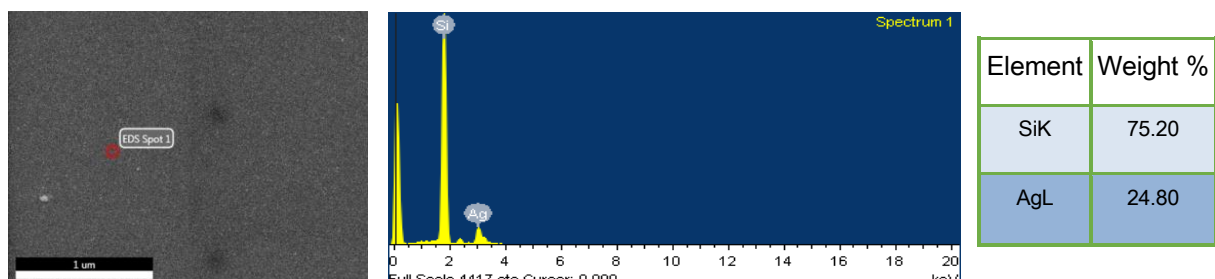


Fig.2.10: EDX spectra of the thermally evaporated Ag thin film on Si

From both XRD and EDX analysis it is confirmed that the deposited thin films of Au and Ag have no other contaminants or other foreign elements. The results indicate that the thin films deposited by thermal evaporation are pure without any contamination or element.

2.2.3.3 Deposition and characterisation of Au thin film deposited with the different source to target distance

Au thin films were deposited by thermal evaporation where the distance between source and substrate was varied to achieve thin films with different surface morphologies. In this regard, three depositions were carried out where every parameter related to thermal evaporation were kept constant except the distance between the source and substrate. Moreover, in this study, one more step was included in the cleaning process of the Si substrate in order to remove the native oxide layer. Thus, after the RCA 1 cleaning (**Step 1**) HF cleaning was performed (**Step 2**) to etch the native oxide layer which normally grows on the surface of Si. The deposition was carried out on all these substrates with the following parameters as illustrates in Table 2.3.

Table 2.3: Deposition parameters for Au thin film deposition by thermal evaporation

Parameters	Values
Base pressure	1×10^{-6} mbar
Source to substrate distance	10, 12 and 15 cm
Substrate rotation	3 rpm
Deposition current	140 A
Deposition time	2, 2 and 4 min

After the deposition, the thin films were characterised with XRD and EDX. Similar to the earlier characteristics, here also for XRD analysis, a dummy substrate was prepared by keeping a clean and bare p-Si (100) substrate inside the deposition chamber along with the test substrate. Afterwards, the dummy substrates for three different depositions were used to collect the XRD pattern for Au deposited on Si substrates. The XRD pattern of the Au thin film on the Si, which was carried out by maintaining 10 cm separation between the source and the substrate is shown in Fig.2.11 (a). From XRD plot, the three peaks appear at ($2\theta = 39.05, 62.0$ and 76.66) are indexed to the face centred cubic (FCC) structure of gold with a lattice constant 3.98 \AA . The (hkl) values are (111), (220), (311) respectively (verified with Downs et al.) [96]. Similarly, two peaks appear at $2\theta = 33.92^\circ$ and 69.67° are indexed to the Si having (hkl) value of (200) and (400) (verified with JCPDS card 27–1402) respectively. Out of all three peaks indexed for Au, the highest intensity peak, i.e. (111) was considered to calculate the crystallite size of Au by using the Scherrer formula as mentioned earlier. The

FWHM was evaluated by performing fitting in origin which is shown in Fig. 2.11 (b). By using the Scherrer's formula (2.1), the crystallite size of the Au is calculated as ~ 10.7 nm.

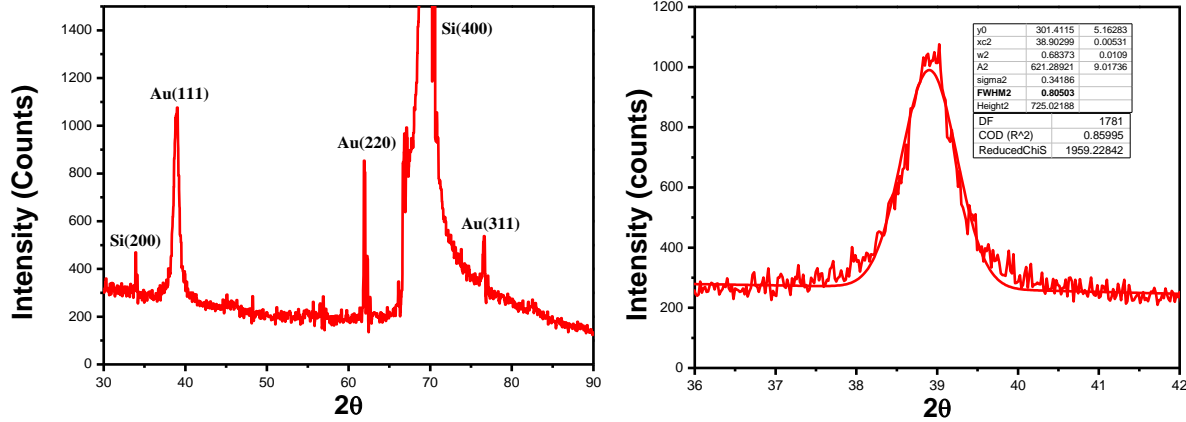


Fig.2.11: (a) XRD pattern of Au thin film deposited on Si substrate by maintaining 10 cm gap between source and substrate, (b) FWHM of the Au (111) peak by Gaussian fitting in Origin

Similarly for another deposition of Au thin film, the distance between the source and substrate was fixed at 12 cm, the corresponding XRD pattern of Au thin film is shown in Fig.2.12 (a).

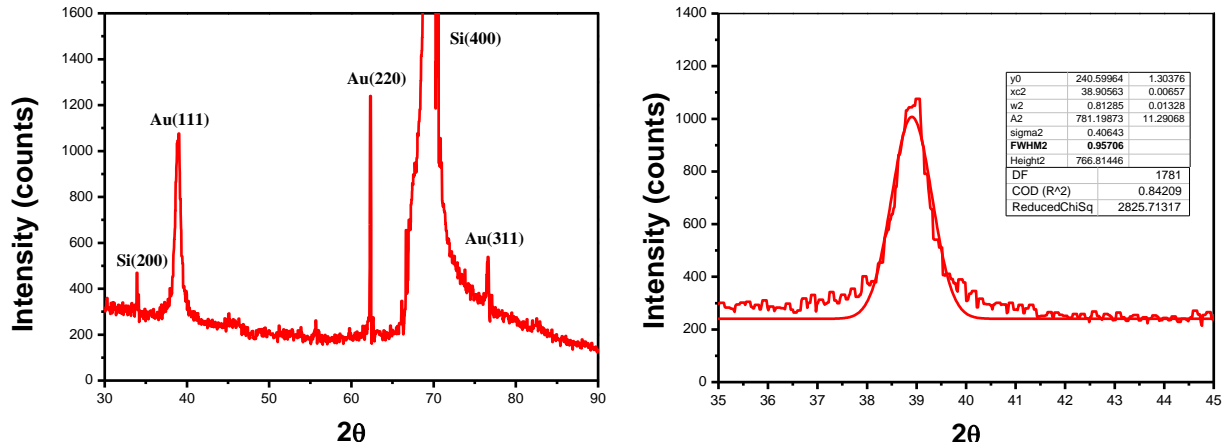


Fig.2.12: (a) XRD pattern of Au thin film deposited on Si substrate by maintaining 12 cm gap between source and substrate, (b) FWHM of the Au (111) peak by Gaussian fitting in Origin.

As shown in Fig. 2.12 (a), three peaks appear at $2\theta = 39.04$, 62.26 and 76.67 and are indexed to the face centred cubic (FCC) structure of gold with a lattice constant of 3.99 Å. The corresponding planes are (111), (220), (311), respectively (verified with Downs et al. [96]). Similarly, two peaks at $2\theta = 33.92^\circ$ and 69.67° are indexed to the Si (200) and (400) planes (verified with JCPDS card 27–1402) respectively. Out of the three peaks, indexed for the Au, the (111) peak was considered for crystallite size measurement by Scherrer's formula. The FWHM of this very peak was measured by fitting the peak in origin which is shown in Fig.2.12 (b). From the Scherrer's formula (2.1), the crystallite size was calculated as ~ 9 nm.

The third Au thin film deposition carried out for the 15 cm source to substrate distance and the corresponding XRD pattern of this sample is shown in Fig.2.13.

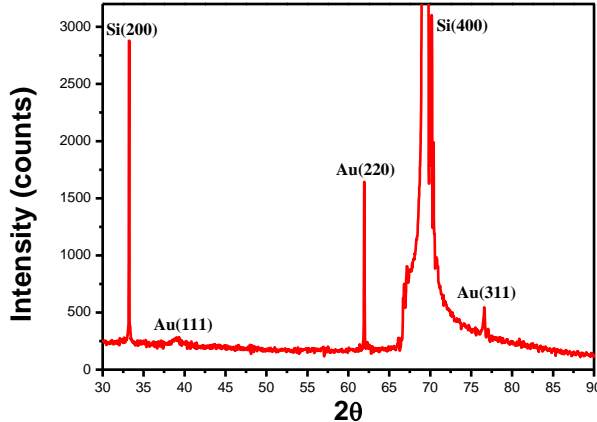


Fig.2.13: XRD pattern of Au thin film deposited on Si substrate by maintaining 15 cm gap between source and substrate

As shown in Fig. 2.13, three peaks appear at $2\theta = 39.10$, 62.06 and 76.66 those are indexed with FCC structure of Au with a lattice constant of 3.99 \AA . These are corresponding to the (111), (220) and (311) planes of Au respectively (verified with Downs et al. [96]). Surprisingly a different result is observed from the XRD analysis as shown in Fig. 2.13. In this case, the Au thin film did not grow in the preferred growth direction i.e. (111), rather an improve intensities for Au(220) and Si(200) peaks are observed. This result indicates the possible diffusion of the Si atoms to Au thin film. It is already reported earlier that in absence of oxide layer, Si atoms diffuse rapidly to the evaporated Au thin film even at room temperature. Due to the diffusion, these Si atoms form a gold silicide layer on both sides of the Au thin film [94]. But at room temperature, these silicide layers show amorphous nature or lacking of the long-range order, hence it may be difficult to detect from XRD [94]. But few changes can be observed such as decrease of the intensity of the (111) peak which is considered as the preferred growth direction for Au thin film deposition and also a noticeable increment in the intensity of the (200) peak which resembles the changes in the crystal structure of deposited Au thin film. Due to these reasons, the Au thin film which was deposited by keeping the distance between source and substrate as 15 cm did not use further for any study. The elemental identification and the quantitative compositional information of the Au thin films (deposited by keeping different distance between source and substrate) were carried out by EDX analysis. The EDX spectra and quantitative compositions for the Au thin films are shown in Fig. 2.14 and 2.15. On the other hand, in the case of Au thin film deposited by keeping 12 cm distance between source and substrate, a different morphology is

observed which will be discussed thoroughly in chapter 3. Due to the complex morphology, EDX analysis was carried out in two different place of the thin film such as one at flat region and other at hillock region which is shown in Fig.2.15

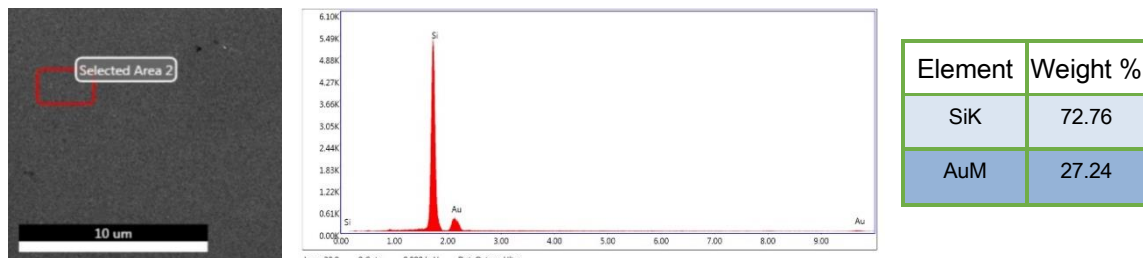


Fig.2.14: EDX spectra of the thermally evaporated Au thin film on Si substrate by maintaining 10 cm gap between source and substrate

It is clearly seen from the EDX analysis that in both the region such as hillock region and flat region consists of pure gold. The possible reason of such morphology is explained in chapter 3. The next step is to proceed to the lift-off process and which in turn remove the unwanted metals from the portions of Si substrate. The whole process of lift-off is mentioned in the next section.

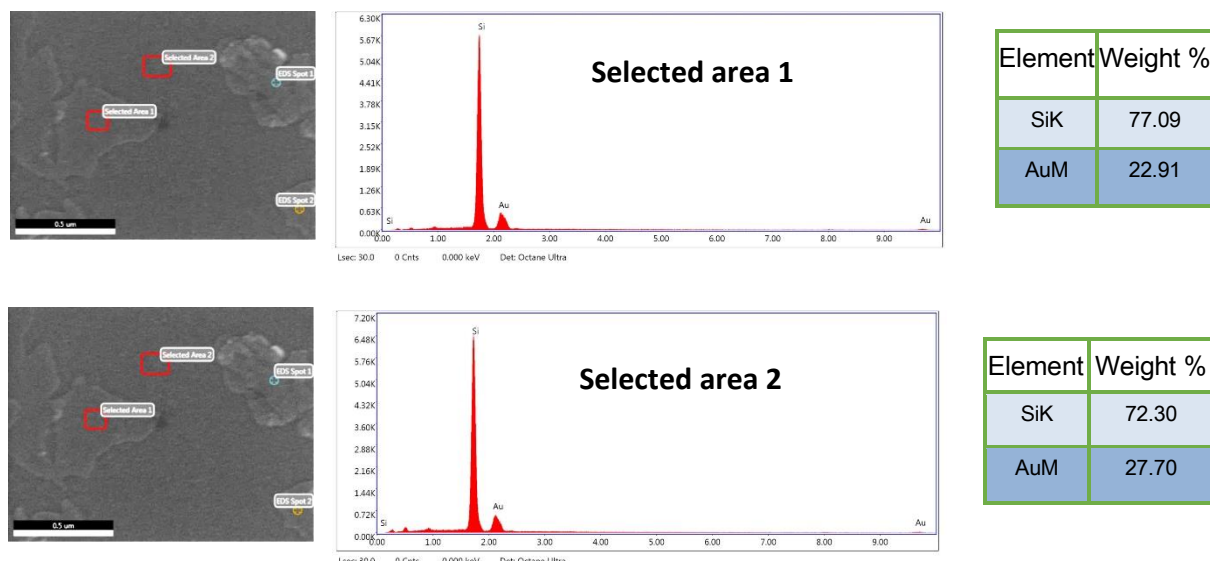
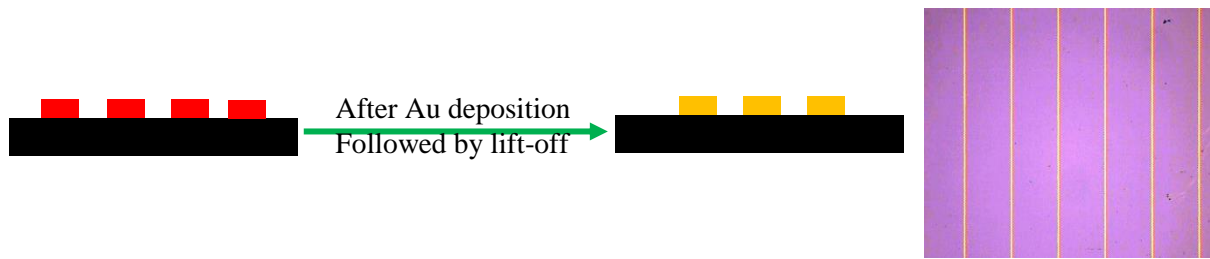


Fig.2.15: EDX spectra of the thermally evaporated Au thin film on Si substrate by maintaining 12 cm gap between source and substrate

2.2.4 Lift-off process for the patterning of gold/silver thin film on Si

The lift-off process was carried out to pattern Au/Ag micro-stripes on the Si substrate. This process was executed by dipping the Au and Ag-coated substrates in acetone along with the sonication for 30 seconds. Then the substrates were cleaned in DI water for three times and subsequently dried with the nitrogen blow.



The fabricated micro-stripes are characterised under FESEM which is shown in Fig.2.16 and it is confirmed that the shape and size of these stripes are uniform.

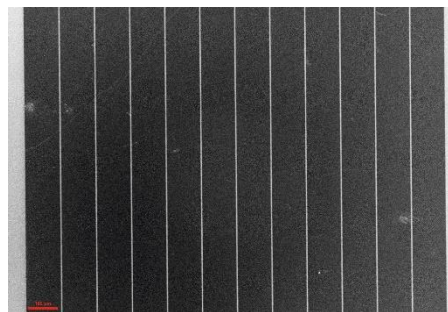


Fig.2.16: FESEM image of the Micro-stripes fabricated on Si

Moreover, the width of the micro-stripes was measured by both optical microscope and FESEM which are shown in Fig.2.17. It is clearly seen that the thickness of the micro-stripes is about of $3.24 \mu\text{m}$.

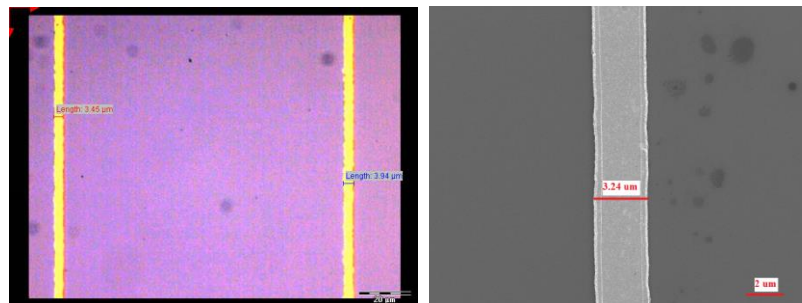
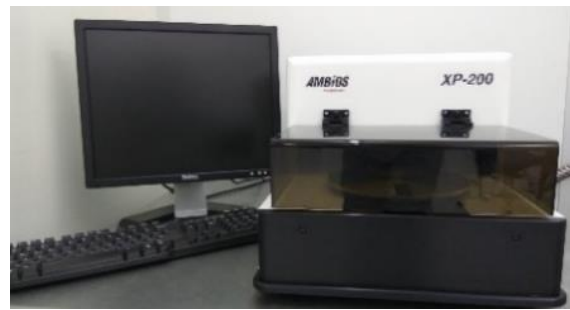


Fig.2.17: Width of the Au catalyst (a) optical microscope image, (b) FESEM

Once the lift-off process was over, the thickness of these micro-stripes of Au and Ag were measured by profilometer and discussed in the next session.

2.3 Characterisation of the metal micro-stripes fabricated on Si substrate

Both the Au and Ag micro-stripes were fabricated on Si substrates and the whole micro-fabrication process is already discussed in earlier sections. Before applying these micro-stripes for further chemical etching of Si, the thickness of these fabricated micro-stripes was measured by using an “Ambios XP-200” surface profilometer system.



Similarly, The thickness of the fabricated micro-stripes on Si substrate which were created from the thin films deposited by RF sputtering incorporating a lithography process are measured with a surface profilometer and is shown in Fig.2.18.

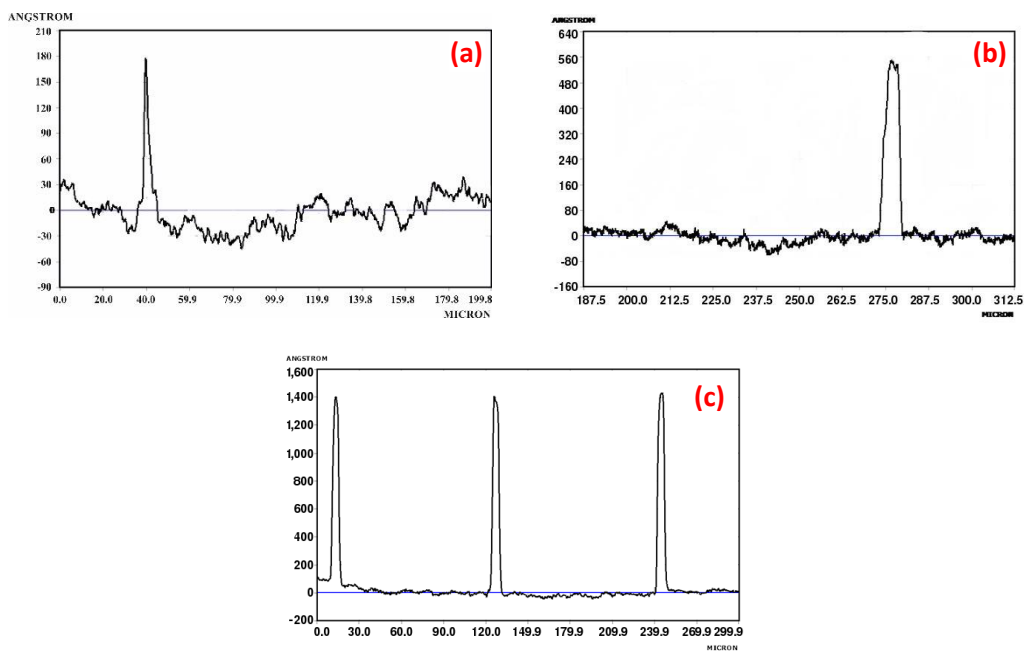


Fig.2.18: Surface profilometer plots of (a) ~ 20 nm (b) ~ 50 nm and (c) ~ 140 nm thin patterned Au micro-stripes on Si substrate

It is found from the measurements that three different thicknesses of the micro-stripes were fabricated, and these results indicate that there is a direct correlation of time with thickness. The 140 nm thick micro-stripes were formed for 23 minutes deposition, 50 nm thick micro-stripes were formed for 8 minutes deposition time and 20nm thickness was obtained for 4 minutes. Another batch of Au and Ag micro-stripes were fabricated on Si substrate by incorporating lithography and thin film deposition by thermal evaporation process which are already mentioned in the previous sections. After the fabrication, the thicknesses of these micro-stripes were measured with surface profilometer which is shown in Fig.2.19.

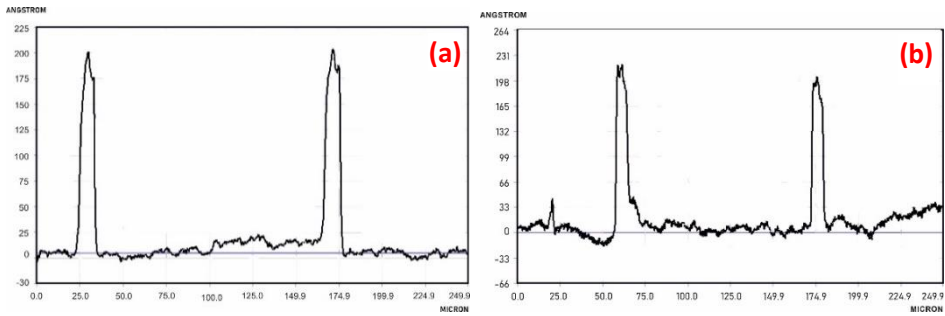


Fig.2.19: Surface profilometer plots of (a) Au (b) Ag micro stripes on the Si

From the surface profilometer measurement, the thickness of the Au and Ag micro-stripes are found to be about 20 nm. In another deposition, the thickness of fabricated Au micro-stripes was measured with the same surface profilometer. In detail, these micro-stripes were fabricated from the thin films deposited by varying the distance between source and substrate.

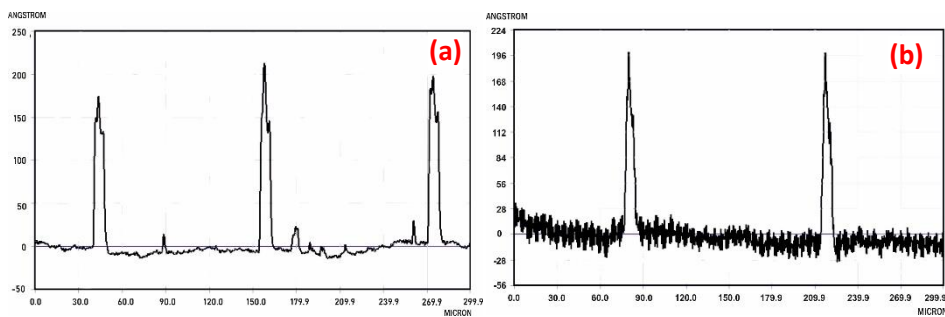


Fig.2.20: Surface profilometer plots of micro-stripes fabricated on Si substrate from Au thin film (a) by maintaining 10 cm gap between source and substrate and (b) by maintaining 12 cm gap between source and substrate

These different micro-stripes fabricated on Si substrate consist of similar thickness which is about ~ 20 nm. Thus, a set of three Au and Ag micro-stripes on the Si were fabricated with different thicknesses for MACE process, which will be discussed in the next chapter.

2.4 Conclusions

The Au and Ag micro-stripes were successfully fabricated on Si substrates by incorporating lithography and thin film deposition followed by a lift-off process. Au and Ag thin films were successfully deposited by two different ways such as RF sputtering and thermal evaporation with utmost purity. Subsequently, the thickness measurement by surface profilometer revealed that the micro-stripes fabricated from the RF sputtered thin films had two different thicknesses related to various deposition times and which were confirmed as 50 nm and 140 nm. Similarly, Au and Ag micro-stripes which were fabricated from the thin film deposited by thermal evaporation consists of the same thickness of 20 nm. In addition to few more depositions were carried out by changing the source to target distance during the thermal

evaporation. The morphology of the micro-stripes fabricated from these thin films was analysed with a surface profilometer and in both cases, the thickness of the micro-stripes was measured as ~ 20 nm. Subsequently, MACE was carried out by using these Au/Ag micro-stripes of different noble metals and also of different thicknesses. The following chapters include the various studies carried out for MACE of Si where these fabricated micro-stripes were used to optimise the chemical etching of Si leading to practical applications of these nano/microstructured Si substrates for SERS detection of chemical species.

CHAPTER 3

Metal-assisted chemical etching of Si by using Au/Ag micro-stripes as catalyst

3.1 Introduction

After successful deposition of various noble metal thin films and fabrication of micro-stripes out of these thin films by incorporating lithography and lift-off process, MACE was carried out by using these metal micro-stripes as a catalyst to fabricate microstructures on the Si substrate. For this purpose, three different batches of MACE experiments were carried out to find the optimised parameters for the fabrication nano/microstructures on Si substrate which were utilized as the SERS substrates. The first batch consists of the **TMS20Au** and **TMS20Ag** micro-stripes (20 nm Au and Ag micro-stripes fabricated from the thermally deposited Au and Ag thin films respectively) assisted MACE of Si. The second batch consists of three different micro-stripes **SMS20Au**, **SMS50Au** and **SMS140Au** (20, 50 and 140 nm Au micro-stripes fabricated from sputter deposited Au thin films) assisted MACE of Si. Similarly, the third batch consists of **MS1** and **MS2** (20 nm Au micro-stripes with different morphologies fabricated from the thermally deposited Au thin films) assisted MACE of Si. The whole experimental details of the MACE processes of all three batches and its outcomes are analysed and illustrated in this chapter.

3.2 Experimental procedure for MACE of Si

The advantage of this technique compared to the reactive ion etching (RIE) or other dry etching processes is that no requirement of any sophisticated instrument and hence cost-effective and simple [8]. Basically MACE process is a chemical etching process which is used to fabricate different nano/microstructure on Si surface. In MACE process an oxidising agent is reduced at the metal catalyst's surface and in the process produces holes (h^+) which are directly transferred to the Si present underneath of the catalyst in use. Owing to the insertion of holes, Si is oxidised and successively dissolve in HF [8,71]. A schematic representation of the local oxidation and dissolution during MACE of Si by Au metal micro-stripes is shown in Fig.3.1.

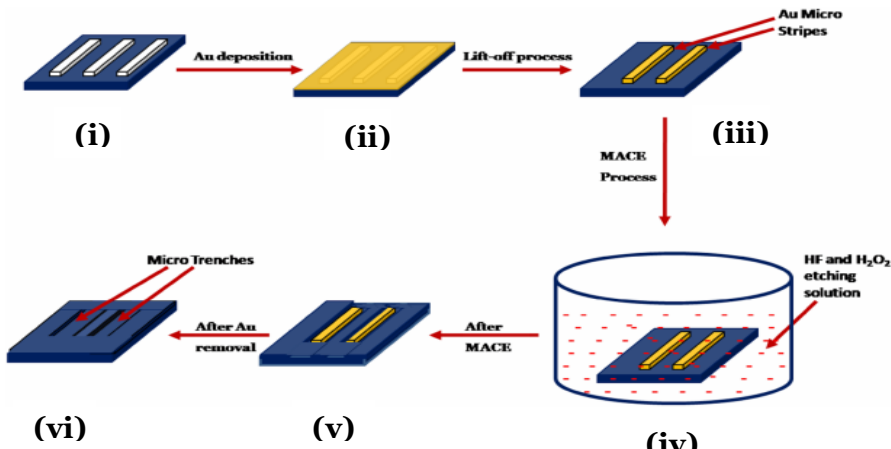


Fig.3.1: Schematic representation of the MACE process on Si substrate by using Au micro-stripes as catalyst 50

The whole MACE process can be understood stepwise which is clearly represented in the schematic diagram shown in Fig.3.1. The stepwise descriptions are mentioned in the next page.

- (i) Patterning of photoresist on Si by using UV lithography which is mentioned in the previous chapter.
- (ii) Deposition of Au/Ag thin film on the photoresist patterned Si substrate by thermal evaporation/sputtering as mentioned in chapter 2.
- (iii) Performing the lift-off process to pattern Au/Ag micro-stripes on Si substrate from the deposited Au and Ag thin films.
- (iv) Dipping of Au/Ag micro-stripes patterned Si substrates in the etching solution to etch out Si atoms from the interface of metal and Si.
- (v) Performing MACE process by using H_2O_2 and HF in presence of the metal catalyst for the desired time to form nano/microstructures on Si substrate.
- (vi) Removal of Au/Ag by using suitable etchant from the Si substrate after completion of the MACE process.

3.3 Effect of different metal catalysts on the formation of Si nano/microstructures

In this study, Au/Ag noble metal micro-stripes were used for Si etching in the presence of a mixture of 0.3 M H_2O_2 and 10 M HF which was used as the etching solution. The etching was carried out for 50 minutes at a constant temperature of $55^0 C$ which was maintained in a water bath. Followed by the MACE process, the Au/Ag micro-stripes were removed by using the etchant and the fabricated structures were analysed by FESEM which is discussed in the next sub-section.

3.3.1 20 nm Au/Ag micro-stripes as catalyst

The fabricated microstructures on Si by **TMS20Au** micro-stripes assisted MACE process is shown in Fig. 3.2. From the FESEM images as shown in Fig. 3.2, it is observed that the etching occurs on the surface of the Si substrate and the etch profile/micro trench keeps the similar dimensions with the micro-stripes used for the MACE process. Moreover, at the bottom of the trench rough surface is formed along with the randomly distributed nanopores. Similar results are also reported earlier [73, 74]. Thus, when 20 nm or less than 20 nm thick metal micro-stripes were used as a catalyst, then the nanopores on the metal micro-stripes led to the formation of such structures at the bottom of the trench.

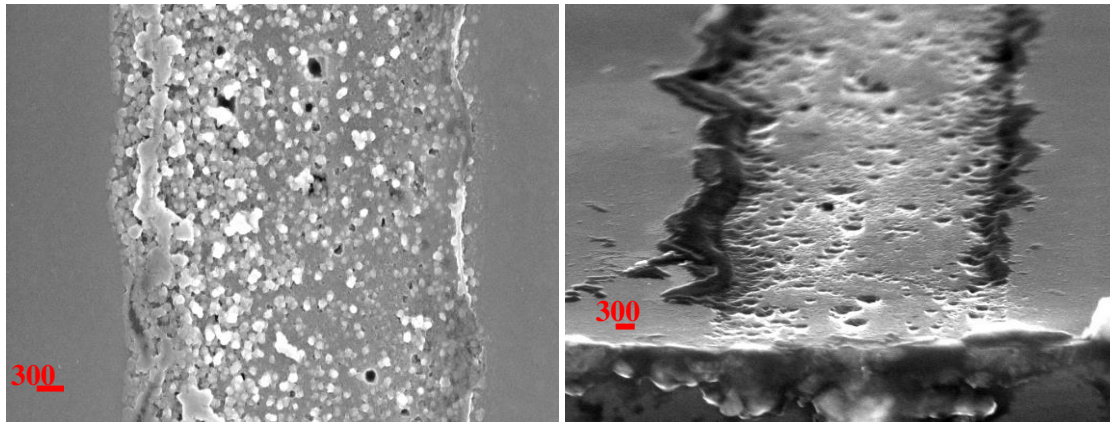


Fig.3.2: Si substrate after MACE by 20 nm thick Au micro-stripes (a) top view and (b) cross-section view

Similarly, MACE experiments were also carried out by using TMS20Ag micro-stripes as catalyst and characterised with FESEM which is shown in Fig. 3.3.

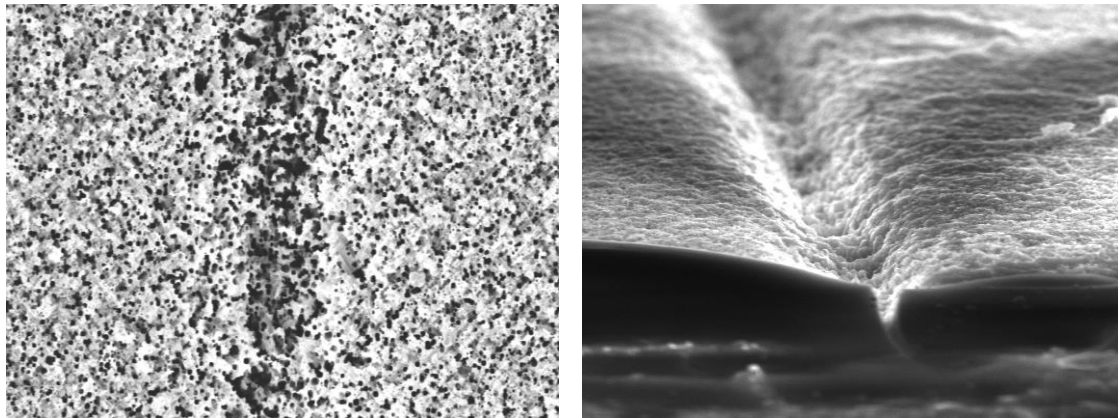


Fig.3.3: Si substrate after MACE by 20 nm thick Ag micro-stripes (a) top view and (b) cross-section view

From the FESEM images as shown in Fig. 3.3, a unique etching profile is observed. It is found that the micro trench nanopores are observed all nearby areas where the Ag metal micro-stripes are present after the MACE process. The formation of the nanopores can be explained on the basis of the oxidation stability of the noble metal catalyst during the MACE process. It is already reported earlier by Max Williams et al. [80] that the etching solution plays a major role in the dissolution of the metal catalyst during the etching process. In their study, they have reported that the Ag catalyst dissolves significantly during the etching process whereas Au catalyst remains stable and due to which unintentional etching happens elsewhere in the Si substrate. It is also seen from the FESEM images (Fig. 3.3) that the post-MACE Si substrate consists of the rough surface. Thus, we believe that these substrates are possibly good for the SERS measurement which will be discussed in following chapters. The

surface R.M.S. roughness of the post-MACE Si substrate was measured with AFM which is shown in Fig.3.4.

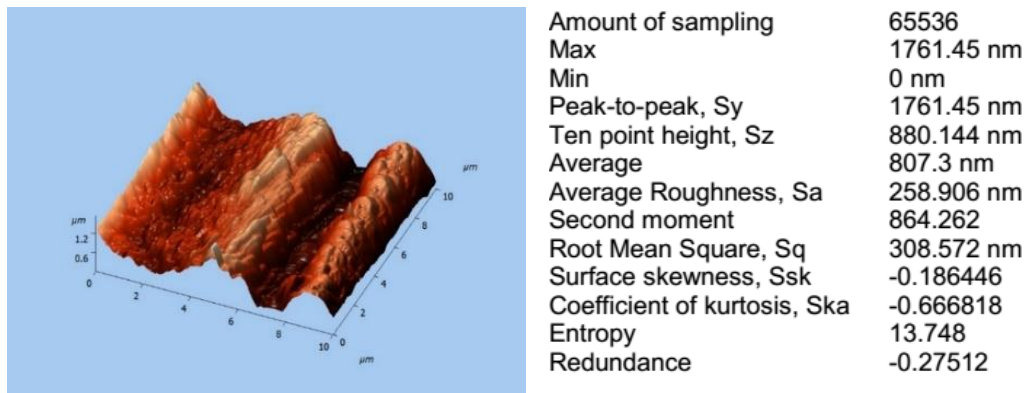


Fig.3.4: 3D AFM image of post-MACE Si substrate fabricated by Ag micro-stripes

From the AFM image, as shown in Fig 3.4, the RMS roughness of the post-MACE Si is found to be ~309 nm which is very high, hence, as per the requirement for the SERS-active substrate, this substrate [99] can be considered as a good candidate for the SERS measurements. Further studies on SERS measurement using this substrate were carried out and discussed thoroughly in chapter 4 of this thesis.

3.3.2 Effect of thermal annealing of metal micro-stripes on the formation of Si micro/nanostructures

After noticing unintended results such as the formation of whiskers along with nanopores at the bottom of the trench and also nanopores formation all over the Si due to the dissolution of Ag, we further carried out the research to overcome such difficulties. To understand these issues, both the Au and Ag micro-stripes were annealed at 200⁰ C for 30 minutes in open air condition by using a hot plate. Both the annealed and un-annealed Au and Ag 20nm thick micro-stripes were analysed by FESEM and shown in Fig.3.5 and 3.6 respectively.

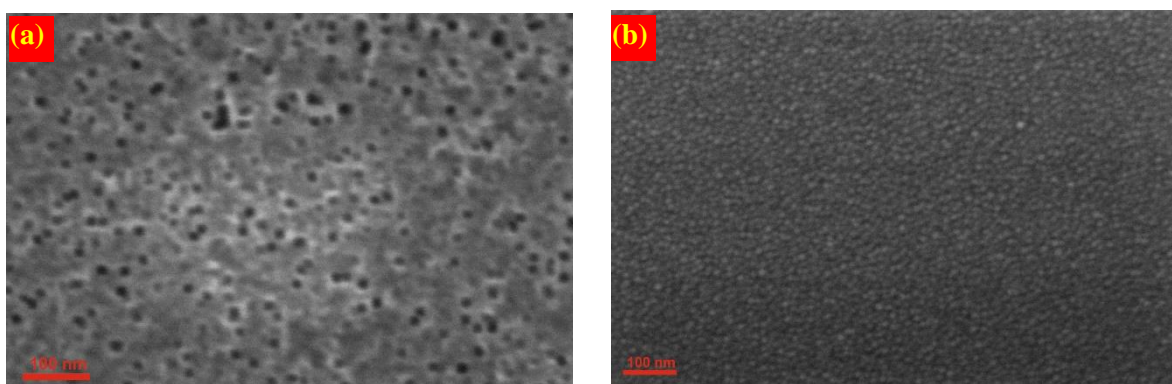


Fig.3.5. FESEM images of the patterned Au micro-stripes (TMS20Au) on Si substrate (a) As-deposited (b) after annealing at 200°C.

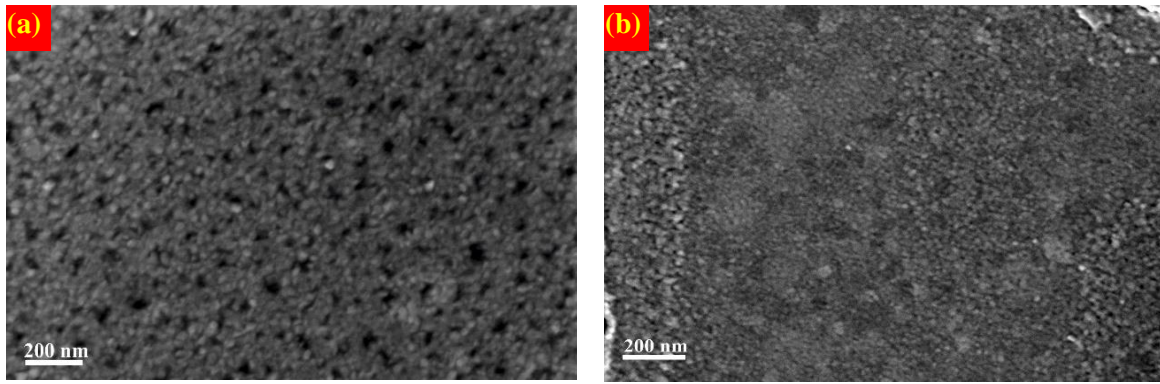


Fig.3.6. FESEM images of the patterned Ag micro-stripes (**TMS20Ag**) on Si substrate (a) As-deposited (b) after annealing at 200°C .

Similarly, for 20 nm Ag micro-stripes were also annealed in open air condition at 200°C for 30 minutes by heating in a hot-plate. In this case, also the nanopores were eliminated by annealing which can be observed from the FESEM images shown in Fig.3.6. As shown in Fig. 3.5 and 3.6, nanopores are not present in both the samples after thermal annealing process.

Then, these annealed and un-annealed samples are chosen for MACE process. After the annealing, both the Au and Ag annealed micro-stripes coated Si substrates were used for MACE where the etching solution composition was kept identical as discussed earlier. The MACE process for both the Au and Ag catalyst was carried out for 50 minutes at 55°C which was maintained by a water bath. Followed by chemical etching, Au or Ag catalysts were removed from these substrates and characterised by FESEM which is shown in Fig.3.7 and 3.8 respectively.

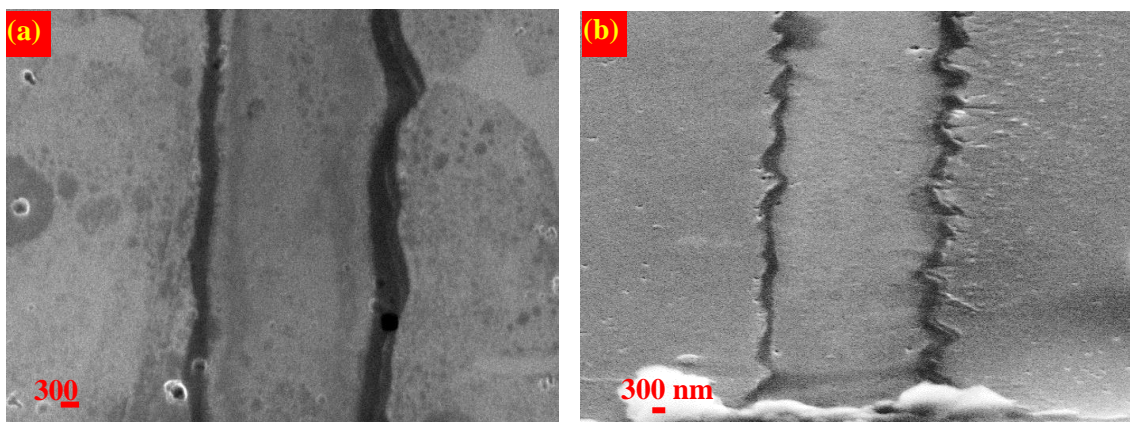


Fig.3.7: Si substrate after MACE by annealed Au micro-stripes (a) top-view and (b) cross-section view

From the FESEM images as shown in Fig. 3.7 (a) and Fig. 3.7 (b), it is clearly seen that roughness at the bottom of the trench significantly decreases and also the nanopores are not

present. The possible reason for obtained result may be due to the thermal annealing effect which eventually eliminates the nanopores present in the Au catalyst micro-stripes (Fig. 3.6). From the FESEM analysis, it is clearly observed that the nanopores which were present in the micro-stripes were eliminated after the annealing process. Possibly due to this reason, the out-of-plan etchants and by-products transport is not possible and a smooth bottom is observed in the micro-trenches. In case of Ag as the metal catalyst, the presence of nanopores in it and dissolution of the metal catalyst during the etching process creates unintended structure in the Si substrate. These problems could be solved for Ag catalyst by annealing the catalyst micro-stripes. The FESEM analysis was carried out for the Si substrate after the etching process which is shown in Fig.3.8. From the FESEM analysis, it is observed that there is no such unintended nanostructure or microstructures were fabricated on the surface of the Si substrate which resembles the similar results obtained for the Au micro-stripes assisted chemical etching process.

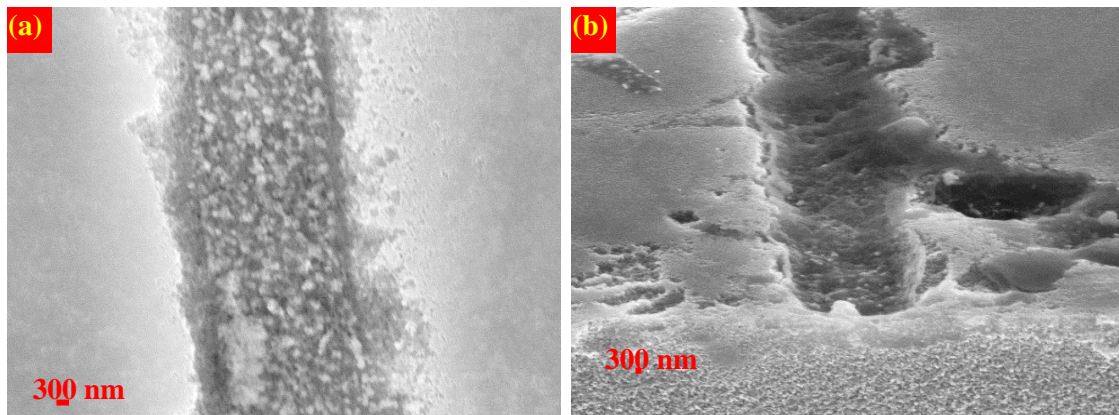


Fig.3.8: Si substrate after MACE by annealed Ag micro-stripes (a) top view and (b) cross-section view

3.4 Effect of the thickness of the Au micro-stripes on the formation of Si microstructures

As the **TMS20Au** micro-stripes assisted MACE was not able to fabricate neither nanoporous nor inverted pyramid structures which are very much desirable to use the substrate as a SERS substrate, further MACE study was carried out with the **SMS20Au** micro-stripes based Si substrates. The main difference between these two type of Au micro stripes such as **TMS20Au** and **SMS20Au** is the Au thin film deposition process only, i.e. thermal evaporation and RF sputtering respectively. The metal catalyst deposition and Au micro stripes formation on Si were thoroughly discussed in the previous chapter of the thesis. In this

section, the influence of metal micro-stripes thickness on the formation of the microstructures in p-Si (100) substrates by MACE process is discussed. Furthermore, a systematic study was also carried out to understand the effect of the oxidising agent in the MACE process when annealed Au micro stripes used as the catalyst for the process and also discussed in the following sub-sections.

Annealing of Au micro-stripes deposited by RF sputtering for MACE of Si

The as-deposited Au micro stripes on the Si substrate as mentioned in Chapter 2 of this thesis, was taken for the investigation. Similar to the annealing process carried out for the **TMS20Au** and **TMS20Ag** micro-stripes, the **SMS20Au** micro-stripes were also annealed in the open environment by using a hot plate where the annealing temperature was maintained at 200°C . In this case also annealing was carried out for 30 minutes and then the substrates were cooled down to the room temperature. The main idea behind this post-deposition annealing was to alter the physical properties of the Au micro stripes and to study the subsequent effect on MACE process of Si. The Fig.3.9 shows the FESEM images of the Au micro-stripes on Si as-deposited and annealed sample.

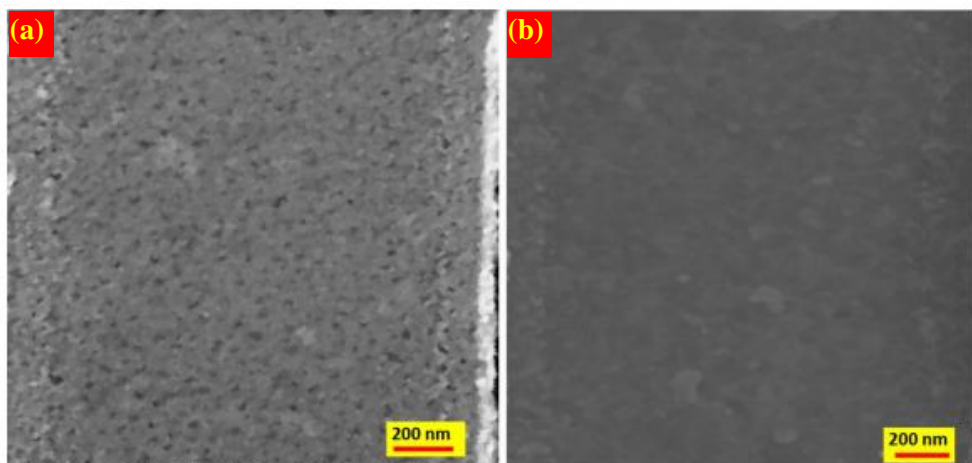


Fig.3.9: FESEM images of the patterned Au micro-stripes on Si substrate (SMS20Au) (a) As-deposited (b) after annealing at 200°C .

It is observed from the Fig.3.9 (a) that the nano-pinholes are present in the as-deposited Au micro stripes whereas, after the annealing process, these pinholes are not present as shown in Fig.3.9 (b). Further, these annealed micro stripes of different thicknesses were directly used in MACE process along with un-annealed micro stripes to understand the effect of annealing on the MACE of Si.

MACE of Si by using SMS20Au micro-stripes as catalyst

In the previous section, it is understood that the annealing process changes the surface morphology of metal thin micro stripes and that impacts the MACE process. By owing to the surface morphological changes in the micro stripes, the MACE was carried out for both annealed and un-annealed **SMS20Au** micro stripes in an etching solution comprised of 0.3 M H₂O₂ and 10 M HF for 50 minutes and at 55° C which was maintained by a water bath. As soon as the etching was completed, Si substrate coated with Au micro stripe was dipped in the Au etchant solution and followed by cleaning in acetone and double distilled water respectively so as the unwanted chemical species can be removed from the substrates. As the cleaning process was over, the cleaned substrates were characterised with FESEM which is shown in Fig.3.10 and 3.11.

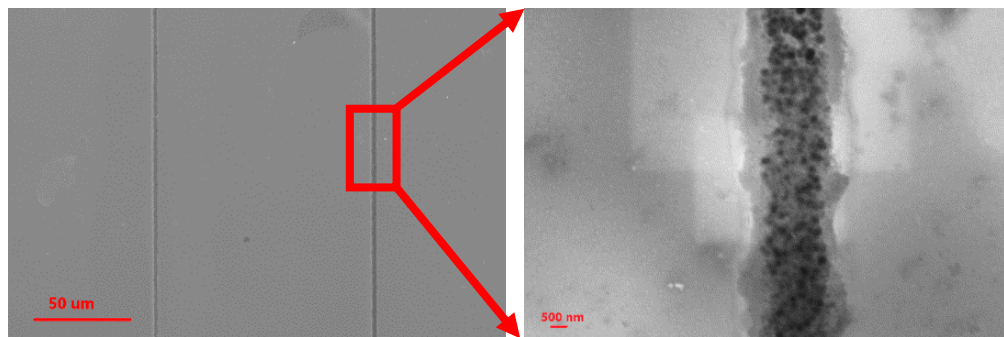


Fig.3.10: Top view of Si substrate after MACE by un-annealed **SMS20Au** micro-stripes

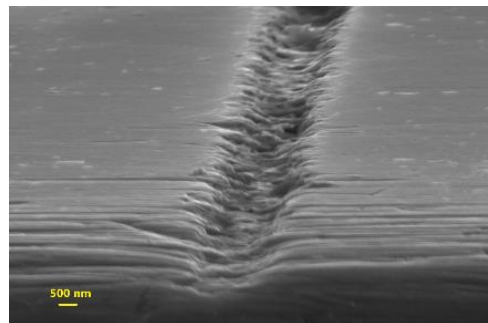


Fig.3.11: Cross-section view of Si substrate after MACE by un-annealed **SMS20Au**

Similarly, MACE of Si was carried out with annealed SMS20Au micro-stripes and the FESEM images of the etched Si substrate are shown in Fig. 3.12 and 3.13. It is seen from the FESEM analysis result that both un-annealed and annealed **SMS20Au** micro-stripes are not able to form rough surfaces on Si substrate. But, in both cases micro trenches on the Si substrate are seen where annealed **SMS20Au** micro-stripes form deeper trenches than the un-annealed one as shown in the Fig. 3.11 and Fig. 3.13.

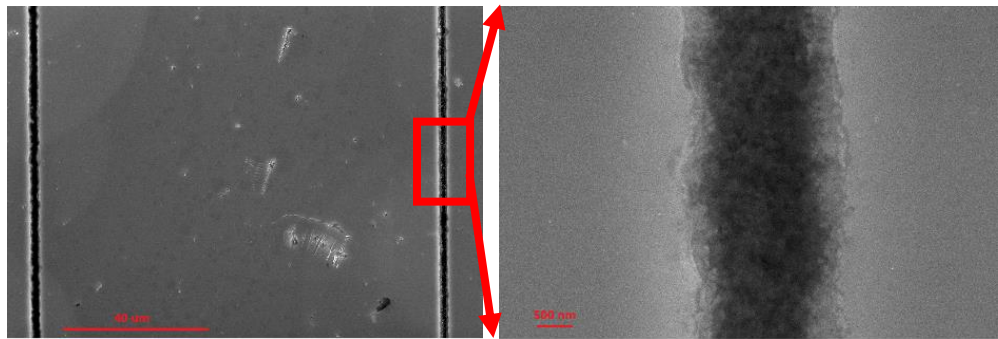


Fig.3.12: Top view of Si substrate after MACE by annealed **SMS20Au**

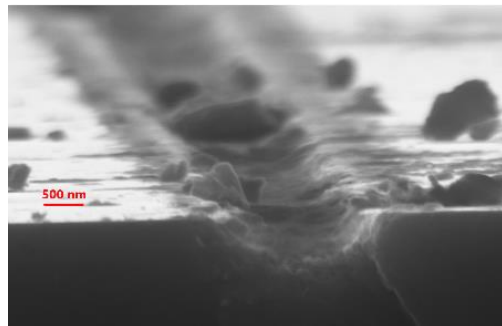


Fig.3.13: Cross-section view of Si substrate after MACE by annealed **SMS20Au**

It is well accepted that during MACE process, the regions where the metal catalyst is in contact with the Si are etched out and in the process different nano/microstructures are formed in the Si substrate. Therefore, when annealed micro-stripes were used as catalyst for MACE of Si, micro trenches with the smoother bottom surface was obtained since the annealed micro-stripes are free from the nanopores. Therefore, it is confirmed that based on annealing rough to the smooth bottom surface Si-microstructures could be achieved. Further, few MACE experiments were carried out by varying the thickness of the micro stripes, those were annealed prior to the MACE process. The following section involves the study of the effect of the thickness of the annealed metal catalyst on the formation of the Si-micro structures.

Analysis of thickness effect on MACE of Si by Au catalyst micro-stripes

Two samples **SMS50Au** and **SMS140Au** with thicknesses about 50nm and 140nm were chosen to investigate the thickness effect of the micro stripes on MACE process. FESEM images are shown in Fig.3.14 (a-d) for samples **SMS50Au** and **SMS140Au**, respectively.

As shown in Fig.3.14 (a) and (b), slight etching occurs in the areas underneath the edges of the Au micro stripes which were in contact with the substrate. For the sample **SMS50Au**, uniform etching occurs in the Si substrate when thick (**SMS140Au**) annealed micro stripes were used as shown in Fig. 3.14 (c) and (d).

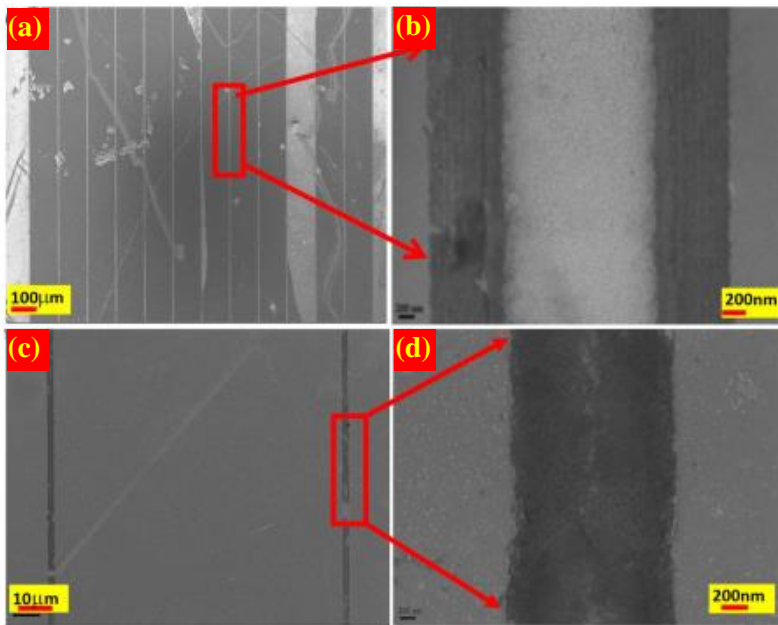


Fig.3.14. FESEM images of chemically etched p-Si (100) substrates where etching was done by using annealed (a,b) **SMS50Au** and (b,d) **SMS140Au** micro stripes

The possible reason for such behaviour is that when an annealed thin or thick micro stripe is used for MACE, the absence of nano-pinholes in the Au stripe inhibit the mass transportation of the etchant through the Au stripe and reach to the Au-Si interface. Due to this reason, only the lateral mass transport of the reacting species occurs under the edges of the Au micro stripes where the metal-Si contact exists. The second possible reason may be related to the width of the Au micro stripes. It was confirmed from FESEM image (as shown in Fig.2.18) that the width of the Au micro stripes is more than $3\text{ }\mu\text{m}$ and which can be a limiting factor for various etch profiles formed in the Si substrate by different thicknesses of the metal catalyst micro stripes. It is already reported by Geyer et al. [71] that bending of the metal micro stripe occurs at the centre of the same when the lateral dimension of the micro stripe is more than $3\text{ }\mu\text{m}$. Moreover, during MACE process hydrogen (H_2) bubbles are formed underneath of the metal micro stripes and are not able to escape due to the absence of the nano-pinholes in the Au stripes which led to bending of the stripes. The FESEM cross-sectional view of the Si substrates (Fig.3.15) after MACE process was carried out by **SMS50Au** micro stripes clearly shows that during the etching process, bending of the Au catalyst occurs and which etched the substrates only at the edges underneath the catalyst stripes. However, in the case of **SMS140Au** metal micro stripes, no bending occurred due to the higher stiffness of these thick stripes. Also, Au-Si interface was always present everywhere underneath the metal micro stripes and etching occurs in all places in contact with the metal catalyst micro-stripes (Fig.3.15).

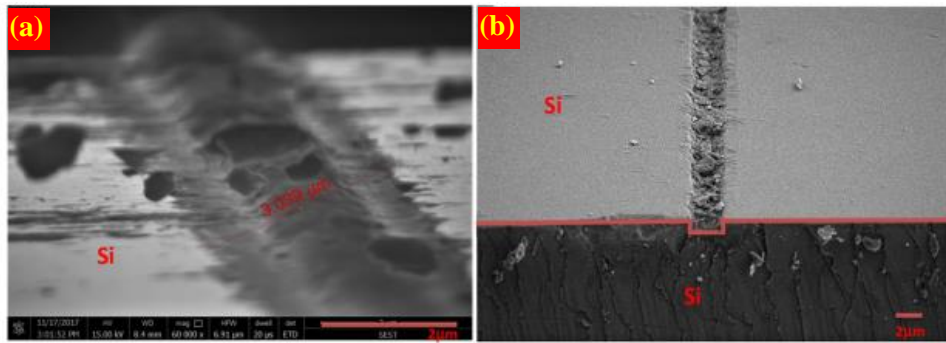


Fig.3.15. FESEM cross-section images of MACE chemically etched p-Si (100) substrates by using (a) SMS50Au thin and (b) SMS140Au thick annealed Au micro stripes

The whole mechanism associated with the MACE of Si by using two different annealed metal micro stripes with various thicknesses is represented graphically in Fig.3.16.

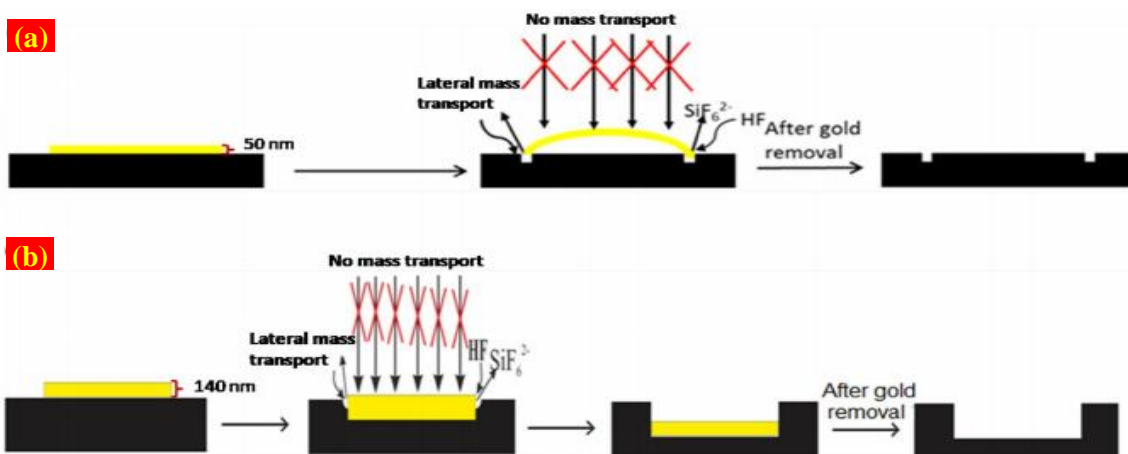


Fig.3.16. Schematic representation of the proposed mechanism of the MACE process by using an annealed Au micro stripe of (a) 50 nm and (b) 140 nm thicknesses and width more than 3 μm

The depth of the etched patterns formed on the p-Si (100) substrate was measured with an optical surface profilometer as shown in Fig. 3.17 (a) and (b).

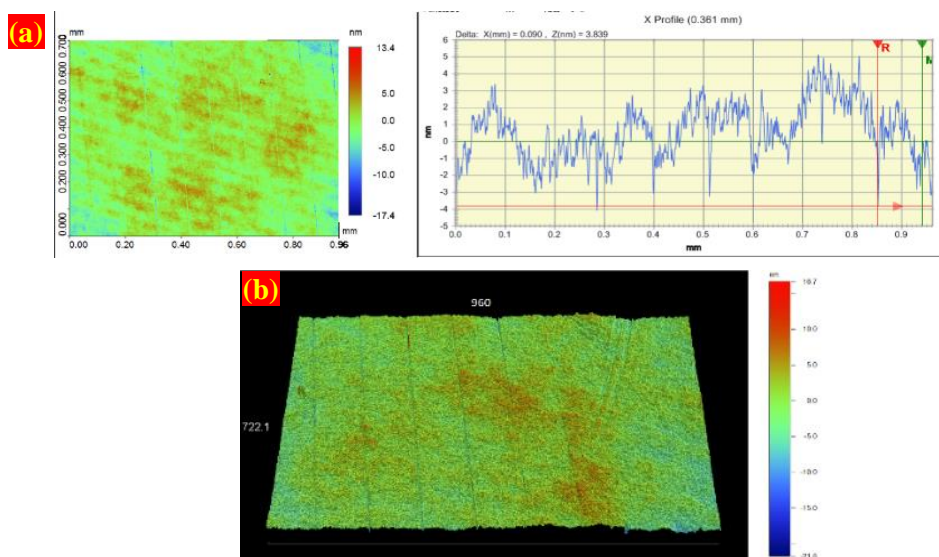


Fig.3.17. Optical surface profilometer images (a) 2-D and (b) 3-D of etched p-Si (100) substrate after MACE by Au strip of 50 nm 60

On the other hand, when 140 nm thick Au micro stripe acts as metal-catalyst etching occurs nicely as the bending of Au strips doesn't happen. Thus, Si atoms are etched anisotropically everywhere beneath the stripes as shown in Fig.3.18 (a) and (b). As the thickness of Au strips increases the stiffness of these stripes also increases. Due to this the trench's depth also increases from 4 nm to 9 nm which can be attributed to the depth profile of optical surface profilometer (Fig.3.18a).

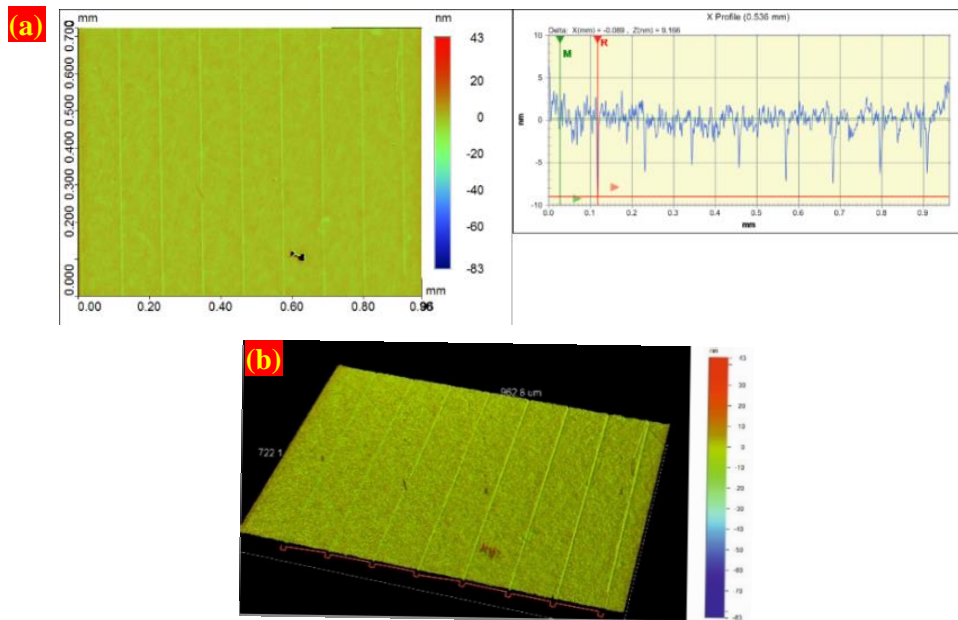


Fig.3.18: Optical surface profilometer images (a) 2-D and (b) 3-D of etched p-Si (100) substrate after MACE by Au strip of 140 nm

It is already known that the etching of Si occurs when an Au-Si interfaces present during the MACE process, therefore in case of 140 nm thick Au stripes, the metal-Si interface present everywhere underneath of these stripes and which allows the etchant solution to etch the Si atoms. In the process, Au micro stripes dig into the Si substrate forming uniform microstructures in it which can be visualised from the 3D image of a surface profilometer (Fig.3.18). Thus, the experimental results indicate that etching does not occur in Si, if the Au-Si interface is not present. Furthermore, to understand the role of the oxidising agent in the chemical etching of Si, the concentration of the oxidising agent i.e. H_2O_2 was increased from 0.3 M to 0.5 M. With the same concentration of the dissolution agent i.e. HF as investigating the effect of the oxidising agent. The etching time and etching temperature were also kept constant. Since, 140 nm thick annealed Au micro stripes showed better etching behaviour than the 50 nm thin annealed Au micro stripe, the effect of the oxidising agent on MACE was investigated by using the 140 nm Au micro stripes. After the MACE process, the Si substrate

was dipped in Au etchant to remove the Au micro stripes from the substrate. Subsequently, a cleaning process was carried out with acetone and DI water for 10 minutes each. Following the cleaning process, the substrate was analysed with FESEM where a different etching profile was found which is shown in Fig. 3.19 (a) and (b).

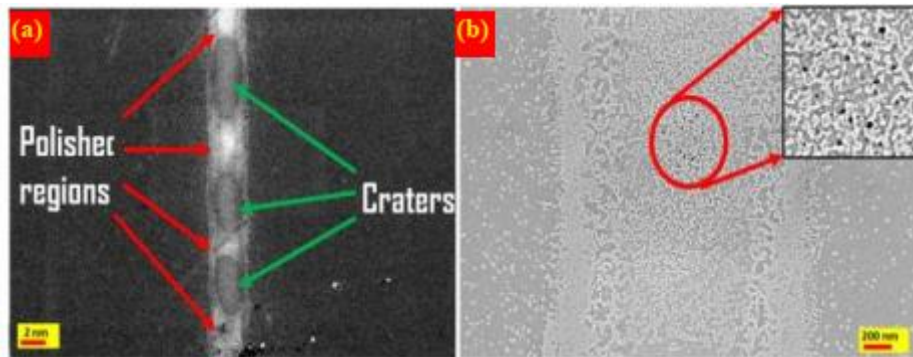


Fig.3.19. Typical FESEM images of (a) p-Si (100) substrate after MACE and followed by removal of Au micro stripes (140 nm) with higher concentration of H_2O_2 and (b) enlarged view of polished region formed after the MACE process

It is seen from FESEM images that two different regions were formed in the Si substrate after performing the MACE process by using thick annealed Au stripes as the catalyst. These two regions can be distinguished as the polished region and craters (Fig.7a). It is already reported that two different sources of holes take part in the MACE process of Si such as one source of holes is from the catalytic decomposition of H_2O_2 in the metal-liquid interface and the other one is from the trapped holes inside the doped Si substrate. These trapped holes are basically taken part in the etching process as they are released under the metal catalyst and can access the metal-Si interface. [100]. Therefore, with the increasing concentration of H_2O_2 , generation of holes also increases due to a higher rate of catalytic decomposition of the oxidising agent in the metal-liquid interface. Eventually, these holes pass through the metal and reach to the Si underneath of it. Therefore, we hypothesize that a repulsion occurs between the catalytically decomposed holes and the trapped holes which are present in the highly doped region of the Si substrate. This is why the generated holes move away from the highly doped regions and eventually get less time to stay and take part in the MACE process in those areas. As a result, in the highly doped regions of the Si substrate, no etching occurs instead polishing takes place with nanopores formation as shown in the image in Fig.3.19 (b). In contrast, in the lightly doped regions, no repulsion occurs between the generated holes and trapped one as the number of holes trapped in these regions are less. Due to which the generated holes can stay for a longer time and can take part in the etching process of Si. In

this way, the Si atoms are etched out from the lightly dopes regions and form craters in the substrate. Therefore, during the MACE process, combined polished regions and craters are formed under the metal catalyst micro stripes.

3.5 Effect of morphology of the metal catalyst on the formation of Si microstructures

In the previous section, the annealing effect of the noble metal catalyst micro-stripes on the MACE of Si has extensively explored. Similarly, this section deals with the morphological effect of the metal micro-stripes in the MACE process of Si. Different morphology of the Au micro stripes were fabricated as mentioned in chapter 2. The details of the whole process and respective characterisations are already mentioned in chapter 2. After the fabrication of the Au micro-stripes on Si substrate (as confirmed by XRD and EDX in chapter 2), the morphology of these stripes were characterised with FESEM and atomic force microscopy (AFM). These results are mentioned in the next sections of this chapter. For simplicity, the micro-stripes fabricated from the Au thin film where the film was deposited by maintaining the distance between the source and substrate at 10 cm is named as **MS₁** and similarly for 12 cm source to substrate distance as **MS₂**.

FESEM analysis of the surface morphology of the fabricated micro-stripes

The FESEM images of MS₁ and MS₂ are shown in Fig. 3.20 and 3.21. As shown in the Fig 3.20 and 3.21, the morphology of the micro-stripes are not same for the sample MS₁ and MS₂. This changes in the morphology due to the deposition rate of the vapour atoms which can be linked to the average kinetic energy of these atoms [101].

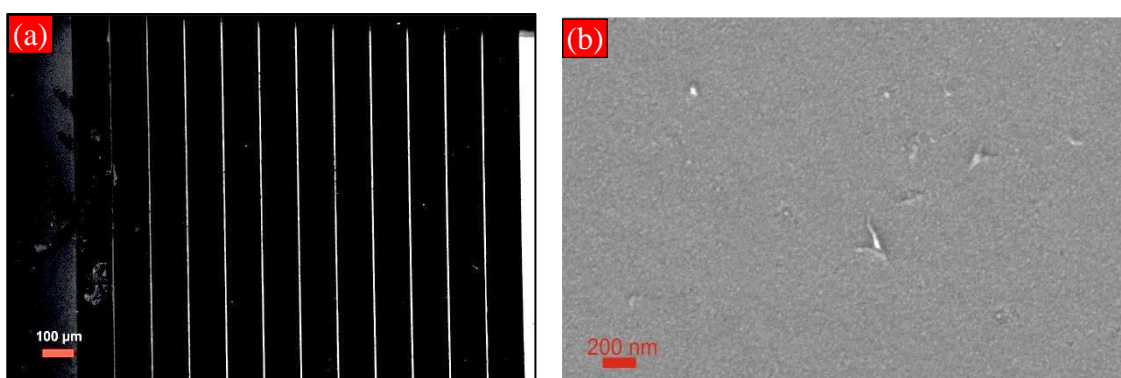


Fig.3.20: FESEM images of **MS₁** (a) Low and (b) High magnification

It is already known that the thermal evaporation process involves at a high vacuum level which is less than the 10^{-4} Torr range, and at this range, the mean free path of the vapour atoms equivalent to the dimension of the vacuum chamber and hence the atoms evaporated

from the source travel towards the substrate in a straight line [101]. Due to this shadowing phenomenon, it is possible that uneven deposition occurs. Moreover, the binding energy of the vapour atoms with the substrate also plays a prominent role in film homogeneity.

It has been reported that if the kinetic energy of these atoms is smaller than the binding energy, then the morphology of the thin film is more inhomogeneous [101]. For example, in case of Au, at the evaporation temperature of it which is 1400^0 C , the average kinetic energy per atom is calculated as 0.2 eV [101]. But, this average kinetic energy is smaller than the binding energy of atoms in a material and this implies that the atoms reach to substrate with low energy which normally affects the morphology of the deposited film [101]. Moreover, both the depositions were carried out by using resistive heating where the same current was applied at the source and hence the vapour atoms possess the same energy. Therefore, when the distance between the source and substrate increases the vapour atoms reaching to the substrate would have lesser energy and which changes the deposition rate. It is also earlier reported that at room temperature Au thin film deposition, variation in the deposition rate changes the roughness of the thin film and for higher deposition rate roughness of the thin film is less [95].

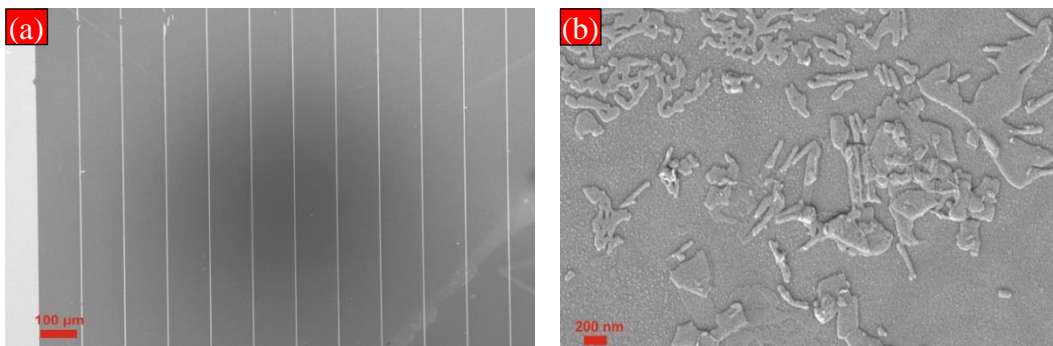


Fig.3.21: FESEM images of **MS₂** (a) Low and (b) High magnification

So, all these facts evidence that the possible reason for obtaining the fractal-like structures in Au thin films (Fig.3.21) when the source to substrate distance increases to 12cm from 10cm. The purity of the sample **MS₁** and **MS₂** was identified by XRD and EDX analysis, as mentioned in chapter 2. Furthermore, the surface roughness and topography study were carried out by AFM for both the **MS₁** and **MS₂** samples (Fig.3.22 and Fig.3.23). It is found from the AFM analysis that with the increase of source to substrate distance, the roughness of the thin films increases, which is consistent with the earlier reported result [95].

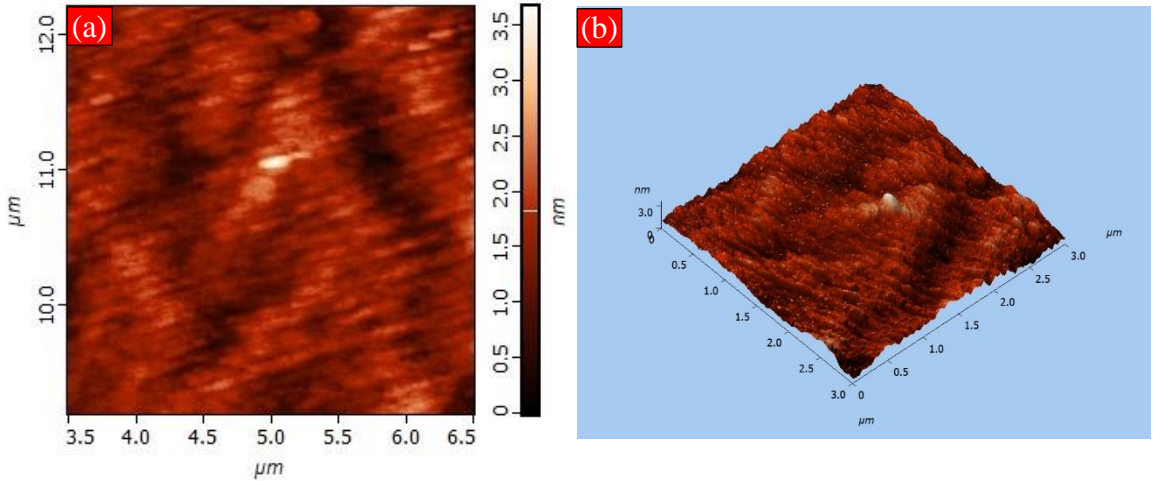


Fig.3.22: AFM images of Au thin film deposited by fixing source to substrate distance at 10 cm

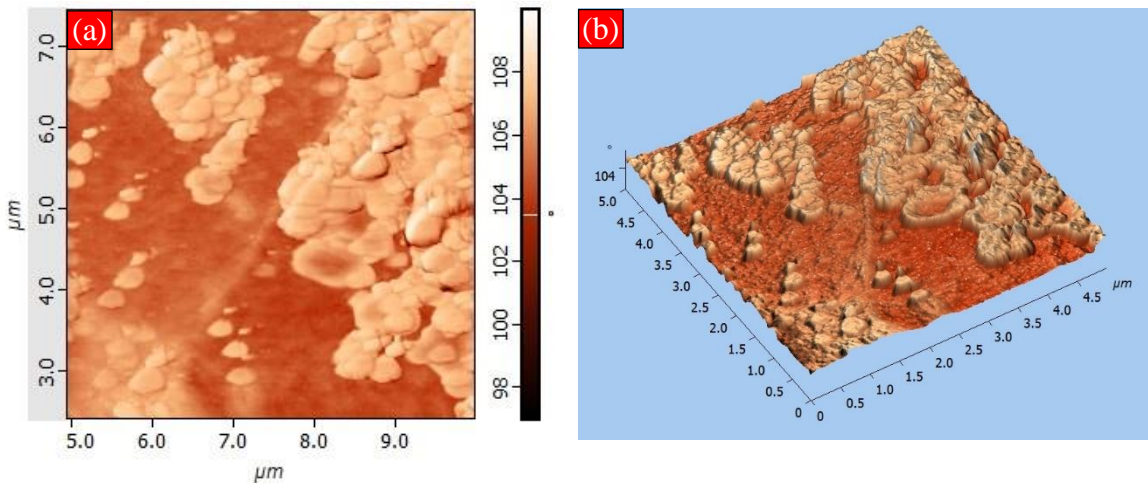


Fig.3.23: AFM images of Au thin film deposited by fixing source to substrate distance at 12 cm

Table 3.1: Roughness values for the thin films deposited with different source to substrate distance

The distance between source and substrate	R.M.S. roughness value (nm)
10 cm	0.37
12 cm	0.77

Similarly, from the XRD analysis, as shown in section 2.2.3.3, it is observed that with the increase of source to substrate distance, crystallite size decreases which can be visualised from the decreasing trend in the intensity of the peak as shown in Fig.2.13. Then these two MS₁ and MS₂ micro-stripes based samples were used for MACE process which is discussed in the next section.

MACE of Si by Au micro-stripes with different morphologies

Metal-Assisted Chemical Etching of Si was carried out by using an etching solution composed of HF and H₂O₂ in a ratio 10 M and 0.5 M respectively, at 55° C for 30 minutes by

using a hot water bath. The etchant and etching conditions are identical for both the samples MS₁ and MS₂. After completion of the etching process, the Au metal catalyst was removed by dipping the Si substrates in aqua regia solution and subsequently analysed the microstructures formed in substrates by FESEM which are shown in Fig. 3.24.

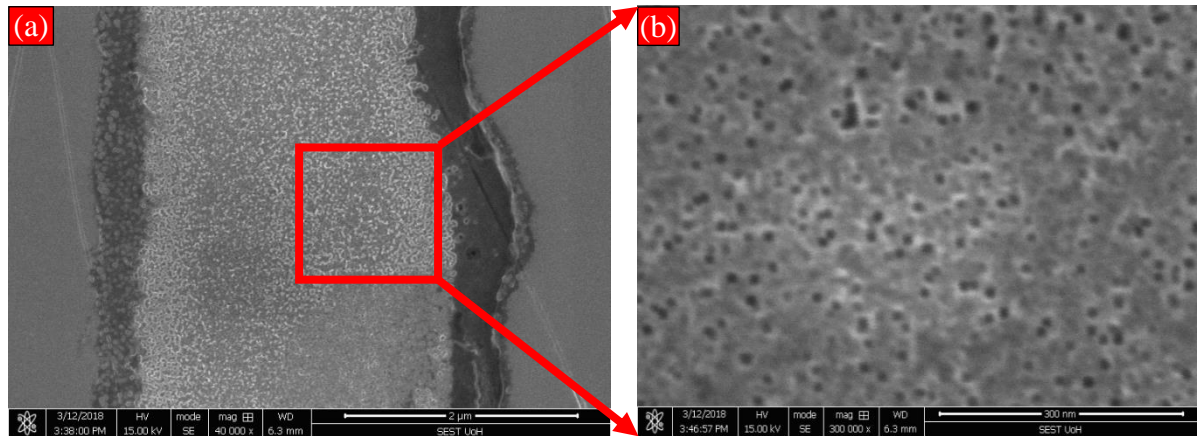


Fig.3.24: FESEM images of Si substrate after MACE by **MS₁ micro-stripes** (a) as a catalyst and (b) its magnified image of the area shown in Fig. 3.24 (a)

From FESEM analysis Fig. 3.24, it is observed that the etching happens in the areas where the metal catalyst stripes were present and the rest of the areas were left un-etched. However, few nanopores are observed at the bottom of the etched area which is formed due to the nanopores were present in the micro-stripes.

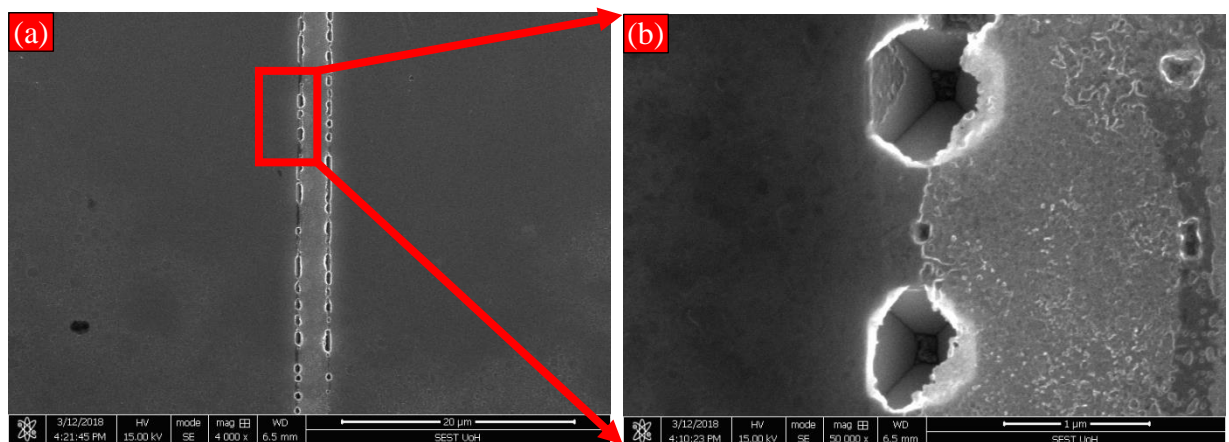


Fig.3.25: FESEM images of Si substrate after MACE by **MS₂ micro-stripes** (a) as a catalyst and (b) zoomed area of the related region in Fig. 3.24 (a)

From FESEM analysis as shown in Fig. 3.25, it is clearly observed that the etching occurs where metal catalyst micro-stripes are present and additionally underneath area of the micro-stripes' edges a different type of etching profile is observed. This different and unique inverted pyramid structures are formed very much periodically throughout both the edges of

the micro-stripes occupied area. For further depth analysis of these microstructures, AFM analysis was performed for both the Si substrate etched by MS₁ and MS₂ micro-stripes which are shown in Fig.3.26 a and b.

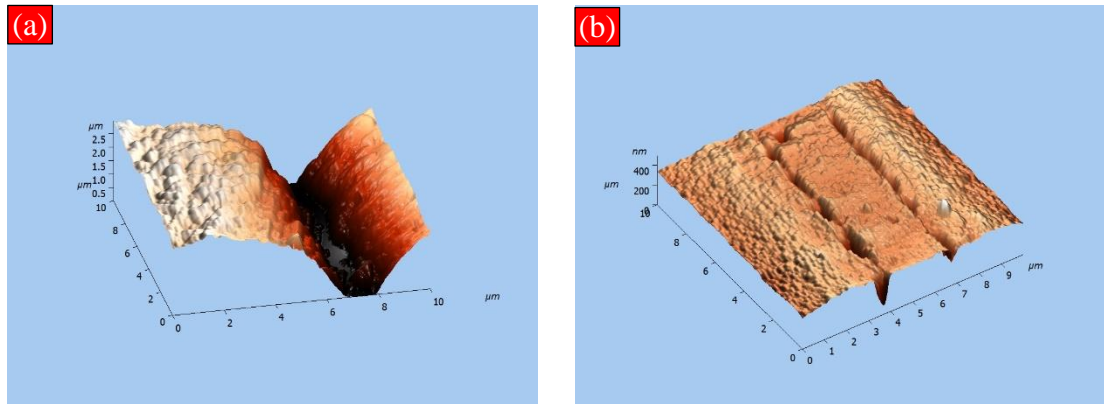


Fig.3.26: 3D AFM images of Si substrate after MACE by (a) MS₁ and (b) MS₂ micro-stripes

From 3D AFM images also similar results are observed for MS₁ and MS₂ micro-stripes assisted MACE of Si. The depth of the etch profiles are calculated from the AFM depth profile analysis which is shown in Fig.3.27 and 3.28.

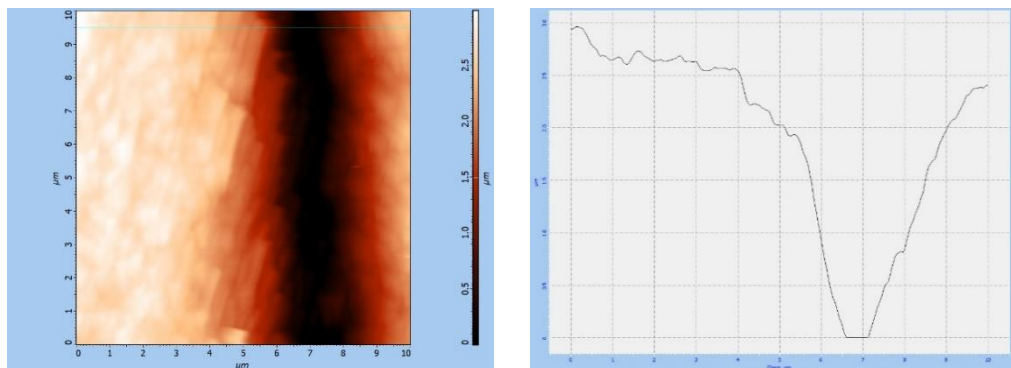


Fig.3.27: AFM depth profile analysis of Si substrate after MACE by MS₁ micro-stripes

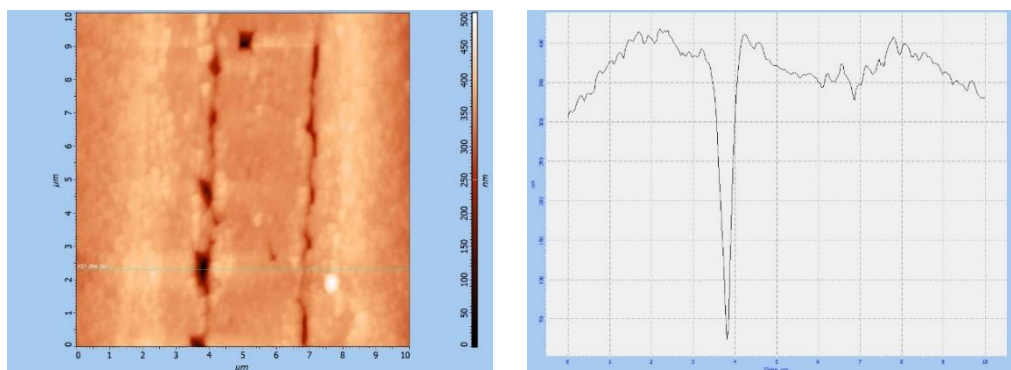


Fig.3.28: AFM depth profile analysis of Si substrate after MACE by MS₂ micro-stripes

It is found from the AFM depth analysis that the micro trenches fabricated on the Si substrate by **MS₁** micro-stripes have 2 μm depth whereas the depth of the inverted pyramid structures fabricated by **MS₂** micro-stripes is ~ 350 nm. It is worth to mention that several researchers have fabricated inverted pyramidal structure by MACE process for different applications such as photovoltaic cell fabrication, commercial SERS substrate etc. where they have reported that microstructures are fabricated all over the surface. But, in our study, we have obtained the microstructure (inverted pyramid) periodically along both edges of a trench. Thus, we believe that this kind of Si-microstructure can be applied to different applications. We have applied these substrates as SERS substrates for detection of a Raman active chemical species with ultra-low concentration.

3.6 Conclusions

MACE of Si was carried out by using both 20 nm thick Au and Ag micro-stripes. The experimental results indicate that the presence of nanopores in the Au micro-stripes form a rough surface at the bottom of the micro-trench fabricated in the Si substrate along with the random distribution of the nanopores. Similar results were also found for Ag micro-stripes assisted MACE process. However, unwanted nanopores were observed all over the substrates when Ag metal micro-stripes were used as a metal catalyst and the possible reason may be due to the dissolution of Ag catalyst during the etching of Si. These problems could be successfully eliminated by thermal annealing process where the metal catalyst micro-stripes were annealed prior to the MACE process. This new experimental finding possibly opens a new direction for fabricating smooth microstructures in Si substrate by MACE process.

Further, the effect of post-deposition thermal annealing of the micro-stripes catalyst on MACE of Si was also investigated by using the Au micro-stripes (fabricated from the thin films deposited by RF sputtering with 20 nm and 140 nm thick metal micro-stripes) as a catalyst. MACE of Si was carried out by using 20 nm annealed and un-annealed thin Au micro-stripes as catalyst and the FESEM results revealed that annealed **SMS20Au** micro-stripes form smoother and deeper trenches than the un-annealed micro-stripes catalyst because the nano-pinholes are not present in the micro stripes after thermal annealing. A similar result was also obtained when the annealed and un-annealed **TMS20Au** micro-stripes were used as catalyst. Two more annealed Au micro-stripes such as **SMS50Au** and **SMS140Au** were also applied as catalyst for MACE process. Because of the absence of the nano-pinholes in the catalyst surface, Si etching occurs under the edges of the Au micro-

stripes where the Au-Si interface is present. Moreover, it is also found from the experimental results that the annealed Au micro-stripes with higher thickness etch Si uniformly in comparison to the annealed Au micro-stripes with lower thickness. Furthermore, with increasing concentration of the oxidising agent, uniform Si etching did not occur. Instead, a combination of polishing regions and craters were formed in the Si substrate.

The experimental results revealed that when 20 nm Au micro-stripes deposited with different growth morphologies by thermal evaporation, act as a metal catalyst for MACE by keeping identical etching parameters, different etch profiles are obtained in the Si substrate. Thus, it signifies the morphological dependency of the catalyst on MACE of Si. In case of Au micro stripes (**MS₁**), uniform etching occurs in all the areas underneath the metal micro-stripes catalyst present, however, when **MS₂** with different growth morphology act as metal catalyst, inverted pyramid structures is obtained at the edges of the micro-stripes. The Si microstructures those were fabricated by using the 20 nm thick Ag metal micro-stripes and 20 nm thick Au-micro-stripes as a catalyst were considered further to apply as SERS-active substrates for chemical detection of MB by Raman signal. The following chapters will discuss the SERS substrate preparation and SERS measurements of Raman active chemical species.

CHAPTER 4

Application of nano/microstructure-based Si substrates for SERS detection of chemical species (MB)

4.1 Introduction

This chapter deals with the SERS-active substrate preparation and SERS measurement by using the Si substrates consisting of fabricated nanopores and inverted pyramidal microstructures as discussed earlier in chapter 3. The nanopores on Si substrate were fabricated by un-annealed 20 nm thick Ag micro-stripes and the fabrication of inverted pyramidal structure on Si substrate by 20 nm Au micro-stripes with different growth morphology as discussed in chapter 3. These two nano/microstructured Si substrates were chosen for SERS measurements due to two main reasons. Firstly, the SERS substrates should be rough surface (Au/Ag/Cu). Secondly, commercial Klarite substrates, those consist of the inverted pyramid structure are fabricated in the Si platform. In addition to this, a plastic replication of Klarite substrate with pyramid and the inverted pyramid was studied by Xu et al. [102] and they have reported that the enhancement factors for inverted pyramid structure is higher than the pyramid structure. Therefore, the SERS measurements were carried out for these substrates where methylene blue (MB) was used as the probe material for targeting the food industries. The enhancement factors were evaluated for both the Si nano/microstructure based substrates and have been reported in this chapter.

4.2 A brief idea about SERS

Surface-enhanced Raman spectroscopy, in short SERS, is a powerful analytical technique which was discovered in the mid-1970. With the advent of this powerful diagnostic technique, the low detection sensitivity of Raman spectroscopy is not an issue any more and it can be used for detection of chemical species for several applications. Basically, SERS associates with the surface plasmon resonance and nanostructure-enhancement phenomenon where the intensity of Raman signal is amplified by several orders which enable single molecule detection by this technique. Apart from this, there are few more factors responsible for the enhancement of the Raman signal and cannot be explained based on the classical electrodynamics. These various enhancement mechanisms are classified as the chemical effect which mainly includes the photon-driven electron transfer. To understand the basic and distinctive difference between the Raman technique and SERS technique a schematic diagram is shown in Fig. 4.1 [103].

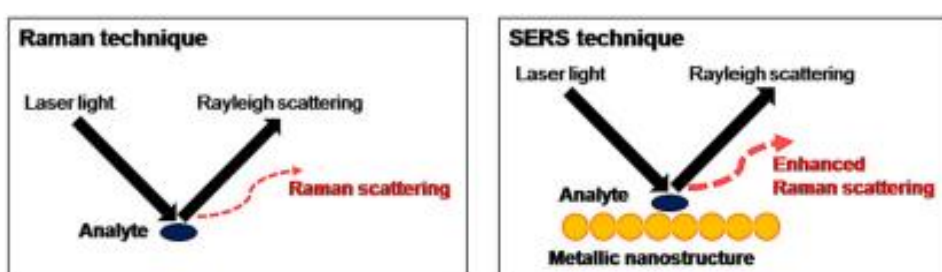


Fig.4.1: Illustration of SERS mechanism [103]

4.3 Experimental procedure for SERS detection

A portable Raman spectrometer (i-Raman® Plus by B&W Tek) near-infrared laser with a wavelength of 785 nm and 100 mW power was used for the excitation of the SERS substrate. The laser integration time was set at 5 seconds for 3 times average. The whole setup for the SERS detection is shown below.

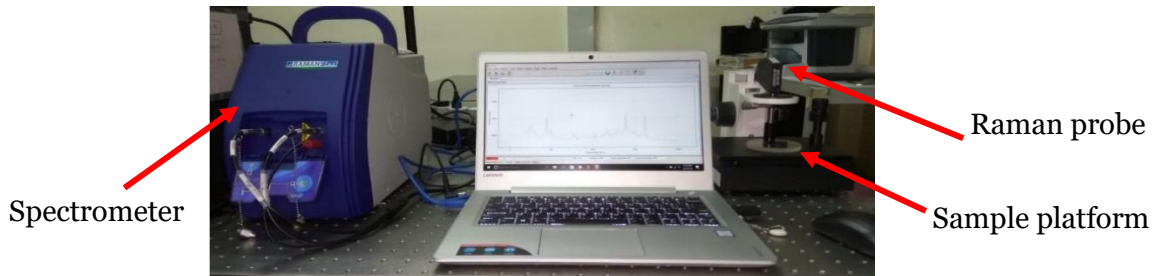


Fig.4.2: Portable Raman spectrometer used for SERS detection

All the nano/microstructure Si-based SERS substrates, those were prepared by MACE process, acted as SERS-active substrate for the SERS measurements to detect Methylene Blue (MB). MB was purchased from Sigma-Aldrich and which was used as the probing material. In this regard, different concentration of MB starting from 0.1 M to 10 pM were prepared by diluting the powder of MB in ethanol to detect the minimum concentration by SERS technique. The detailed procedure for SERS measurements is mentioned elaborately in the next section.

4.4 SERS detection by the nano/microstructured Si substrate

In the experimental process, two different nano/microstructured Si substrates, those were prepared by using MACE process, were used to prepare the SERS substrates. These substrates are indexed as the **AgSiM** (with nanoporous micro trenches) and **AuSiM** (with inverted pyramidal structures), those were fabricated by **TMS20Ag** and **MS2** micro-stripes respectively. For the SERS measurements, the Si substrates consist of the nano/microstructured **AgSiM** and **AuSiM** were considered. A few steps were followed to perform SERS measurements which are mentioned below:

1. After MACE process, the Si substrates were dipped in aqua regia (a mixture of hydrochloric acid and nitric acid, optimally in a molar ratio of 3:1) or concentrated nitric acid separately to dissolve Au or Ag present in the substrates.
2. Then the substrates were cleaned in acetone, isopropanol (IPA) and double distilled water to remove any contamination present in the substrates.
3. Subsequently, the cleaned substrates were characterised by FESEM for the testing of the micro/nanostructures formation on the substrates as shown in Fig.4.3.

4. For SERS study, the substrates were coated with Ag NPs (details characterisation of these NPs are mentioned in section 5.3) by drop casting where these NPs were dispersed in IPA with 0.004 W/V% concentration (Fig.4.4).

5. Finally, the Ag NPs coated Si substrates were deposited with 20 μ L methylene blue (50 nM) by drop casting and subsequently the SERS measurements were carried out by using methylene blue (MB) as the probe material (Fig.4.5).

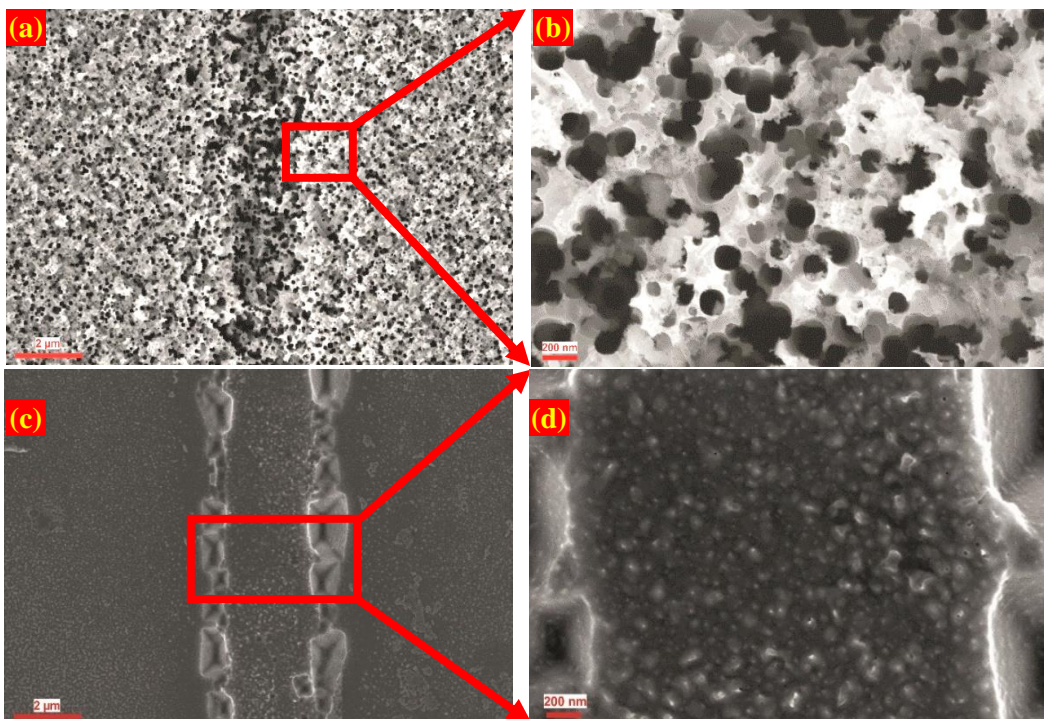


Fig.4.3: FESEM images of p-Si (100) substrate after MACE process (a, b) by using Ag micro-stripes, (c, d) Au micro-stripes as catalysts.

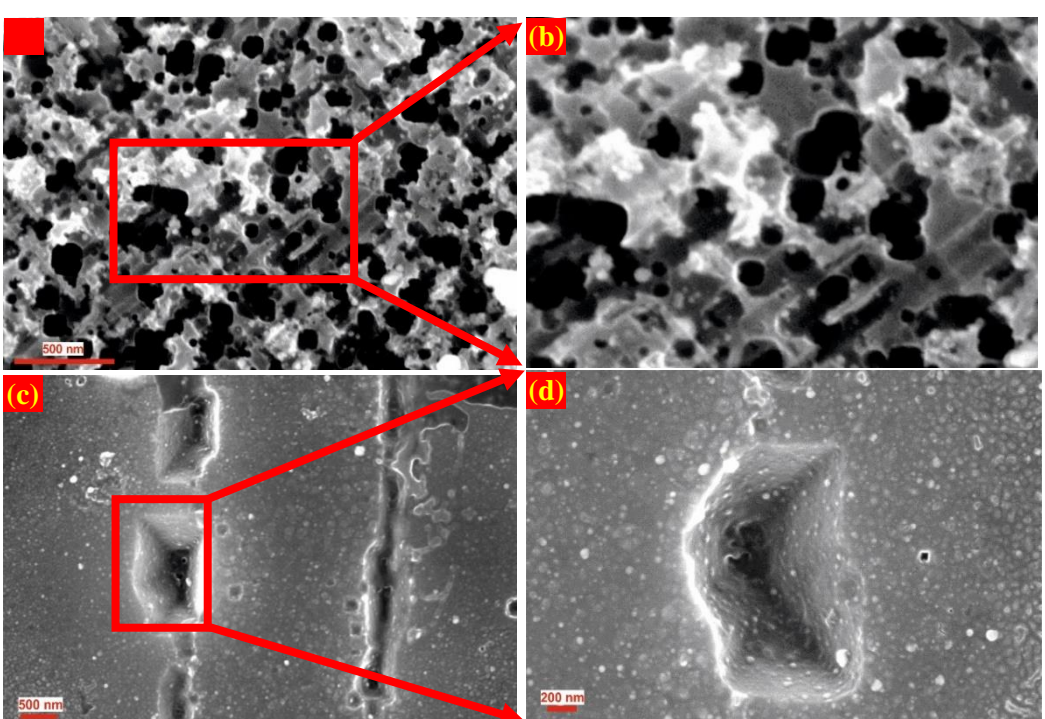


Fig.4.4: FESEM images of (a,b) AgSiM and (c,d) AuSiM substrates deposited with Ag NPs

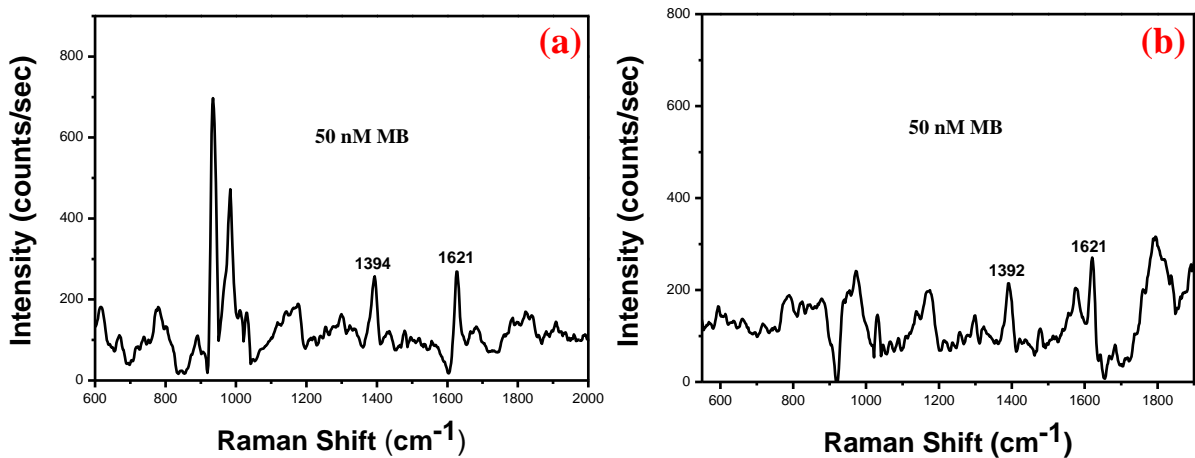


Fig.4.5: SERS spectra of MB of 50 nM detected by micro/nanostructured Si substrate prepared by (a) Ag assisted MACE process, (b) Au assisted MACE process

Fig.4.5 shows the Raman spectra for the Ag NPs coated on **AgSiM** and **AuSiM** substrates. As shown in the Fig.4.5, two characteristics peaks of MB appear at 1621 cm⁻¹ and 1394 cm⁻¹ and these are assigned to C-C ring stretching and C-N symmetrical stretching [104, 105]. The efficiency of these substrates was measured by calculating the enhancement factor and the details about the calculation are mentioned below.

The enhancement factor (EF) of the SERS effect is calculated by using the following formula [106, 107].

$$EF = \frac{I_{SERS}}{I_{Raman}} \times \frac{C_{HC}}{C_{LC}}$$

Where,

I_{SERS} = integrated intensity of highly elevated Raman bond of analyte molecule under consideration from the NP/NS surface

I_{Raman} = integrated intensity of the same bond obtained on a Si substrate

C_{HC} = high concentration of analyte molecule generating the normal Raman intensity from the Si substrate

C_{LC} = low concentration of analyte molecule generating the Raman intensity from the nanostructures substrate

To calculate EF, we performed the SERS measurement on MB deposited p-Si (100) substrate and which eventually gives the I_{Raman} value. From the following plot, I_{Raman} is calculated from the most intense peak which is at 1621 cm⁻¹ and the intensity is found as 3310 counts/sec.

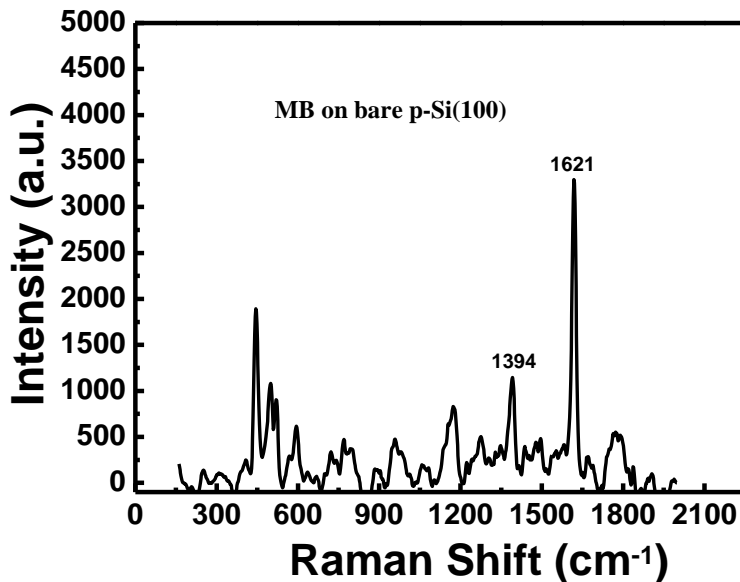


Fig.4.6: SERS spectra of MB of 0.1 M detected by bare Si substrate

Therefore, EF for the SERS substrate produced by Ag micro stripes assisted MACE process is calculated as mentioned below —

$$I_{\text{SERS}} = 263 \text{ counts/sec}, I_{\text{Raman}} = 3310 \text{ counts/sec}, C_{\text{HC}} = 0.1 \text{ M}, C_{\text{LC}} = 50 \text{ nM}$$

$$\therefore \text{EF} = \frac{275}{3310} \times \frac{0.1}{50 \times 10^{-9}} = 1.7 \times 10^5$$

Similarly, EF for the SERS substrate produced by Au micro stripes assisted MACE process is calculated as mentioned below—

$$I_{\text{SERS}} = 270 \text{ counts/sec}, I_{\text{Raman}} = 3310 \text{ counts/sec}, C_{\text{HC}} = 0.1 \text{ M}, C_{\text{LC}} = 50 \text{ nM}$$

$$\therefore \text{EF} = \frac{270.5}{3310} \times \frac{0.1}{50 \times 10^{-9}} = 1.6 \times 10^5$$

Both the SERS substrates show almost similar value for enhancement factor, but the SERS intensity is little higher for the nanoporous Si substrate as compared to inverted-pyramid Si substrate. So, to understand the impact of the substrate on the enhancement factor, few more SERS measurements were carried out with the nanoporous Si substrate fabricated with Ag micro-stripes assisted MACE process. For that purpose, first, a cleaned Si substrate without any nano/microstructure fabricated on the surface of it, but coated with Ag NPs was tested for SERS and is shown in Fig.4.7. As shown in Fig.4.7, the detection of MB is possible by a normal and also with the bare surface, but the signal is pretty poor and almost lost in the

background noises. Likewise, another study was carried out to understand the impact of the modified Si substrate alone.

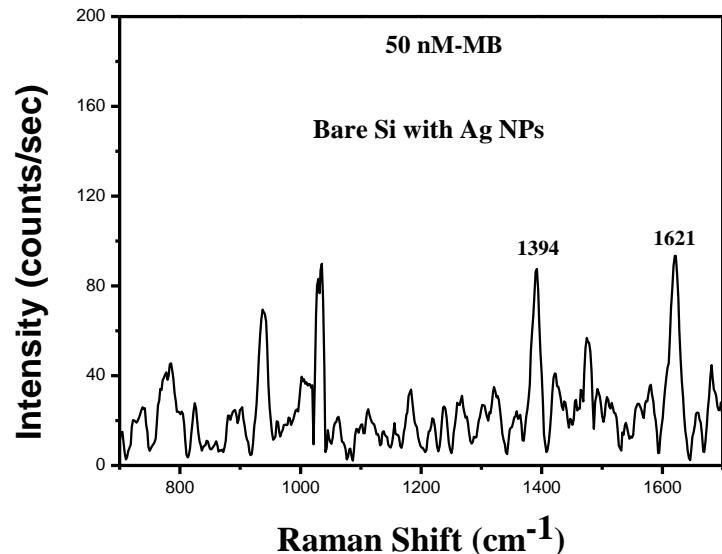


Fig.4.7: SERS spectra of 50 nM MB detected by a Si substrate (without any micro/nanostructures on the surface) coated with Ag NPs

In this regard, the Si substrates which consist of the nanostructures prepared by the Ag assisted MACE process were tested for SERS by using 50 nM MB as the probe material. Raman spectra of SERS measurement by using this modified Si substrate is shown in Fig.4.8. It is clearly seen from the Fig.4.8 that 50 nM concentrated MB could not be detected by the surface modified substrate. Whereas, with the same substrate the 50 nM concentrated MB was detected when it was incorporated with the Ag NPs as shown in Fig.4.5 (a). So, it is confirmed that neither the Ag NPs nor the surface modified substrate is self-sufficient to detect MB with a low concentration in the order of 50 nM. Rather, a combination of the surface modified Si substrate with Ag NPs are required to detect such a low concentration MB molecule.

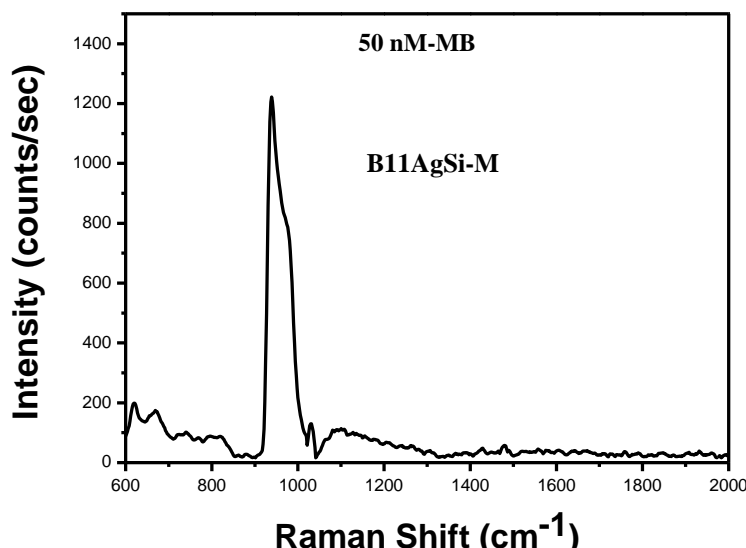


Fig.4.8: SERS spectra of MB of 50 nM tested with a MACE modified Si substrate without coating any noble metal on the surface of the substrate 76

But, for single molecule detection, the detection limit should go further down and at the same time, the value of the enhancement factor should increase. Thus, experimental results indicated that for better Raman signal (SERS intensity), the nanoporous Si substrate is a better choice, to achieve further lower detection limit. Furthermore, a recent work as reported by Bi-Shen Lee et al. [89] showed that an Au metal layer could be used to avoid trapping of the Raman signals by silicon nanowires and the Raman signal can be improved for the detection of malachite green (MG). Being inspired by their work, a new experiment was carried out to enhance the Raman signal where a combination of Au discontinuous thin film and Ag NPs were incorporated with the nanoporous Si substrate (as prepared by MACE process) to enhance the lower detection limit of MB. The details of all the optimisations are discussed in the next section.

4.5 Effect of the discontinuous Au thin film on SERS detection limit

In order to improve the enhancement factor and also for smaller concentration limit detection of MB, a thin layer of the gold discontinuous film was deposited before coating the Ag NPs on the MACE modified Si substrate. The Au thin film of 10 nm was deposited by thermal evaporation and details of the deposition is mentioned in Table 4.1.

Table 4.1: Deposition parameters for discontinuous thin film deposition by thermal evaporation

Parameters	Values
Base pressure	1×10^{-6} mbar
Source to substrate distance	10 cm
Substrate rotation	3 rpm
Deposition current	140A
Deposition time	1 min

The morphology, purity and thickness of the discontinuous Au thin film were investigated by using FESEM, EDX and surface profilometer measurements. The morphological study of the thin film by FESEM is shown in Fig.4.9.

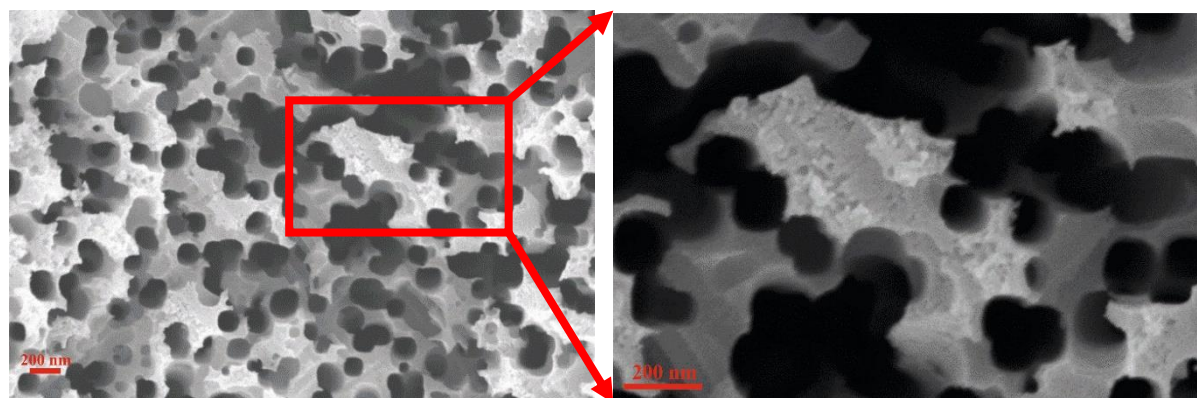


Fig.4.9: Thin film of Au deposited on the MACE Si substrate (using 20 nm Ag micro-stripes) by thermal evaporation for SERS measurement 77

The elemental analysis of the deposited thin film was carried out by using EDS to verify the purity of the deposited discontinuous Au thin film which is shown in Fig.4.10.

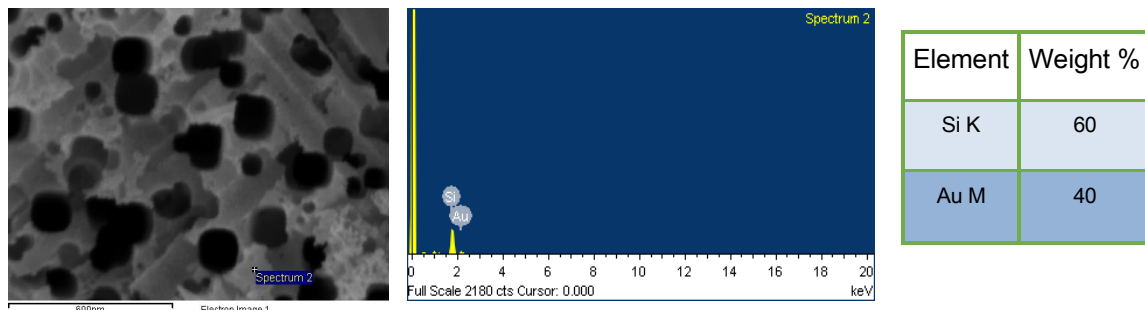


Fig.4.10: EDX analysis of the evaporated thin film on (Ag micro-stripes assisted) MACE modified Si substrate

As shown in the Fig.4.10, EDX analysis reveals that no other foreign element is present in the deposited Au thin film and the Si is shown up because of the Si substrate. Thus, almost pure Au was deposited on the MACE Si substrate (AgSiM). The thickness of the deposited thin film was measured by using a surface profilometer which is shown in Fig.4.11. It was found that a thin film of ~ 10 nm was deposited on the AgSiM substrate.

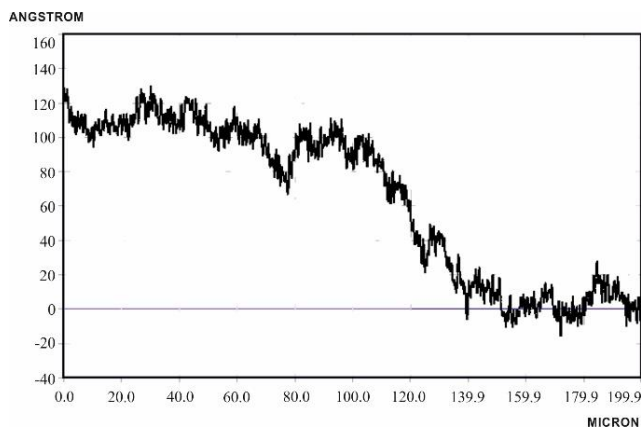


Fig.4.11: Surface profilometer plot of the deposited 10 nm Au thin film on nanostructured AgSiM substrate

The discontinuous Au thin film deposited MACE surface modified Si substrate was coated with Ag NPs and further examined for SERS by using the same probe material, i.e. MB of 5 nM as shown in Fig.4.12. From Fig.4.12, two characteristics peaks of MB appear at 1626 cm^{-1} and 1392 cm^{-1} , those are assigned to C-C ring stretching and C-N symmetrical stretching respectively. The most intense peak is shifted from 1621 cm^{-1} to 1626 cm^{-1} which may be due to the chemisorption of MB on the surface of gold. These results are in good agreement with the earlier value reported in the literature [108]. Similarly, EF for this SERS substrate is calculated which is mentioned in the next page—

$$I_{\text{SERS}} = 312.4 \text{ counts/sec}, I_{\text{Raman}} = 3310 \text{ counts/sec}, C_{\text{HC}} = 0.1 \text{ M}, C_{\text{LC}} = 5 \text{ nM}$$

$$\therefore \text{EF} = \frac{312.4}{3310} \times \frac{0.1}{5 \times 10^{-9}} = 1.8 \times 10^6$$

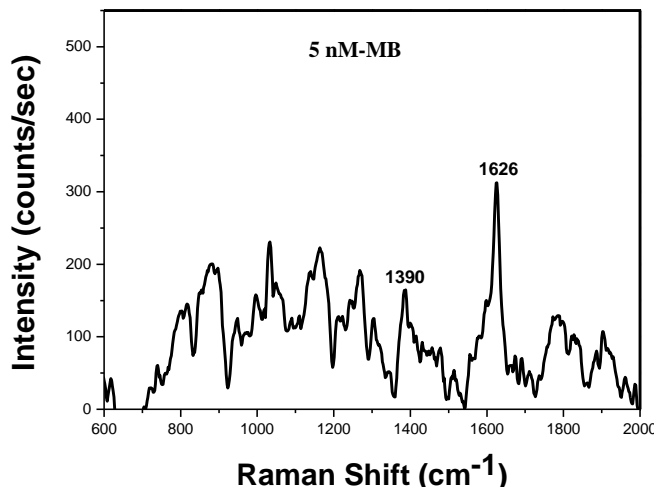


Fig.4.12: SERS spectra of MB of 5 nM detected by 10 nm discontinuous Au thin film and Ag NPs coated nanostructured Si substrate produced by Ag assisted MACE process

It is observed that the detection limit is reached up to 10^{-9} level (5 nM) and at the same time there is an increment in the enhancement factor by 10 times. The possible reason for the enhancement in the detection limit of the MB is that the thin discontinuous layer of Au deposited on the nanoporous Si possibly forms smaller metal nanoaggregate or specifically Au islands. These Au islands can be featured as the Au NPs with average size 100-200 nm. These nanoaggregates or Au islands show different plasmon resonances which in turn possibly change the position of the C-C ring stretching peak. A similar result was also obtained as shown in FESEM image (Fig.4.13), which confirms the presence of the Au-island on the surface of the Si substrate. This plays the vital role in the SERS detection by acting as the hotspots for this measurement.

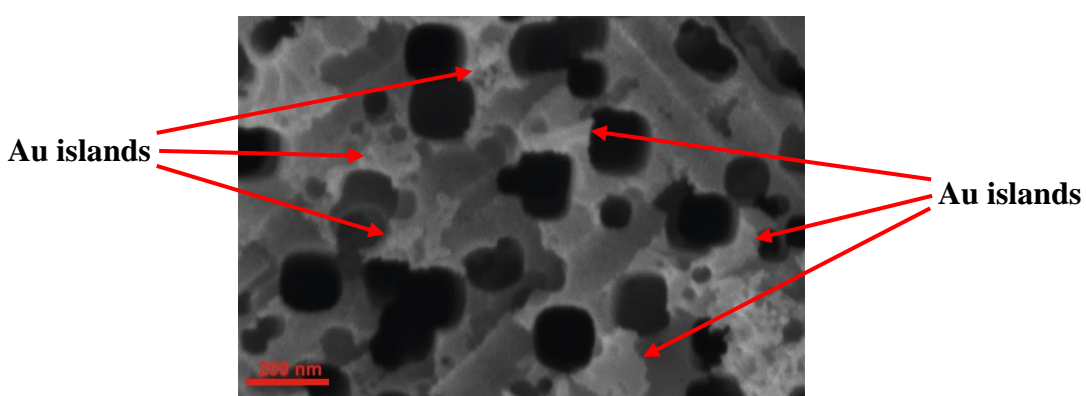


Fig.4.13: FESEM image of 10 nm Au discontinuous thin film coated nanoporous Si substrate fabricated by Ag assisted MACE process

The experimental results indicated that the discontinuous Au thin film on the nanoporous Si enhanced the detection limit of the MB and also the enhancement factor. Thus further studies were carried out to understand the effect of the discontinuous Au thin film on the enhancement of the detection limit. For this purpose, 10 nm Au thin film coated on bare Si substrate (without changing the MACE nanoporous Si substrate) was used in the SERS measurement for the detection of MB of 5 nM which is shown in Fig.4.14.

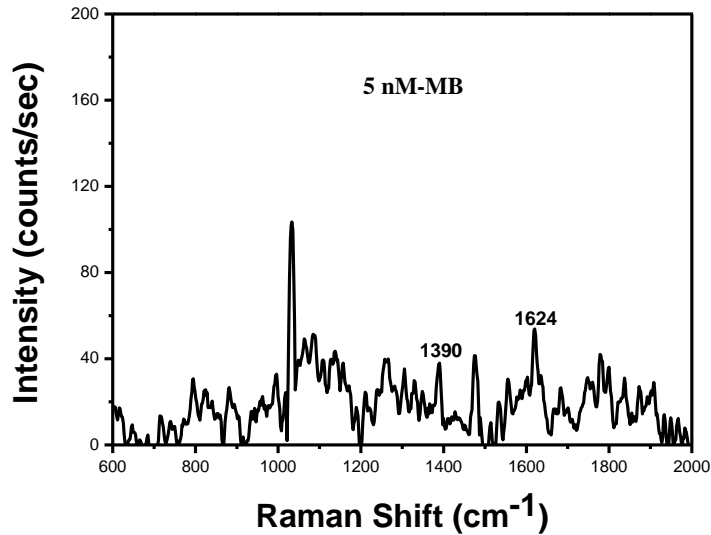


Fig.4.14: SERS spectra of MB of 5 nM by Au thin film coated on bare Si substrate

It is seen from the Fig.4.14 that the intensity of the MB peaks at 1624 cm^{-1} and 1390 cm^{-1} are very low. These experimental results indicate that a proper combination of discontinuous Au thin film coated on the nanostructured Si substrate along with Ag NPs shows better performance to detect a lower concentration of the probe (MB) material. As the lower detection of MB molecules was detected with the deposition of 10 nm discontinuous Au thin film on the nanoporous Si substrate with improved enhancement factor, few more experiments were further carried out with increasing thickness of the discontinuous Au thin films. As the lower than 5 nM MB detection was not possible with 10 nm Au thin film, four more depositions were carried out with different thicknesses of Au thin films (20 nm/30 nm/40 nm/50 nm) on the 10 nm Au coated nanostructured Si substrate. Then, subsequently the SERS measurements were carried out for detection lower concentration ($<5\text{ nM}$) of MB. Here, a particular point to be noted that the same substrate was used for all the deposition which were done one after another and then subsequently used for SERS measurements. For this purpose, before every Au deposition the substrate was dipped in HNO_3 for Ag removal and then cleaned in acetone and isopropanol with ultrasonication for 10 minutes each. In this way, each time same substrate was used and the probe material was removed for the further

SERS measurements. Before the SERS measurements, the thicknesses of the deposited thin films were measured with surface profilometer which is shown in Fig.4.15. Once, the deposition of the 20 nm discontinuous Au thin film on nanostructured Si substrate (in short **20AuSi**) was over, the same substrate was used for SERS measurement where again MB was used as the probe material but with a lesser concentration of 100 pM.

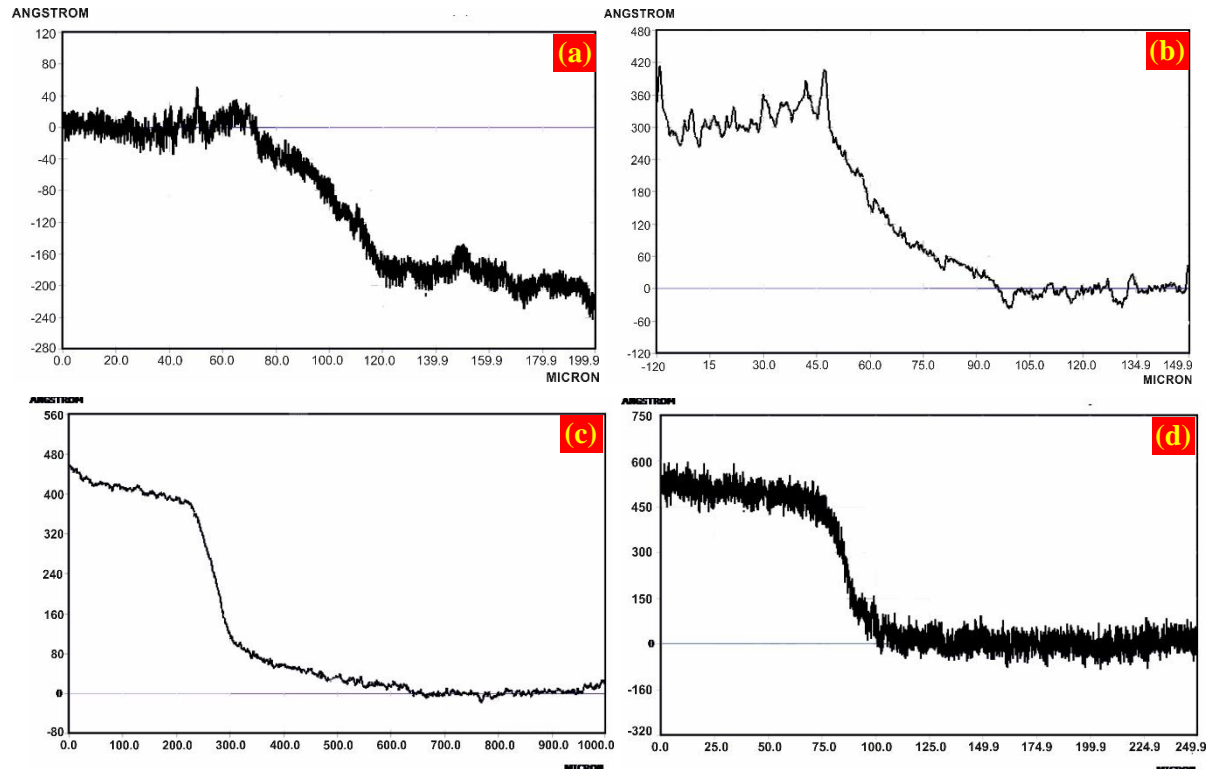


Fig.4.15: Surface profilometer reading of the deposited (a) 20 nm, (b) 30 nm, (c) 40 nm and (d) 50 nm discontinuous Au thin film on nanostructured Si substrate

Before the SERS measurement, the **20AuSi** substrate was coated with Ag NPs by drop casting. It was found that the 100 pM concentration was detected by this SERS-active substrate which is shown in Fig.4.16.

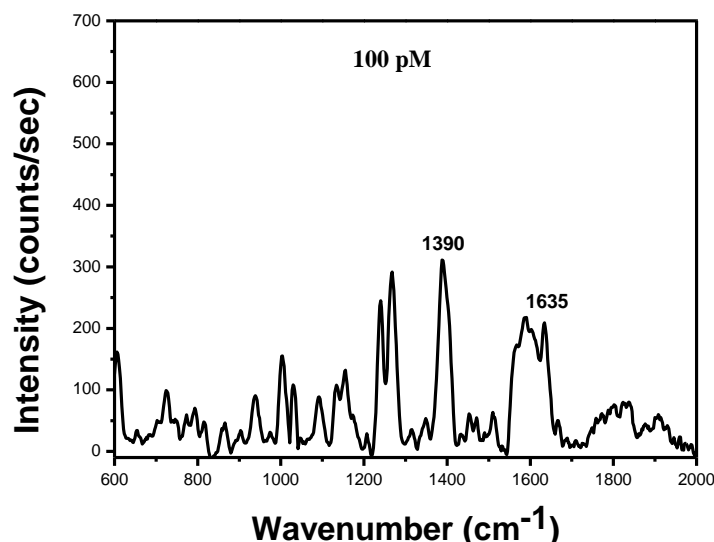


Fig.4.16: SERS spectra of MB of 100 pM by the **20AuSi** substrate

As shown in Fig.4.16, the C-C ring stretching peak shifts from 1626 cm^{-1} to 1635 cm^{-1} , whereas no shifting in peak position is observed for the C-N symmetrical stretching peak. This further shifting in the peak position possibly relates to the thickness of the Au discontinuous thin film which is increased by 10 nm. Thus, the number of metal nanoaggregates or Au islands also further increases. For this purpose, FESEM was carried out for this SERS-active substrate and is shown in Fig.4.17 which confirms the Au islands.

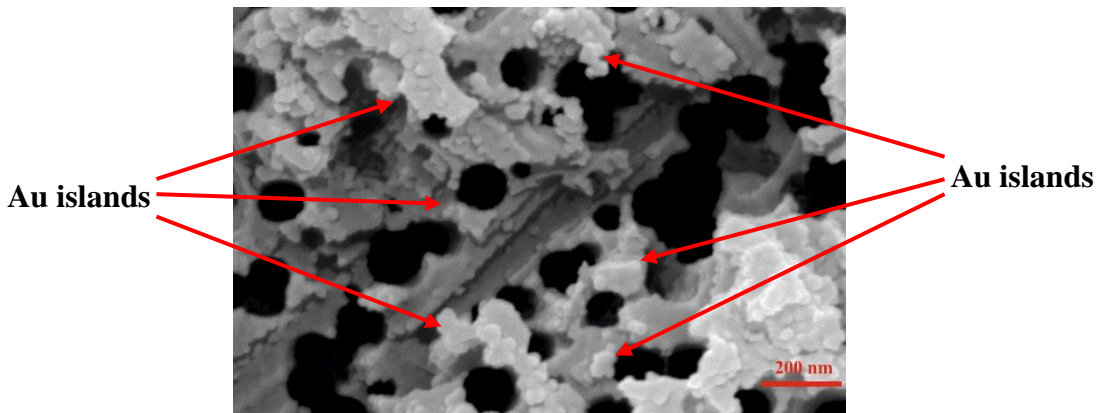


Fig.4.17: FESEM image of 20 nm Au discontinuous thin film coated on nanoporous Si substrate fabricated by Ag assisted MACE process

It has been reported earlier by Yuko S. Yamamoto [108] that variation in the metal nanoaggregates changes the shape of the SERS spectra, and same result has been also obtained from the SERS spectra collected for 100 pM MB by the **20AuSi** substrate as shown in Fig.4.16. The EF for this **20AuSi** SERS substrate is calculated as follows—

$$I_{\text{SERS}} = 213.4 \text{ counts/sec}, I_{\text{Raman}} = 3310 \text{ counts/sec}, C_{\text{HC}} = 0.1 \text{ M}, C_{\text{LC}} = 100 \text{ pM}$$

$$\therefore \text{EF} = \frac{213.4}{3310} \times \frac{0.1}{10^{-10}} = 6.4 \times 10^7$$

Later the same substrate, i.e. 20AuSi was also used for 10 pM detection of MB, but was not able to detect such a lower concentration. Thus another deposition of Au thin film (~ 10 nm) was carried out on the same substrate **20AuSi**, so as to make the total thickness 30 nm of the Au thin film deposited on the nanostructured Si substrate (Fig.4.18)

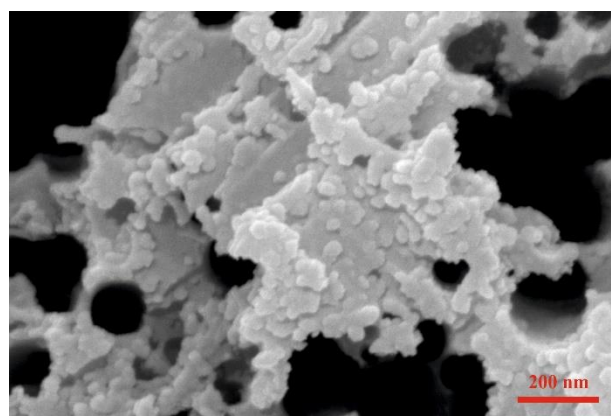


Fig.4.18: FESEM image of 30 nm Au discontinuous thin film coated on nanoporous Si substrate fabricated by Ag assisted MACE process

This new Au deposited substrate is named as **30AuSi** and it was used for the detection of 10 pM concentration of MB. The SERS spectra for using the **30AuSi** is shown in Fig.4.16. As it is seen from the plot that two characteristics peaks of MB appear at 1635 cm^{-1} and 1390 cm^{-1} which are assigned to C-C ring stretching and C-N symmetrical stretching. In this case, also the C-C ring stretching peak is found at 1635 cm^{-1} and the reason for this shifting is mentioned in the previous SERS measurement carried out with the 20AuSi substrate.

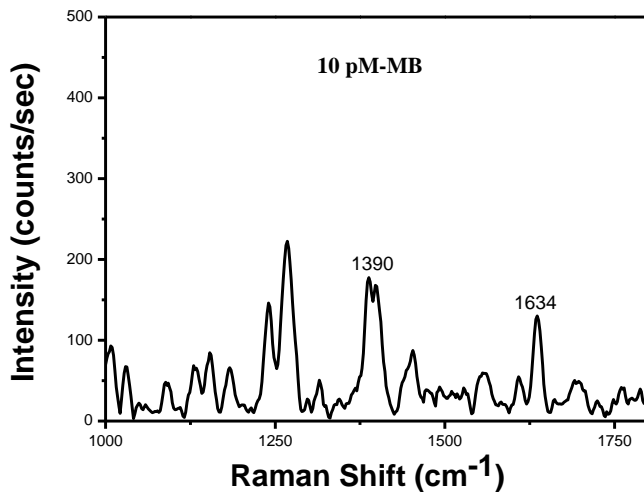


Fig.4.19: SERS spectra of MB of 10 pM by the **30AuSi** substrate

Similarly, EF for this **30AuSi** SERS substrate is calculated which is mentioned below—

$$I_{\text{SERS}} = 133.3 \text{ counts/sec}, I_{\text{Raman}} = 3310 \text{ counts/sec}, C_{\text{HC}} = 0.1 \text{ M}, C_{\text{LC}} = 10 \text{ pM}$$

$$\therefore \text{EF} = \frac{133.3}{3310} \times \frac{0.1}{10^{-11}} = 4 \times 10^8$$

Though the detection of 10 pM MB was possible with the 30AuSi substrate, due to the lower Raman signal at this concentration, no further lower concentration was tried for detection. Instead, cleaning of the substrate was done to remove the probe material as mentioned earlier. Following the cleaning process, one more deposition of Au (~ 10 nm) thin film was carried out on the **30AuSi** substrate to make the final thickness of Au thin film to 40 nm which is named as **40AuSi**. After completion of the deposition, the **40AuSi** substrate was used for the SERS measurement where 10 pM MB was used for the detection. But it was found that such a low concentration was not possible to detect. Therefore, little higher concentration, i.e. 100 pM MB solution was considered. But, in this case, also **40AuSi** substrate was not able to detect this concentration. Further to investigate SERS detection with higher Au thin film thickness, first cleaning of the **40AuSi** was carried out followed by another Au thin film of 10 nm was deposited on it to make the final of the Au thin film to 50 nm which is named as **50AuSi**. A similar result was found for this substrate where neither 10 pM nor 100 pM

solution of MB was detected. The possible reason for non-detectability of these substrates at very low concentrations may be due to the higher thickness of Au eliminates the nanoaggregates and deposited as the continuous thin film instead of Au islands as shown in Fig.4.20. Moreover, the higher thickness of Au continuous film possibly minimises the roughness which in turn reduces the SERS detection capability [109].

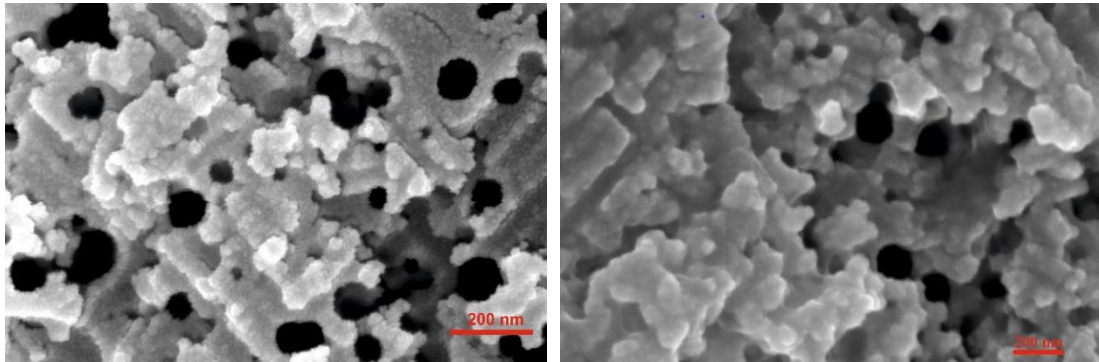


Fig.4.20 : FESEM image of (a) 40 nm Au discontinuous thin film and (b) 50 nm coated on nanoporous Si substrate fabricated by Ag assisted MACE process

Moreover, it has also been reported by J. Theiss et al. that the highest electromagnetic enhancement can be achieved for nanoparticles separated less than 2 nm from each other [110]. Therefore, when the nanoaggregates or Au islands are absent with the higher thickness of the Au thin film, the probability of residing an analyte molecule between two adjacent nanoaggregates also reduces. Due to this reason, when the number of analyte molecules decreases with the decreasing concentration, the **40AuSi** and **50AuSi** substrates were not able to detect 100 pM MB solution. So, the experimental results indicated that the nanoporous or nanostructured Si substrate, deposited with a discontinuous Au thin film 30 nm thickness could be used to detect MB at a very low concentration of 10 pM ($\sim 10^{-11}$) with higher enhancement factor (4×10^8).

4.6 Combined analysis of all the Si-based SERS-active substrates fabricated by MACE

Experimental results from SERS measurements indicated that the detection of MB as probe material depends on the thickness of the discontinuous noble metal thin film, shape and density of the nano/microstructures fabricated on the substrate. In this section, a combined analysis is discussed for the detection of MB by using different SERS substrates those were fabricated by MACE process. The SERS detections were carried out for ten different substrates such as bare Si, Ag NPs on bare Si, Ag NPs deposited on different nano/microstructured Si fabricated by MACE and Ag NPs deposited on Au thin film with

different thicknesses deposited on the nanoporous Si substrate. The details about all the process parameters, SERS measurements are mentioned in Table 4.2.

Table 4.2: Different Si micro/nanostructured substrates used for SERS measurements

Sl. No.	The process used for SERS substrate preparation	Fabricated Nano/microstructures on the Si substrate	Types of noble metal used for SERS detection	The lowest concentration used for detection	SERS detection (1390 cm^{-1} & 1621 cm^{-1})
1	Bare Si	NA	NA	50 nM	No
2	Bare Si	NA	Ag NPs coated on it	50 nM	Yes
3	20 nm Ag micro-stripes assisted MACE Si substrate	Nanopores (I)	Ag NPs coated on it	50 nM	Yes
4	20 nm Au micro-stripes assisted MACE Si substrate	Inverted pyramid structure (II)	Ag NPs coated on it	50 nM	Yes
5	20 nm Ag micro-stripes assisted MACE Si substrate	Nanopores (III)	Combination of 10 nm discontinuous Au thin film and Ag NPs coated on it	5 nM	Yes
6	20 nm Ag micro-stripes assisted MACE Si substrate	Nanopores (IV)	Combination of 20 nm discontinuous Au thin film and Ag NPs coated on it	100 pM	Yes
7	20 nm Ag micro-stripes assisted MACE Si substrate	Nanopores (V)	Combination of 30 nm discontinuous Au thin film and Ag NPs coated on it	10 pM	Yes
8	20 nm Ag micro-stripes assisted MACE Si substrate	Nanopores	Combination of 40 nm discontinuous Au thin film and Ag NPs coated on it	10 pM	No
9	20 nm Ag micro-stripes assisted MACE Si substrate	Nanopores	Combination of 50 nm discontinuous Au thin film and Ag NPs coated on it	10 pM	No

A consolidated plot is shown for all the above mentioned SERS substrates fabricated by different MACE process. In this plot, data used from all the fabricated SERS substrate by MACE process and hence the Ag NPs coated bare Si substrate's result is not included in the

plot. A number is assigned to each plot corresponding to the number assigned to each fabricated substrate mentioned in Table 4.2.

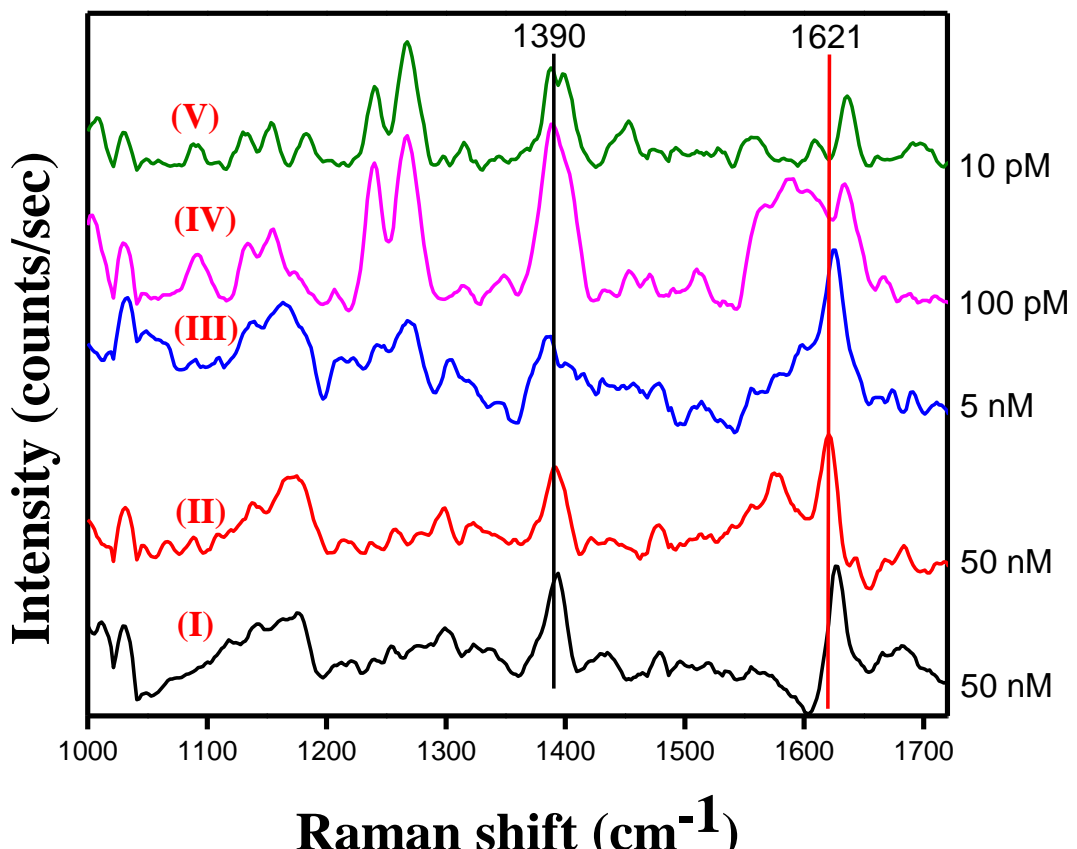


Fig.4.21: A comparative plot of SERS spectra of MB detected by different SERS substrates mentioned in Table 4.2

The final result indicates correlation between detection limit and enhancement factor of the SERS-active substrate, and offers the possibility of molecular level detection with higher enhancement factor of different chemical species by suitably preparing the SERS-active substrate.

4.7 Conclusions

SERS measurements for both nano/microstructured Si substrate fabricated by Ag and Au micro-stripes assisted MACE process coated with Ag NPs were investigated. In both the cases, up to 50 nM concentration of MB was detected, however lower than this concentration was not detectable. It was confirmed from the SERS measurement that nanoporous Si substrate showed better Raman signal than the inverted pyramid structured Si substrate for the same concentration of MB. Subsequently, few more SERS measurements were carried out to clarify the role of the nanoporous Si substrates and the Ag NPs which were used in the detection process. It was confirmed from the experimental results that by using SERS

technique, neither the nanoporous Si substrate nor the Ag NPs alone sufficient to detect the low concentration of the probe molecules (MB). The further experiments for the lower detection limit was carried out by depositing a discontinuous Au thin film on the nanoporous Si and then depositing Ag NPs. The experimental results indicated that these SERS substrates were able to detect 5 nM MB. Moreover, a 10 fold increment was achieved in the enhancement factor with this process. Thus, more experiments were carried out by increasing the thickness of the Au thin films on the nanoporous Si substrates (10 nm/20 nm/30 nm/40 nm/50 nm). The SERS measurement results on different SERS active substrates revealed that by increasing the Au discontinuous thin film thickness, 10 pM MB could be successfully detectable where a combination of 30 nm Au discontinuous thin film and Ag NPs were deposited on nanoporous Si substrate. However, further increasing the Au thin film thickness to 40 nm or 50 nm, no detection was obtained even at a lower concentration of MB (10 pM or 100 pM). Hence, nanoporous Si substrate as fabricated by using the 20 nm Ag micro-stripes based MACE process, with 30 nm discontinuous Au thin film deposited on the top along with the Ag NPs could be the best choice to prepare the SERS substrate to detect lower limit MB (10 pM).

CHAPTER 5

Applications of Si nanopores based substrates for SERS detection of chemical species (MB)

5.1 Introduction

The SERS measurements, as discussed in the previous chapter, it was seen that the nanoporous Si substrate showed better improvements in Raman signal than the Si substrate consist of inverted pyramidal structures. Previously, the nanoporous Si substrates were prepared by MACE process where 20 nm Ag thin film with micron-scale coverage was used as catalyst. Therefore, directly nanoporous Si substrates were prepared by choosing the Ag NPs as metal catalyst instead of using 20 nm Ag micro-stripe as catalyst and the influence of this way of preparation of the SERS-active substrate on the detection limit and enhancement factor for detection of MB by SERS technique are discussed in this chapter.

5.2 Deposition of Ag NPs on Si substrate and its characterisation

The silver NPs were purchased from Sigma Aldrich, USA which act as metal catalyst for nanopores formation in the Si (100) substrate. In the typical experiment, p-Si (100) substrate (resistivity 1-10 $\Omega\text{.cm}$) was used and cut into 1cm \times 1cm size by using a diamond scriber. All the cut pieces of Si samples were cleaned in the same way which is explained in chapter 2. In next step, the MACE was performed in two steps, firstly, uniform deposition of Ag nanoparticles on the Si substrate and secondly, chemical etching of the Si by using the as-deposited Ag nanoparticles as metal catalyst in the presence of the etching solution. For this purpose, commercially procured Ag NPs were dispersed in isopropanol (IPA) with the concentration of 0.004 Vol % and subsequently dispersed Ag nanoparticles in IPA were coated on the cleaned p-Si (100) substrate. For deposition purpose, two deposition processes were used such as dip coating and spin coating to find the impacts of these two different processes on the size distribution and nanopores formation in Si. The parameters used for a dip and spin coating processes are listed in Table 5.1.

Table 5.1: Details about the coating parameters of dip and spin coating

Sl. No.	Coating Parameters	Dip Coating	Spin Coating	
1	Concentration of Ag NPs dispersion	0.004 w/v%	0.004 w/v %	
2	Coating Time (in seconds)	10	Step 1 @200 rpm	Step 2 @700 rpm
			10	30

5.3 Characterizations of the commercially available Ag NPs

The shape and size of the commercially available Ag NPs were characterised by using Tecnai transmission electron microscope (TEM). Similarly, the elemental composition of the NPs was characterised by using energy dispersive X-ray spectroscopy (EDS) manufactured by Oxford Instruments. X-ray diffraction (XRD) analysis was carried out by using Bruker D8 Advance X-ray diffractometer to confirm the NPs as silver and to get the structural information of these particles. The morphology of the Ag NPs, which were coated on p-Si(100) substrates by dip coating and spin coating was characterised by CARL ZEISS field emission scanning electron microscope (FESEM). Similarly, the surface topography of the p-Si (100) substrates after Ag NPs assisted MACE was done by using FESEM. Figure 5.1(a-c) depicts the XRD, analysis of the Ag NPs. As shown in Fig. 5.1, five peaks appear at $2\theta = 38.50, 44.60, 64.30, 77.50, 81.80$ and indexed as (111), (200), (220), (311), (222) planes, respectively. By comparing JCPDS (file no: 04-0783), the typical pattern of Ag NPs is found to comprise an fcc structure (with lattice parameter $a=b=c= 2.13 \text{ \AA}$)

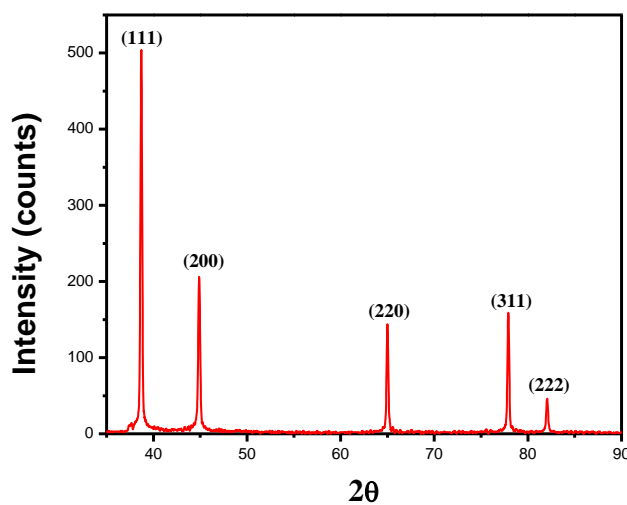


Fig.5.1: XRD pattern of Ag NPs

The size and shape of the Ag NPs were analysed by TEM (Fig.5.2 a). Similarly, in Fig.5.2 (b), an EDX spectrum of these particles is shown. In this quantitative analysis, a typical and strong signal peak was found at 3 keV, which corresponds to metallic Ag NPs.

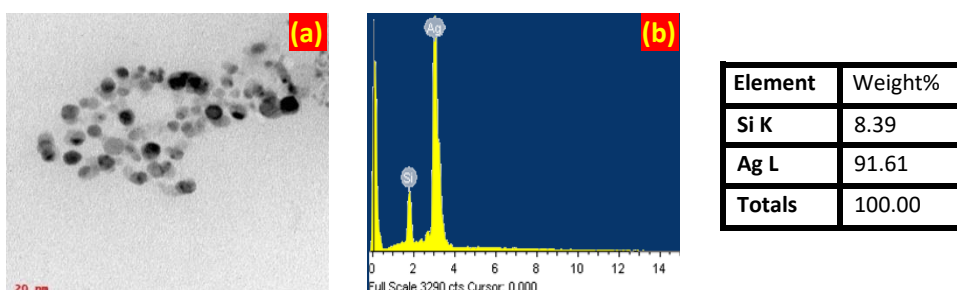


Fig. 5.2: (a) TEM and (b) EDX of the commercial Ag NPs

The corresponding atomic percentages are shown in Table 5.2. The particle size was calculated by using ImageJ software, and the average size is found to be about 33 nm as shown in Fig.5.3. The average NP's size is calculated based on the values XC and W acquired from the curve fitting.

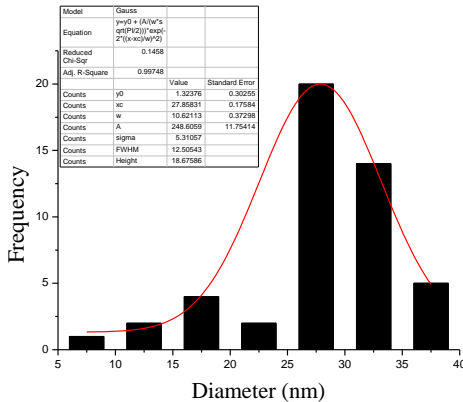


Fig.5.3: Size distribution analysis of Ag NPs

$$XC=27.9, W=10.6$$

$$\therefore \text{standard deviation } (\sigma) = W/2 = 10.6/2 = 5.3$$

$$\therefore \text{average NPs size} = (27.9+5.3) = 33.2 \sim 33 \text{ nm}$$

The Ag NPs were used in MACE of p-Si (100) substrate by depositing two different techniques such as dip coating and spin coating, and the distribution of these particles was characterised by FESEM which is shown in Fig.5.4(a-d). Comparing both deposition techniques, dip coating method showed the better distribution of the NPs than the spin coating method on p-Si (100) substrate with 0.004 w/v% of initial concentration of the solution for both the deposition process. The possible reason for non-uniformity in Ag NPs distribution over Si substrate resulted from the spin coating process is the low initial concentration of the solution.

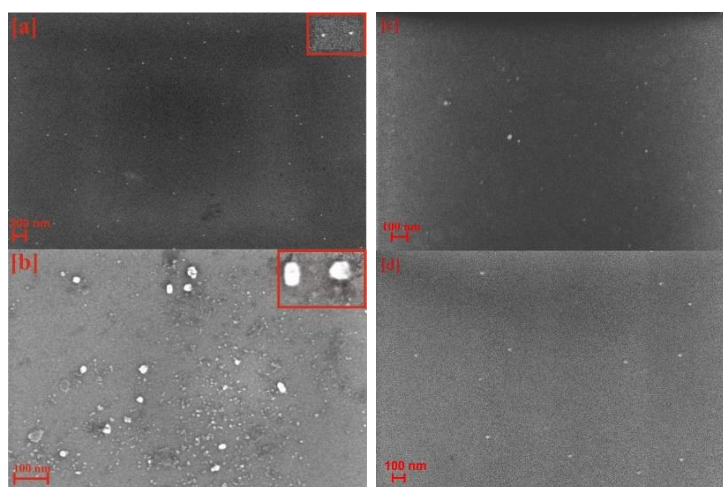


Fig. 5.4: FESEM images of Ag nanoparticles coated on p-Si (100) substrate by (a,c) dip coating and (b,d) spin coating method

It is already reported that the thinning of a film in the spin coating process depends upon two consecutive mechanisms such as convective radial outflow and the solvent evaporation [111]. Similarly, in our spin coating deposition process, two steps with different rotation per minute (rpm) values were used to deposit the Ag NPs. In the first step of the spin coating process, the convective outflow and solvent evaporation play the main role in the distribution of the NPs throughout the substrate. Likewise, as the concentration of the solution is very low and the solvent is in use is also volatile (IPA), henceforth during the first step of the spin coating process, solution viscosity increases with the increase of solution concentration. Due to this increment in the viscosity of the solution and the convective radial outflow encompasses centrifugal force which distributes the NPs throughout the substrate non-uniformly which can be attributed to Fig. 5.4 (b,d). In the dip coating method, solvent evaporation and draining play major roles in the thinning of the film [110]. Unlike the spin coating method where centrifugal force is applied in the solution, here in dip coating method such force is absent.

5.4 MACE of Si by using Ag NPs deposited by dip and spin coating process

Then MACE of p-Si was carried out with two samples, one dip, and spin-coated Ag NPs with the same parameters as mentioned earlier. Then, the morphology of these substrates was examined under an electron microscope which is depicted in Fig.5.5 (a,c) and 5.5 (b,d). Fig.5.5 (a,c) show the nanopores distribution on the p-Si substrate after MACE was performed by dip coated Ag NPs. Whereas, Fig.5.5 (b,d) shows the nanopore on the Si by using the spin-coated Ag NPs as a catalyst in the MACE process.

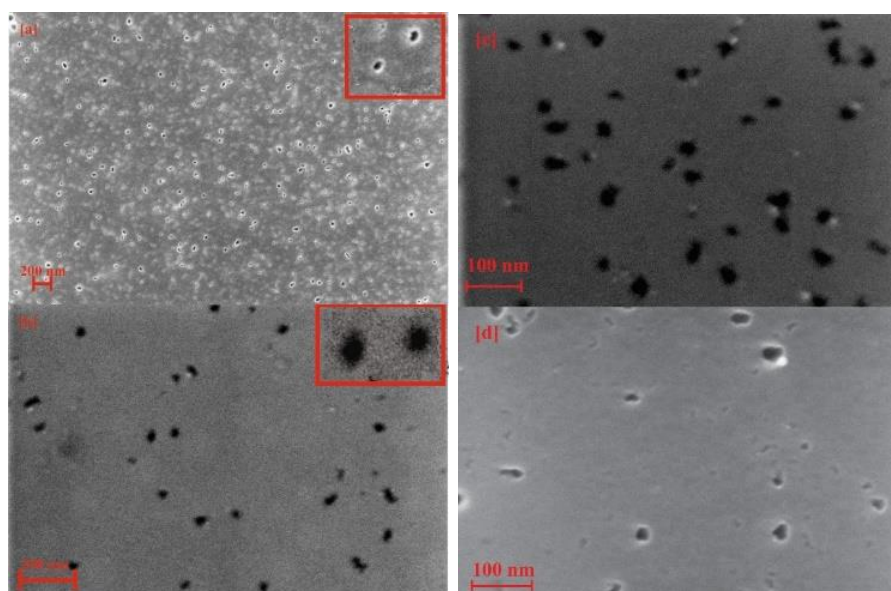


Fig.5.5: FESEM image of p-Si (100) substrate after MACE by (a,c) dip coated and (b,d) spin coated Ag nanoparticles

Comparing the nanopores formation during the MACE of Si by both dip and spin-coated Ag NPs, it is confirmed the nanopores are uniformly and with equal dimension formed with dip coated Ag NPs as compared to the spin-coated process. It has been reported by the Brendan D. Smith et al. [74] that not all the deposited NPs on the Si take part in the etching process for shorter etching time. This problem occurs mainly due to the presence of the SiO_2 shell thickness which promotes the non-uniform hole injection into the Si substrate. As our process does not involve these, all the NPs deposited on the Si substrate possibly take part in the etching process which can be attributed to Fig.5.5. Similarly, Fig. 5.6 (a) and 5.6 (b) show the nanopores size distribution on the p-Si substrate after MACE by dip and spin-coated Ag NPs respectively.

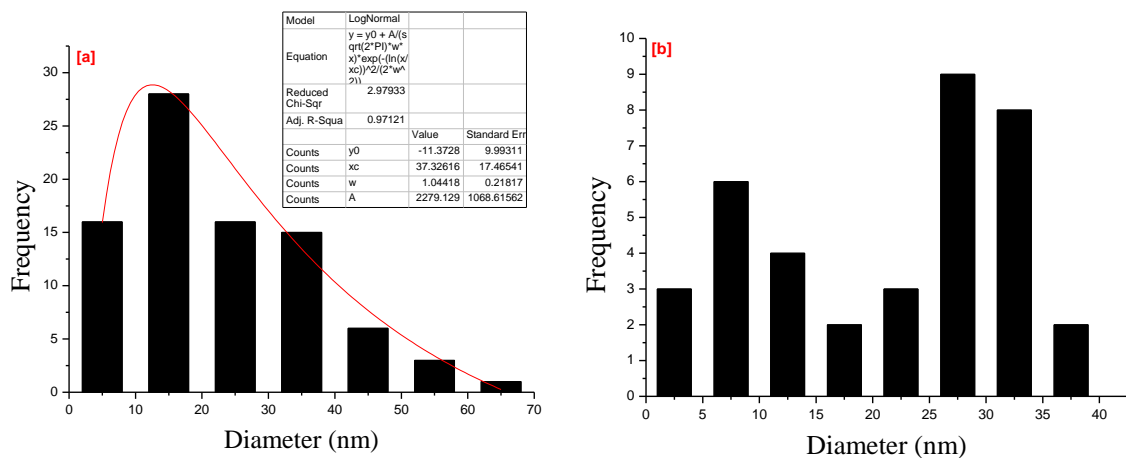


Figure 5.6. Size distribution of nanopores formed on p-Si (100) substrate after MACE by (a) dip coated Ag NPs (b) Spin coated Ag NPs

It is seen from Fig.5.6a and 5.6b that after the MACE process, the nanopores with uniform size and shape (Fig.5.6a) are formed with dip coated than the spin-coated Ag NPs (Fig.5.6b). The average nanopore size formed during MACE with dip coated Ag NPs is

$$XC=37.3, W=1.04$$

$$\therefore \text{standard deviation } (\sigma) = W/2 = 1.04/2 = 0.52 \sim 0.5$$

$$\therefore \text{average nanopore size} = (37.3+0.5) = 37.8 \sim 38 \text{ nm (eq.2)}$$

It is found that the diameter of the nanopores formed by dip coated Ag NPs are little larger (~15%) than the size of the NP's diameter. This resembles the same results reported by C. Chartier et al. [25]. In contrast, the size of the nanopores formed by spin-coated Ag NPs varies non-uniformly, and the density of the nanopores formed is less compared to dip coated Ag NPs. By using any one of this method, nanopores with tens of centimetre coverage on Si substrate are possible to form with ease. Moreover, the difficulty associated with the uniform size distribution of the NPs formed during the one-step MACE process (e.g. by using AgNO_3

as precursor solution) can be controlled more effectively to obtain the non-uniform nanopores formation on Si substrates. In this study, it is seen that the nanopores formed by MACE process resemble the same size and shape of the NPs used in the process. So, by controlling the size and shape of the metal NPs during the synthesis process, it is possible to fabricate uniform nanopores on Si substrate by MACE process. Further research can be carried out on different NPs deposition techniques and how these techniques influence in nanopores formation by MACE process. After the nanopores formation on the Si substrates, both the substrates were used for SERS measurement which is discussed in the next section.

5.5 SERS measurement by nanoporous Si substrates fabricated by Ag NPs assisted MACE process

The SERS measurements were carried out for both the nanoporous Si substrate fabricated by dip coated (here onwards **SD1**) and spin coated (**SS1**) Ag NPs assisted MACE process. Before the SERS measurements, Ag NPs were drop cast on the surface of the nanoporous substrate. Then, these two samples were analysed by the same portable Raman spectrometer which details are mentioned earlier (Chapter 4). Initially, both the substrates were used to detect MB of lower concentrations such as 10 pM, 100 pM and 5 nM respectively. But, no Raman signal was obtained to detect such lower concentrations. So, a higher concentration of 50 nM MB was used for SERS measurements by using the same substrates. In this case, the **SS1** substrate was unsuccessful to detect the MB whereas the **SD1** substrate was able to detect that concentration which is shown in Fig.5.7. It is seen from the Raman spectra that the two characteristics peaks of MB appear at 1620 cm^{-1} and 1390 cm^{-1} , those are assigned to C-C ring stretching and C-N symmetrical stretching. As the detection of the methylene blue was successful, the efficiency of these substrates was measured by calculating enhancement factor and the details about the calculations are mentioned in the next page.

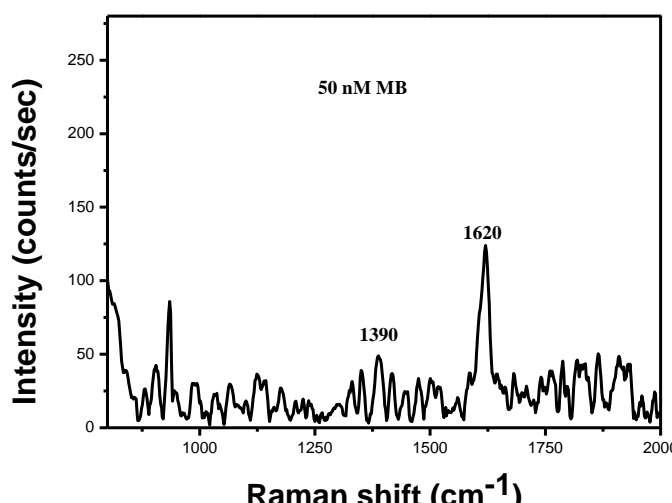


Fig.5.7: SERS spectra of MB of 50 nM detected by Ag NPs coated nanostructured Si substrate produced by dip-coated Ag NPs assisted MACE process 94

EF for this SERS substrate is calculated which is mentioned below—

$$I_{\text{SERS}} = 125.1 \text{ counts/sec}, I_{\text{Raman}} = 3310 \text{ counts/sec}, C_{\text{HC}} = 0.1 \text{ M}, C_{\text{LC}} = 50 \text{ nM}$$

$$\therefore \text{EF} = \frac{125.1}{3310} \times \frac{0.1}{50 \times 10^{-9}} = 7.6 \times 10^4$$

By comparing the result of the SERS signal by the substrate **AgSiM** and **SD1** substrate, it is found that the SD1 substrate showed lesser detection and the enhancement is 10 times lower.

5.6 Conclusions

The influence of the deposition process of Ag nanoparticles on the Si substrate for nanopores formation has been found to be an important parameter in MACE of Si substrate. The diameter of the nanopores formed by MACE process is little larger than the NPs diameter. It is found that in case of dip-coated Ag NPs assisted MACE; nanopores are formed uniformly throughout the Si surface. The spin-coated Ag NPs formed nanopores which are non-uniform in size with uneven distribution. Moreover, the density of nanopores formed during the MACE process with spin-coated Ag NPs is lower than the dip coated Ag NPs assisted MACE process. After the nanopores formation on the Si substrate by Ag NPs assisted MACE process, both the substrates **SS1** and **SD1** were used for SERS measurements and confirmed that the **SD1** can be used for SERS measurement to detect 50nm MB. However, the Raman signal is not that much strong as compared to the samples discussed earlier (Chapter 4). Further studies can be carried out to improve the detection limit of these reusable substrates as it does not require any sophisticated instruments and also can be fabricated easily.

CHAPTER 6

Summary and Conclusions

The first part of this thesis work deals with the fabrication of the Au and Ag micro-stripes on Si substrates by incorporating lithography, thin film deposition followed by a lift-off process. For this purpose, Au and Ag thin films were successfully deposited on Si substrates by two different ways such as RF sputtering and thermal evaporation processes, those acted as the metal catalyst for the MACE process. 20 nm thick Au and Ag micro-stripes of length 2500 μm and width about 3.3 μm were fabricated on the Si substrate by using the thermal evaporation process to understand the effect of a different metal catalyst on MACE of Si. Furthermore, a few more depositions were also carried out by changing the source to target distance during the thermal evaporation, to obtain different growth morphology based Au metal catalysts. Later, these metal catalysts were used to etch Si by MACE process. In all the cases, the thickness of the micro-stripes was kept about 20 nm which were confirmed from the profilometer analysis results. MACE was carried out by using these Au and Ag micro-stripes as a metal catalyst with 20 nm thickness and also with higher thicknesses such as 40 nm and 140 nm, to study of thickness effect of the Au metal catalyst on the MACE of Si.

The experimental results indicated that the presence of nanopores in the Au micro-stripes form a rough surface at the bottom of the micro-trench fabricated on the Si substrate along with the random distribution of the nanopores at the bottom of the trench. Similar results were also found when Ag micro-stripes were used as a metal catalyst for the MACE process. Also, it was found that the unwanted nanopores were distributed all over the substrates when Ag metal micro-stripes acted as a metal catalyst for the MACE process. This was possibly due to the dissolution of Ag catalyst during the etching of Si and redeposited in different parts of the substrates. Further studies on the MACE process also indicated that thermal annealing of the metal catalyst before the MACE process helped to reduce the nanopores at the bottom of the micro-trench and opened a new path for the fabrication of smooth microstructures in Si substrate by MACE process.

Furthermore, the effect of post-deposition thermal annealing of the micro-stripes catalyst on MACE of Si was also investigated by the Au micro-stripes fabricated by using the thin films deposited by RF sputtering process with 20 nm, 50 nm and 140 nm thick metal micro-stripes as a catalyst. The first MACE of Si was carried out by using 20 nm annealed and un-annealed thin Au micro-stripes and the FESEM results revealed that annealed micro-stripes formed smoother and deeper trenches than the un-annealed one. The obtained results further indicated that the nano-pinholes were not present in the micro stripes after thermal annealing process. A similar result was also obtained when the annealed and un-annealed 20 nm Au

micro-stripes fabricated by using the Au thin film deposited by thermal evaporation. Further investigations were also carried out by using 50 nm and 140 nm Au micro-stripes as a catalyst and the obtained results indicated that the annealed Au micro-stripes with higher thickness etch Si uniformly in comparison to the annealed Au stripes with lower thickness. The possible reason for obtained results is discussed in the thesis. In brief, because of the absence of the nanopores, etching happened at the edges of the Au stripes where Au-Si interface was present. Furthermore, with the increase of the concentration of oxidising agent, uniform Si etching was not obtained. Instead, a combination of polishing regions and craters were formed in the Si substrate.

Further studies were also carried out to investigate the growth morphology of the metal catalyst on the MACE of Si. For this purpose, 20 nm thick Au micro-stripes were fabricated from the thin film deposited by thermal evaporation process and by changing the source to target distance. The different Au thin film morphologies were confirmed from the FESEM and AFM analysis results. The experimental results indicated different etch profiles formed in the Si substrate which signifies the morphological dependency of the catalyst on MACE of Si. In the case of Au micro stripes fabricated from the thin film deposited with the shortest source to substrate distance, uniform etching occurred and etched micro-trenches with the smoother bottom surface in all the areas underneath the metal micro-stripes catalyst. But in the case of Au micro-stripes fabricated from the thin film deposited with the longest source to substrate distance, different growth morphology, inverted pyramid structures are obtained at the edges of the micro-stripes. The Si microstructures those were fabricated by using the 20nm thick, Ag metal micro-stripes and 20nm thick Au-micro-stripes as a catalyst were considered further to apply as SERS substrates for chemical detection.

In the next part of this thesis work, SERS measurements were carried out to detect MB having different concentration starting from 50 nM to 10 pM. SERS measurements for both the nano/microstructured Si substrate fabricated by Ag and Au micro-stripes assisted MACE process coated with Ag NPs were investigated. In both the cases, up to 50 nM concentration of MB was detected and lower than this concentration was not detectable. It was confirmed by the SERS measurement that nanoporous Si substrate showed better Raman signal than the inverted pyramid structured Si substrate for the same concentration of MB. Subsequently, few more SERS measurements were carried out to clarify the role of the nanoporous Si substrates and the Ag NPs which were used in the detection process. It was confirmed that neither the nanoporous Si substrate nor the Ag NPs alone detects the low concentration (pM)

of the probe molecules (MB) by using SERS. The further optimisation for the lower detection limit was carried out by depositing a discontinuous Au thin film on the nanoporous Si followed by depositing Ag NPs for the SERS measurement. These SERS substrates were able to detect 5 nM MB. Moreover, a 10 fold increment was achieved in the enhancement factor with this optimisation. Thus, further investigations were carried out by increasing the thickness of the Au thin films on the nanoporous Si substrates. In this way, 10 nm, 20 nm, 30 nm, 40 nm and 50 nm Au thin films were deposited on the nanoporous Si substrate which was fabricated by 20 nm Ag micro-stripe as catalyst. The SERS measurement results on different SERS active substrates revealed that by increasing the Au discontinuous thin film thickness, 10 pM MB could be successfully detectable at 30 nm Au discontinuous thin film on nanoporous Si substrate. However, further increasing the Au thin film thickness to 40 nm or 50 nm, no improvements in the detection limit was obtained at a lower concentration of MB (10 pM or 100 pM). Hence, nanoporous Si substrate which was fabricated by using the 20 nm Ag micro-stripes based MACE process, with 30 nm discontinuous Au thin film deposited on the top along with the Ag NPs could be the best choice to prepare the SERS substrate to detect lower limit MB (10 pM) with larger enhancement factor.

In another study, instead of taking Ag micro-stripes, Ag NPs were directly used as a catalyst for the Si chemical etching by MACE process. For this purpose, procured Ag NPs with approximately 33 nm diameter were deposited on the Si substrate and subsequently MACE was carried out. It is found that in case of dip-coated Ag NPs assisted MACE; nanopores are formed uniformly throughout the Si surface. The spin-coated Ag NPs formed nanopores which are non-uniform in size with uneven distribution. Moreover, the density of nanopores formed during the MACE process with spin-coated Ag NPs is lower than the dip coated Ag NPs assisted MACE process. After the nanopores formation on the Si substrates by Ag NPs assisted MACE process, these were used for SERS measurements. The results indicated that 50 nM MB could be detected but the Raman signal was not that much strong as compared to the samples discussed earlier (Chapter 4). Further studies can be carried out to improve the detection limit of these reusable substrates as it does not require any sophisticated instruments and also can be fabricated easily.

In summary, the lowest detection limit of 10 pM with an enhancement factor of 10^8 was achieved by depositing 30 nm thick discontinuous Au thin film on the MACE Si prepared by 20 nm Ag micro-stripes. This lowest detection limit further indicated that the fabrication of SERS based sensor with ultrahigh sensitivity is possible and also without any further

modification of the surface. Forming nanoporous structures on the surface of the Si substrate helps to get rid of the “diffusion limit”. Thus our results showed that pM concentration of MB could be detected with an enhancement in the enhancement factor up to 10^8 .

Conclusions and future prospects

The outcome of this thesis work indicates that the different nano/microstructures fabricated on the Si substrate strongly influences the SERS detection limit and also the enhancement factor. So, there is a future scope to prepare Si-based SERS-active substrate by fabricating different nano/microstructures or the combination of both by suing MACE process. It was also observed that the combination of discontinuous Au thin film and Ag NPs showed highest detection limit and hence there is another scope to use different sizes of the Ag NPs with a combination of Ag or Au thin discontinuous film for the detection of different Raman active chemical species. Despite the SERS measurements were carried out to detect a single probe material alone, there is a need to verify the ability of the fabricated Si-based SERS substrates in detecting a mixture of two or more probe materials at a time. We believe that our experimental findings will be more helpful to develop more efficient SERS-active substrates for the detection of chemical species at molecular level.

CHAPTER 7

References

- [1] Hee Hana, Zhipeng Huang, Woo Lee, *Nano Today*, 9, 271—304 (2014).
- [2] Yousong Liu, Guangbin Ji, Junyi Wang, Xuanqi Liang, Zewen Zuo and Yi Shi, *Nanoscale Research Letters*, 7:663 (2012).
- [3] S. A. Kara, A. Keffous, A. M. Giovannozzi, A. M. Rossi, E. Cara, L. D'Ortenzi, K. Sparnacci, L. Boarino, N. Gabouze and S. Soukane, *RSC Adv.*, 6, 93649 (2016).
- [4] Bi-Shen Lee, Pi-Chen Lin, Ding-Zheng Lin & Ta-JenYen, *Sci. Rep.* 8:516 (2018).
- [5] D. Kumar, S. K. Srivastava, P. K. Singh, K. N. Sood, V. N. Singh, N. Dilawar and M. Husain, *J. Nanopart. Res.*, 12, 2267–2276 (2010).
- [6] P. Singh, S. K. Srivastava, M. Yameen, B. Sivaiah, V. Prajapati, P. Prathap, S. Laxmi, B. P. Singh, Vandana, C. M. S. Rauthan and P. K. Singh, *J. Mater. Sci.*, 50, 20, 6631–6641 (2015).
- [7] S. K. Srivastava, D. Kumar, S. W. Schmitt, K. N. Sood, S. H. Christiansen and P. K. Singh, *Nanotechnology*, 25, 175601 (2014).
- [8] Hee Han, Zhipeng Huang, Woo Lee, *Nano Today* 9, 271—304 (2014).
- [9] Z. Huang, T. Shimizu, S. Senz, Z. Zhang, X. Zhang, W. Lee, et al., *Nano Lett.*, 9, 7 2519–2525 (2009).
- [10] H. Fang, X. Li, S. Song, Y. Xu and J. Zhu, *Nanotechnology*, 19, 255703 (2008).
- [11] Y. Cui, Q. Wei, H. Park and C. M. Lieber, *Science*, 293, 1289 (2001).
- [12] F. Patolsky, G. Zheng and C. M. Lieber, *Nat. Protoc.*, 1, 1711-1724 (2006).
- [13] Y. Cui and M. Lieber, *Science*, 291, 851 (2001).
- [14] L. J. Chen, *J. Mater. Chem.*, 17, 4639 (2007).
- [15] Albella P, Poyli M A, Schmidt M K, Maier S A, Moreno F, Saenz J J and Aizpurua J, *J. Phys. Chem., C* 117 13573–13584 (2013).
- [16] Fu Y H, Kuznetsov A I, Miroshnichenko A E, Yu Y F and Luk'yanchuk, *Nat. Commun.*, 4, 1527 (2013).
- [17] K. Q. Peng, Y.J. Yan, S.P. Gao, J. Zhu, *Adv. Mater.* 14 (2002)1164—1167. K.Q. Peng, Y.J. Yan, S.P. Gao, J. Zhu, *Adv. Funct. Mater.* 13 (2003).
- [18] Li X, Bohn PW. Metal-assisted chemical etching in HF/H₂O₂ produces porous silicon. *Appl Phys Lett.*, 77, 16, 2572 (2000).
- [19] Li X, Kim Y-W, Bohn PW, Adesida I. In-plane bandgap control in porous GaN through electroless wet chemical etching. *Appl Phys Lett.*, 80, 6, 980 (2002).
- [20] Zhipeng Huang , Nadine Geyer , Peter Werner , Johannes de Boor , and Ulrich Gösele, *Adv. Mater.*, 23, 285-308 (2011).
- [21] S. Chattopadhyay, X. L. Li, P. W. Bohn, *J. App. Phys.* 91, 6134 (2002).

- [22] Prayudi Lianto, Sihang Yu, Jiaxin Wu, C. V. Thompson and W. K. Choi, *Nanoscale*, 4, 7532 (2012).
- [23] H. J. Kim, I. C. Bang and J. Onoe, *Opt. Laser. Eng.*, 47, 532–538 (2009).
- [24] http://www51.honeywell.com/sm/hfacid/common/documents/HF_properties_and_graphs.pdf, 2002.
- [25] C. Chartier, S. Bastide, C. Levy-Clement, *Electrochimica Acta*, 53, 5509–5516 (2008).
- [26] M. Fleischmann, P. J. Hendra and A. J. McQuillan, *Chem.Phys. Lett.*, 26, 163–166 (1974).
- [27] D. L. Jeanmaire and R. P. Van Duyne, *J. Electroanal. Chem. Interfacial Electrochem.*, 84, 1–20 (1977).
- [28] M. G. Albrecht and J. A. Creighton, *J. Am. Chem. Soc.*, 99, 5215–5217 (1977).
- [29] K. Kneipp, Y. Wang, H. Kneipp, L. T. Perelman, I. Itzkan, R. R. Dasari and M. S. Feld, *Phys. Rev. Lett.*, 78, 1667–1670 (1997).
- [30] S. S. R. Dasary, A. K. Singh, D. Senapati, H. Yu and P. C. Ray, *J. Am. Chem. Soc.*, 131, 13806–13812 (2009).
- [31] J. F. Li, Y. F. Huang, Y. Ding, Z. L. Yang, S. B. Li, X. S. Zhou, F. R. Fan, W. Zhang, Z. Y. Zhou, Y. WuDe, B. Ren, Z. L. Wang and Z. Q. Tian, *Nature*, 464, 392–395 (2010).
- [32] Y. He, S. Su, T. Xu, Y. Zhong, J. A. Zapien, J. Li, C. Fan and S.-T. Lee, *Nano Today*, 6, 122–130 (2011).
- [33] A. Chou, E. Jaatinen, R. Buiidas, G. Seniutinas, S. Juodkazis, E. L. Izake and P. M. Fredericks, *Nanoscale*, 4, 7419–7424 (2012).
- [34] V. K. K. Upadhyayula, *Anal. Chim. Acta*, 715, 1–18 (2012).
- [35] Giner-Casares, J. J.; Liz-Marzán, L. M. *Nano Today*, 9, 365–377 (2014).
- [36] Luo, S.-C., Sivashanmugan, K., Liao, J.-D., Yao, C.-K., Peng, H.-C., *Biosens. Bioelectron.*, 61, 232–240 (2014).
- [37] Wang, Y., Irudayaraj, J. *Philos., Trans. R. Soc. B Biol. Sci.*, 368, 20120026 (2012).
- [38] Harmsen, S. Huang R., Wall, M. A. Karabeber, H. Samii, J. M. Spaliviero M., White J. R. Monette S., O'Connor R., Pitter, K. L., Stephen A. Sastra, Michael Saborowski, Eric C. Holland, Samuel Singer, Kenneth P. Olive, Scott W. Lowe, Ronald G. Blasberg, Moritz F. Kircher, *Sci. Transl. Med.*, 7, 271ra7 (2015).
- [39] D. L. Jeanmaire and R. P. Van Duyne, *J. Electroanal. Chem. Interfacial Electrochem.*, 84, 1–20 (1977).
- [40] A. Otto, J. Billmann, J. Eickmans, U. Erturk and C. Pettenkofer, *Sur. Sci.*, 138, 319-338 (1984).

- [41] T. E. Furtak, J. Reyes, *Surf. Sc.*, 93, 351-382 (1980).
- [42] E. Burstein, Y. J. Chen, C. Y. Chen, S. Lundquist, and E. Tosatti, *Sol. Stat. Comm.*, 29, 567-570 (1979).
- [43] Hongxing Xu, Javier Aizpurua, Mikael Kall, and Peter Apell, *Physic Rev E*, 62, 3, 4318-4324 (2000).
- [44] Hongxing Xu and Mikael Kall, *ChemPhyChem*, 4, 1001-1005 (2003).
- [45] Martin Moskovits, *J. Raman Spectrosc.*, 36, 485-496 (2005).
- [46] J. Mullin, N. Valley, M. G. Blaber, G. C. Schatz, *J. Phys. Chem. A*, 116, 1931-1938 (2012).
- [47] K. Balasundaram, J. S. Sadhu, J. C. Shin, B. Azeredo, D. Chanda, M. Malik, K. Hsu, J. A. Rogers, P. Ferreira and S. Sinha, *Nanotechnology*, 23, 305304 (2012).
- [48] W. Xia, J. Zhu, H. Wang, X. Zheng, *CrystEnggChem*, 16, 4289-4297 (2014).
- [49] Kazuya Tsujino and Michio Matsumura, *Electrochemical and Solid-State Letters*, 8, C193-C195 (2005).
- [50] Kuiqing Peng, Juejun Hu, Yunjie Yan, Yin Wu, Hui Fang, Ying Xu, Shuit Tong Lee, and Jing Zhu, *Adv. Funct. Mater.*, 16, 387–394 (2006).
- [51] J. D. Holmes, K. P. Johnston, R. C. Doty, B. A. Korgel, *Science*, 287, 1471 (2000).
- [52] Kuiqing Peng, Yin Wu, Hui Fang, Xiaoyan Zhong, Ying Xu, and Jing Zhu, *Angew. Chem. Int. Ed.*, 44, 2737 –2742 (2005).
- [53] K. Peng, A. Lu, R. Zhang, and S. T. Lee, *Adv. Funct. Mater.*, 18, 3026–3035 (2008).
- [54] H. Fang, Y. Wu, J. H. Zhao, J. Zhu, *Nanotechnology*, 17, 3768 (2006).
- [55] Z. P. Huang, H. Fang, J. Zhu, *Adv. Mater.*, 19, 744-748 (2007).
- [56] K. Q. Peng, M. L. Zhang, A. J. Lu, N. B. Wong, R. Q. Zhang, S. T. Lee, *Appl. Phys. Lett.*, 90, 163 123 (2007).
- [57] Owen James Hildreth, Wei Lin, and Ching Ping Wong, *ACS Nano*, 3, 4033–4042 (2009).
- [58] Yongquan Qu, Lei Liao, Yujing Li, Hua Zhang, Yu Huang, and Xiangfeng Duan, *Nano Lett.*, 9, 12, 4539-4543 (2009).
- [59] Ciro Chiappini, Xuewu Liu, Jean Raymond Fakhoury, and Mauro Ferrari, *Adv. Funct. Mater.*, 20, 2231–2239 (2010).
- [60] Manel Abouda-Lachiheb, Nesma Nafie and Mongi Bouaicha, *Nanoscale Research Letters*, 7:455 (2012).
- [61] Yongkwan Kim, Angela Tsao, Dae Ho Lee† and Roya Maboudian, *J. Mater. Chem. C*, 1, 220–224 (2013).

- [62] M. Christophersen, J. Carstensen, S. Ronnebeck, C. Jager and W. Jager, *J. Electrochem. Soc.*, 148, E267 (2001).
- [63] V. Lehmann, *J. Electrochem. Soc.*, 140, 2836 (1993).
- [64] Guoliang Liu, Kaylie L. Young, Xing Liao, Michelle L. Personick, and Chad A. Mirkin, *J. Am. Chem. Soc.*, 135, 12196–12199 (2013).
- [65] A. Backes, U. Schmid, *Sensors and Actuators B*, 193, 883–887 (2014).
- [66] M.L. Zhang, K.Q. Peng, X. Fan, J.S. Jie, R.Q. Zhang, S.T. Lee, N.B. Wong, *J. Phys. Chem. C*, 112, 4444–4450 (2008).
- [67] H. Krishna, R. Sachan, J. Strader, C. Favazza, M. Khenner, R. Kalyanaraman, arXiv:1002.2100, *cond-mat.mtrl-sci.*(2010)
- [68] K. W. Kolasinski, *Nanos. Res. Lett.*, 9:432 (2014).
- [69] A. Backes, A. Bittner, M. Leitgeb, U. Schmid, *Scripta Materialia*, 114, 27–30 (2016).
- [70] Ruby A. Lai, Thomas M. Hymel, Vijay K. Narasimhan, and Yi Cui, *ACS Appl. Mater. Interfaces*, 8, 14, 8875–8879 (2016).
- [71] Nadine Geyer, Bodo Fuhrmann, Zhipeng Huang, Johannes de Boor, Hartmut S. Leipner, and Peter Werner, *J. Phys. Chem. C*, 116, 13446–13451 (2012).
- [72] Keorock Choia, Yunwon Songa, Ilwhan Ohb and Jungwoo Oh, *RSC Adv*, 00, 1-3 (2015).
- [73] Bing Jiang, Meicheng Li, Yu Liang, Yang Bai, Dandan Song, Yingfeng Lia and Jian Luo, *Nanoscale*, 8, 3085–3092 (2016).
- [74] Brendan D. Smith, Jatin J. Patil, Nicola Ferralis, and Jeffrey C. Grossman, *ACS Appl. Mater. Interfaces*, 8, 8043–8049 (2016).
- [75] Cheng, S., Chung, C. & Lee, H, *Journal of the Electrochemical Society*, **155**, D711–D714 (2008).
- [76] Huihui Chen, Rujia Zou, Haihua Chen, Na Wang, Yangang Sun, Qiwei Tian, Jianghong Wu, Zhigang Chen and Junqing Hu, *J. Mater. Chem.*, 21, 801–805 (2011).
- [77] C.-Y. Chen & C.-P. Wong, *Chem. Commun*, 49, 7295–7297 (2013).
- [78] A. I. Hochbaum, D. Gargas, Y. J. Hwang & P, Yang, *Nano letters*, **9**, 3550–3554 (2009).
- [79] Chia-Yun Chen, Ta-Cheng Wei, Cheng-Ting Lin & Jheng-Yi Li, *Sci. Rep.* 7:3164 (2017)
- [80] Max O. Williams, Daniel Hiller, Thomas Bergfeldt, and Margit Zacharias, *J. Phys. Chem. C*, 121, 9296–9299 (2017).
- [81] Bich Ha Nguyen, Van Hieu Nguyen and Hong Nhung Tran, *Adv. Nat. Sci.: Nanosci. Nanotechnol.*, 7, 03300 (2016).
- [82] M. Baia, F.Toderas, L. Baia, J. Popp and S. Astilean, *Chem. Phys. Lett.*, 422, 127–132 (2006).

- [83] D. He, B. Hu, Q. F.Yao, K. Wang, and S-H. Yu, *ACS Nano*, 3, 3993-4002 (2009).
- [84] L. Billot, M. L. de la Chapelle, A. S. Grimault, A. Vial, D. Barchiesi, J. L. Bizeon, P. M. Adam and P. Royer, *Chem. Phys. Lett.*, 422 303 (2006).
- [85] Chen-Chieh Yu, Sin-Yi Chou, Yi-Chuan Tseng, Shao-Chin Tseng, Yu-Ting Yen and Hsuen-Li Chen, *Nanoscale*, 7, 1667 (2015).
- [86] S. Chattopadhyay, H. C. Lo, C. H. Hsu, L. C. Chen, K. H. Chen, *Chem. Mater.*, 17, 553 (2005).
- [87] Baohua Zhang, Haishui Wang, Lehui Lu, Kelong Ai, Guo Zhang, and Xiaoli Cheng, *Adv. Funct. Mater.*, 18, 2348–2355 (2008).
- [88] Lara Mikac, Mile Ivanda, Marijan Gotić, Aleksandar Maksimović, Sebastiano Trusso, Cristiano D’Andrea, Antonino Foti, Alessia Irrera, Barbara Fazio, Pietro Giuseppe Gucciardi, *Croat. Chem. Acta*, 88, 437–444 (2015).
- [89] Bi-Shen Lee, Ding-Zheng Lin & Ta-JenYen, *Sci. Rep.*, 7:4604 (2017).
- [90] Xuexian Chen, Jinxiu Wen, Jianhua Zhou, Zebo Zheng, Di An, Hao Wang, Weiguang Xie, Runze Zhan, Ningsheng Xu, Jun Chen, Juncong She, Huanjun Chen, and Shaozhi Deng, *J. Opt.*, 20, 024012 (2018).
- [91] Asger W. Nørgaard, Jitka S. Hansen, Jorid B. Sørli, Marcus Levin, Peder Wolkoff, Gunnar D. Nielsen, and Søren T. Larsen, *Toxicological Sciences*, 137, 179–188 (2014).
- [92] K.P. Sooraj, Mukesh Ranjan, Rekha Rao, Subroto Mukherjee, *Appl. Sur. Sc.* 447, 576-581 (2018).
- [93] Layla A. Wali, Khulood K. Hasan, Alwan M. Alwan, *Spec. Acta Part A: Mol. and Biomol. Spectr.*, 206, 31-36 (2019)
- [94] A. K. Green and E. Bauer, *J. Appl. Phys.*, 47, 1284 (1976).
- [95] Nasim Mahmoodi, Abduljabbar I. Rushdi, James Bowen, Aydin Sabouri, Carl J. Anthony, Paula M. Mendes, and Jon A. Preece, *J. Vac. Sci. Technol. A*, 35, 041514 (2017).
- [96] R. T. Downs, K. L. Bartelmehs, G. V. Gibbs, & M. B. Boisen, *American Mineralogist*, 78(9-10), 1104-1107 (1993).
- [97] U. Holzwarth and N. Gibson, *Nat. Nanotechnol.*, 6, 534 (2011).
- [98] Peter Zaumseil, *J. Appl. Cryst.*, 48, 528–532 (2015).
- [99] J. E. Potts, R. Merlin, D. L. Partin, *Phys. Rev. B*, 27, 6, 3905-3908 (1983).
- [100] Z. Cao, Q. Huang, C. Zhao, Q. Zhang, *Electron. Mater. Lett.*, 12, 742 (2016).
- [101] J.M. Albella (ed.), *Láminas delgadas y recubrimientos: Preparación, propiedades y aplicaciones*, Instituto de Ciencia de Materiales, CSIC, Madrid, 2003.

- [102] Z. Xu, H.-Y. Wu, S. U. Ali, J. Jiang, B. T. Cunningham, and G. L. Liu, *J. Nanopho.*, 5, 053526 (2011).
- [103] J. Zheng, l. He, *Com. Rev. in Food Sc. and Food Saf.*, 13, 317-328 (2014).
- [104] C. Li, Y. Huang, K. Lai, B. A. Rasco, Y. Fan, *Food Cont.*, 65, 99-105 (2016).
- [105] C. Byram, S. S. B. Moram, A. K. Shaik, V. R. Soma, *Chem. Phys. Lett.*, 685, 103-107
- [106] E. C. L. Ru, E. Blackie, M. Meyer, P. G. Etchegoin, *J. Phys. Chem. C*, 111, 13794-13803 (2007).
- [107] C. Byram, V. R. Soma, *Nano-struc. & Nano-obj.*, 12, 121-129 (2017).
- [108] Yuko S. Yamamoto and Tamitake Itoh, *J. Raman Spectrosc.*, 47, 78–88 (2016).
- [109] Yuda Zhao, Xin Liu, Dang Yuan Lei and Yang Chai, *Nanoscale*, 6, 1311 (2014).
- [110] Jesse Theiss, Prathamesh Pavaskar, Pierre M. Echternach, Richard E. Muller, and Stephen B. Cronin, *Nano Lett.*, 10, 2749–2754 (2010).
- [111] P. Yimsiri, M. R. Macley, *Chem. Engg. Sc.*, 61, 3496-3505 (2006).